Modelling dispersion and mixing in geophysical flows

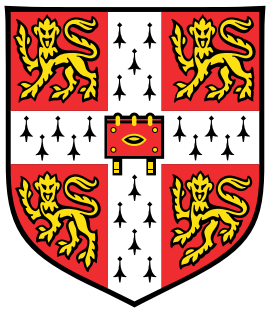

Neeraja Bhamidipati

Department of Earth Sciences

University of Cambridge

This dissertation is submitted for the degree of

Doctor of Philosophy

Murray Edwards College April 2020

Declaration

This thesis is the result of my own work and includes nothing which is the outcome of work done in collaboration except as declared in the Preface and specified in the text. It is not substantially the same as any that I have submitted, or, is being concurrently submitted for a degree or diploma or other qualification at the University of Cambridge or any other University or similar institution except as declared in the Preface and specified in the text. I further state that no substantial part of my thesis has already been submitted, or, is being concurrently submitted for any such degree, diploma or other qualification at the University of Cambridge or any other University or similar institution except as declared in the Preface and specified in the text. It does not exceed the prescribed word limit for the relevant Degree Committee.

Neeraja Bhamidipati
April 2020

Modelling dispersion and mixing in geophysical flows

Neeraja Bhamidipati

This thesis is concerned with modelling geophysical flows. The problems considered in this work include dispersion in flows through heterogeneous porous rocks, turbulent mixing in the surface layer of the ocean, and mixing in turbulent starting plumes. In chapters 2, 3 and 4, we study the longitudinal dispersion of a passive tracer by a two-dimensional pressure-driven flow through a layer of heterogeneous porous rock which is bounded above and below by impermeable seal rock. In chapters 2 and 3, we assume that the heterogeneity of the rock is due to localised regions of different permeability located at randomly assigned vertical positions within the otherwise uniform permeability layer. It is well known that in a porous layer of large cross-flow extent, such heterogeneity leads to Fickian-type dispersion. However, many porous rocks consist of relatively thin, laterally extensive layers. As a result, streamlines in the centre of the channel can be diverted upwards or downwards into regions of higher permeability, while streamlines near the boundaries are more restricted. We demonstrate that this results in a net cross-layer shear in the mean flow. We develop a depth-averaged model for the dispersal of a pulse of tracer by the flow, which shows that although at early times the Fickian dispersion dominates, at large distances downstream the spreading of the pulse of tracer is controlled by the shear. In chapter 4, we demonstrate this shear in a cross-bedded formation, focusing on the flow across an interface between two neighbouring zones of the rock. We explore the strength of this shear as a function of the permeability ratio across the interface and the interface angle. Finally, in chapters 5 and 6, we focus our attention on mixing in turbulent flows, considering two classes of problems – turbulent mixing of a passive tracer in the ocean mixed layer and mixing in turbulent starting plumes. In chapter 5, we present results from high resolution numerical simulations of the ocean mixed layer to estimate an exact functional relationship between the turbulent fluxes and the gradients of a passive tracer. This functional form of the eddy diffusivity does not use any closure assumptions, and it highlights both local and non-local effects of mixing of a passive tracer. For simplicity, we restrict our focus to convection-driven mixing in an idealised two-dimensional surface layer of the ocean. In chapter 6, we explore the dynamics of turbulent starting plumes by analysis of a series of new small-scale laboratory experiments to describe the mixing and interaction between the plume head, the following steady plume, and the ambient. We find that the head of the plume ascends with a speed which is approximately 0.6 times the characteristic speed of the fluid in the following steady plume, and so the fluid released from the source eventually catches the head of the flow. On reaching the top of the plume, it recirculates and mixes in the plume head. We present results from new experiments to visualise the dispersion of the source fluid in the plume head, and propose a theoretical model to describe the dynamics of the plume head. We present our conclusions and discuss directions for future work in chapter 7.

I dedicate this thesis to my parents.

Acknowledgements

I would like to begin by thanking my supervisor, Professor Andrew W Woods, who made my PhD journey possible. His passion for science has inspired me immensely, and his attention to detail has helped improve my research practice significantly. I cannot thank him enough for his support and guidance, and for the many hours he spent discussing ideas with me.

I would also like to thank Professor Colm-cille Caulfield, whose advice I have sought time and again, for his counsel and for always saying yes to a chat despite his incredibly busy schedule. During my PhD, I spent three months in Woods Hole, Massachusetts, where I collaborated with Professor Glenn Flierl and Dr Andre Souza from MIT. Glenn and Andre have guided me to the world of oceanography and climate modelling, which is where my career will be headed after my PhD. For this, I owe them a debt of gratitude.

This thesis would not have been possible without the help of numerous people, including Keaton Burns, Greg Wagner and Basile Gallet, who were always up for helping me as I figured out the world of numerical simulations. Special thanks also to Lotty Gladstone and Andrew Pluck for helping me setup laboratory experiments during my first and second years in Cambridge.

I would also like to thank Chris Howland, Tyler Lutz, Sara Lenzi, Edward Hinton, Laura Cope, Thomas Le Reun, Rohit Supekar, Andrea Lehn, Sutirtha Sengupta, Bowen Zhao, David Goluskin, Alexis Kaminski, Megan Davies-Wykes, and Kat Smith for their company and our adventures during my time in Woods Hole. Working on problems in oceanography was certainly inspired by the time spent climbing, cycling and swimming with them.

My journey in Cambridge began in Beaufort House, where I had the chance to live with wonderful women from around the world, who continue to be a source of positivity in my life. For this, I would like to thank Ji Ying, Hande Güzel, Amanda Smyth, Päivi Pirhonen, Melony Dilshad and Laura Malric-Smith. My first year in Cambridge would not have been nearly as fun without

the company of Chelsea Kaandorp, Michelle Kwok, Ben Jackson, Lois Baker, Matthieu Kohl, Olly Whitehead, Jeremy Parker, Matt Butler and Loren Held, who helped me keep my head above water as I grappled with new mathematical concepts during Part III of the Mathematical Tripos.

Outside of research, time spent doing sports with Jeff Barda and Kari Jackson helped me stay active and motivated. I would also like to thank Bogdan Ganchev, who continues to be one of my closest friends, for his company and our conversations during the last five years in Cambridge. My list of thanks would not be complete without acknowledging Martin Lippert, who in many ways was my second pair of eyes and my confidant as I wrote journal articles and job applications.

I am most grateful to my parents, Rukmini Bhamidipati and Srinivas Bhamidipati, for encouraging me relentlessly and for making big sacrifices in order to see me and my sister succeed. My sister, Tanuja Bhamidipati, is my partner in crime and she continues to inspire me in more ways than she realises.

Finally, I would like to thank Jostein Løhr Hauge for being my best friend and the most supportive, considerate, and understanding partner I could have hoped for. He inspires me with his own writings and research, and I'm very grateful to have shared this journey with him.

Abstract

This thesis is concerned with modelling geophysical flows. The problems considered in this work include dispersion in flows through heterogeneous porous rocks, turbulent mixing in the surface layer of the ocean, and mixing in turbulent starting plumes. In chapters 2, 3 and 4, we study the longitudinal dispersion of a passive tracer by a two-dimensional pressure-driven flow through a layer of heterogeneous porous rock which is bounded above and below by impermeable seal rock. In chapters 2 and 3, we assume that the heterogeneity of the rock is due to localised regions of different permeability located at randomly assigned vertical positions within the otherwise uniform permeability layer. It is well known that in a porous layer of large cross-flow extent, such heterogeneity leads to Fickian-type dispersion. However, many porous rocks consist of relatively thin, laterally extensive layers. As a result, streamlines in the centre of the channel can be diverted upwards or downwards into regions of higher permeability, while streamlines near the boundaries are more restricted. We demonstrate that this results in a net cross-layer shear in the mean flow. We develop a depth-averaged model for the dispersal of a pulse of tracer by the flow, which shows that although at early times the Fickian dispersion dominates, at large distances downstream the spreading of the pulse of tracer is controlled by the shear. In chapter 4, we demonstrate this shear in a cross-bedded formation, focusing on the flow across an interface between two neighbouring zones of the rock. We explore the strength of this shear as a function of the permeability ratio across the interface and the interface angle. Finally, in chapters 5 and 6, we focus our attention on mixing in turbulent flows, considering two classes of problems – turbulent mixing of a passive tracer in the ocean mixed layer and mixing in turbulent starting plumes. In chapter 5, we present results from high resolution numerical simulations of the ocean mixed layer to estimate an exact functional relationship between the turbulent fluxes and the gradients of a passive tracer. This functional form of the eddy diffusivity does not use any

closure assumptions, and it highlights both local and non-local effects of mixing of a passive tracer. For simplicity, we restrict our focus to convection-driven mixing in an idealised two-dimensional surface layer of the ocean. In chapter 6, we explore the dynamics of turbulent starting plumes by analysis of a series of new small-scale laboratory experiments to describe the mixing and interaction between the plume head, the following steady plume, and the ambient. We find that the head of the plume ascends with a speed which is approximately 0.6 times the characteristic speed of the fluid in the following steady plume, and so the fluid released from the source eventually catches the head of the flow. On reaching the top of the plume, it recirculates and mixes in the plume head. We present results from new experiments to visualise the dispersion of the source fluid in the plume head, and propose a theoretical model to describe the dynamics of the plume head. We present our conclusions and discuss directions for future work in chapter 7.

Table of contents

Chapter 1

Introduction

This thesis focuses on a series of problems related to dispersion and mixing in geophysical flows. The thesis consists of three main parts: the first part relates to flow in porous media, the second part concerns turbulent mixing in the ocean, and part three is on turbulent starting plumes.

In the first part (chapters 2, 3 and 4), we study the dispersion of tracer in flows through heterogeneous porous rocks. Understanding the dispersion in such flows is crucial for many fundamental problems such as pollutant dispersal in groundwater, and more recently, carbon sequestration. In this thesis, we develop some simplified models of flows through a layer of heterogeneous porous rock, assuming that the heterogeneity of the rock is due to the presence of (i) localised zones of different permeability (chapters 2 and 3) and (ii) cross-bedding (chapter 4). We complement these models with numerical simulations to gain an understanding of the leading order controls on the dispersion of tracer in such flows.

In the second part (chapter 5), we study the turbulent mixing of a tracer in the ocean mixed layer. In the case where the mixing within these layers is driven by convection, there may be significant non-local transport by convective plumes, deep into the mixed layer. Often, this non-local mixing is modelled using an effective turbulent diffusivity, which has worked successfully through the use of many parametersations. In this thesis, using numerical simulations (DNS) of the ocean mixed layer, we show that the mixing of a passive tracer can be described by a non-local eddy diffusivity kernel which relates the turbulent fluxes with the gradients of tracer concentration throughout the layer.

In the third part (chapter 6), we study the dynamics of turbulent starting plumes in an unstratified and a stratified environment, identifying how (i) the drag on the plume head impacts the motion of the plume head, and (ii) the fluid in the tail of the plume mixes into the plume head. We present series of new small-scale laboratory experiments, and complement the experimental data with a theoretical model to describe the transient dynamics of these plumes.

The following sections give a brief overview of these three problems.

1.1 Dispersion in flows through heterogeneous porous rocks

Modelling flow through porous rocks has received considerable interest for several decades (Bear, 1971; Bickle, 2009; Dagan, 1984; Saffman, 1959; Tompson and Gelhar, 1990; Woods, 2015). Quantifying the dispersion associated with such flows has relevance for understanding groundwater flows in aquifers, radioactive waste disposal, and carbon sequestration in underground geological formations. In groundwater flows, there is interest in understanding the large-scale transport of contaminants released into the flow (Bear and Cheng, 2010; Suciu, 2014). In the case of carbon sequestration, it is important to understand the path followed by carbon dioxide as it spreads through a porous layer saturated with brine (Ghesmat et al., 2011; Hesse and Woods, 2010; Hidalgo and Carrera, 2009). If the fluid is incompressible, Newtonian, isothermal, and in steady-state, the two-dimensional velocity of the fluid may be described using Darcy's law (Darcy, 1856),

$$\mathbf{u} \equiv \begin{pmatrix} u \\ w \end{pmatrix} = -\frac{1}{\mu} \begin{pmatrix} k_{xx} & k_{xz} \\ k_{zx} & k_{zz} \end{pmatrix} \begin{pmatrix} \partial p/\partial x \\ \partial p/\partial z \end{pmatrix}, \tag{1.1}$$

where the 2×2 matrix on the right hand size is the permeability tensor, $\underline{\underline{k}}$, and p is the pressure. The permeability, $\underline{\underline{k}}$, may either be isotropic (a symmetric matrix with zero off-diagonal terms) or anisotropic (a symmetric and positive definite matrix).

One of the main challenges in modelling these flows is associated with random fluctuations in permeability—or heterogeneity—in the structure of the porous layer, which can lead to large scale dispersion in the flow (Greenkorn and Kessler, 1969; Matheron and De Marsily, 1980; Srzic et al., 2013). One

method to estimate the dispersion is to add passive tracers to the flow at an injection well and then sample the fluid at an observation well downstream (Kampman et al. (2014); Mathieson et al. (2011), see figure 1.1). In some cases, stochastic models have been used to describe this dispersion in heterogeneous rocks (Dagan, 1982; Gelhar et al., 1979; Meyer et al., 2010). These models often assume that the heterogeneities become decorrelated over some length scale leading to a mean transport process that is Fickian.

Cala and Greenkorn (1986) investigated the dispersion of flow in a confined porous medium of finite vertical extent consisting of a single localised lens of different permeability. They found that, compared to a homogeneous medium, the difference in permeability between the lens and the background causes a localised shearing of the flow. Eames and Bush (1999) generalised this approach by considering flow through a random assemblage of such lenses in a periodic domain with a view to derive a continuum model for the dispersion. They assumed that the lenses are sufficiently far apart so that the distortion of the flow associated with each lens is independent. In this dilute limit, they showed that the dispersive process is Fickian at large times. Dagan and Fiori (2003) and Fiori et al. (2003) have since further generalised this approach and derived valuable expressions for the effective dispersion coefficient in a heterogeneous medium. Janković et al. (2003) tested their solutions with a series of numerical simulations of the dispersal of a patch of tracer of much smaller vertical extent than the size of the numerical domain and located far from the vertical boundaries. Implicit in these models is the assumption that the streamlines all sample the same mean speed, irrespective of vertical position in the layer, and as a result, the heterogeneity leads to a Fickian type dispersion. This simplification is appropriate in a vertically extensive layer in which the cross-layer scale of the heterogeneity is much smaller than the vertical extent of the layers. However, many porous rocks are relatively thin but laterally extensive over hundreds of meters, and are often bound by impermeable seal rock at the top and bottom (see figure 1.1).

In this thesis, we explore the role of: (i) the vertical boundaries of the formation, and (ii) heterogeneity of the rock on the dispersal of tracer as the flow migrates through a heterogeneous porous layer of finite vertical extent.

In chapters 2 and 3, we assume that the heterogeneity of the rock is due to the presence of localised zones of different permeability in an otherwise uniform permeability layer (cf. Cala and Greenkorn (1986), Dagan et al. (2003)). In

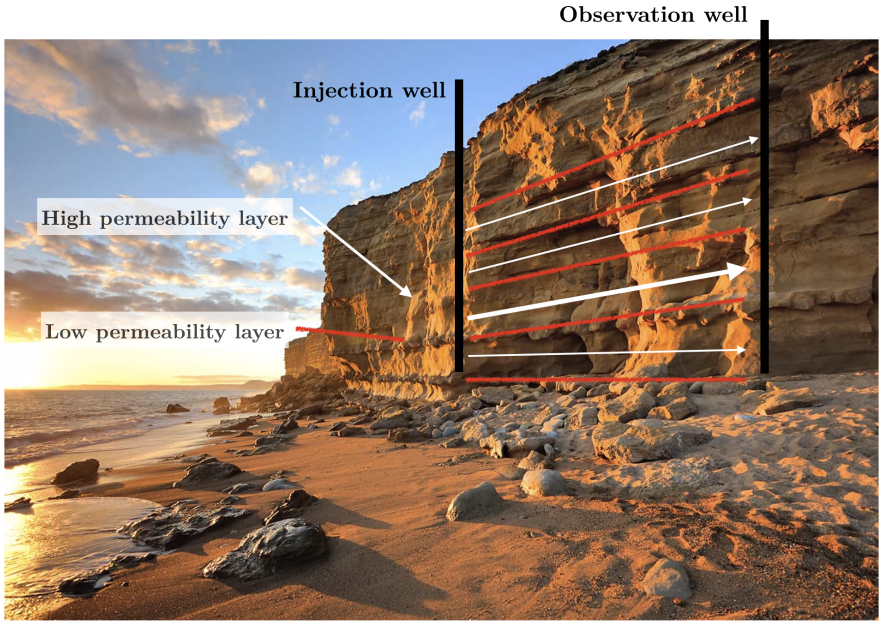

Figure 1.1 Illustration of injection and observation wells in a layered and laterally extensive heterogeneous formation. This photograph of Bridport sandstone in Dorset, England illustrates alternating high permeability and low permeability layers of different cross-layer extents. The high permeability layers are of the order 10 metres, and the low permeability layers are of the order 1 metre. The formation shown here has a height of 120 metres and is laterally extensive over tens of kilometres.

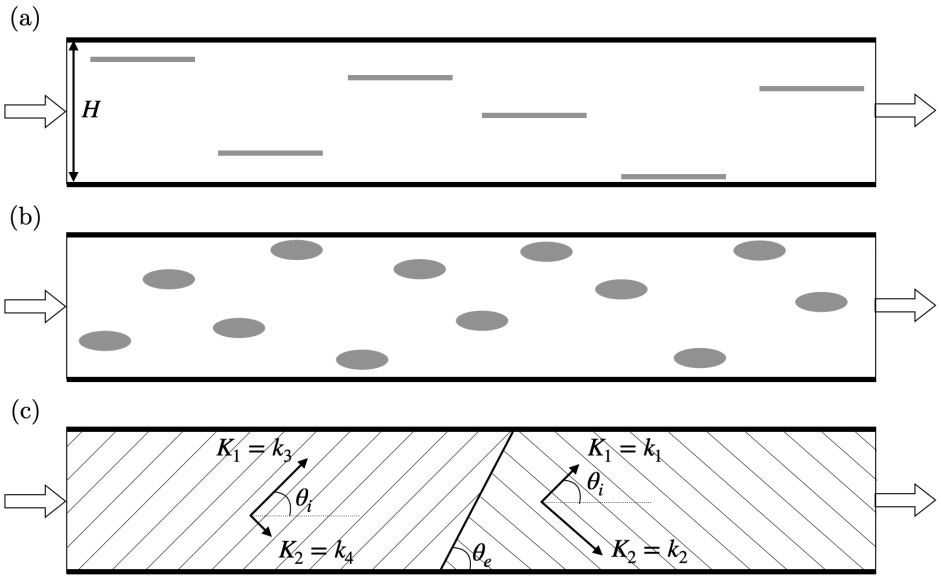

Figure 1.2 (a)-(c) Schematics of the model setup of problems presented in chapters 2, 3, and 4 respectively. In (a) and (b), the lenses have permeability k_2 and are embedded in a domain with background permeability k_1. The lenses have length l and height h, in a channel of width H. In (a), $l \gg h, H$, and in (b), $l/H \sim \mathcal{O}(1)$. In (c), within the cross-bedded layer to the right of the interface, the permeability is k_2 and k_1, along and across the bedding, and the bedding planes are inclined at an angle θ_i to the lateral boundaries. The interface between the two individual zones of rock is tilted at an angle θ_e to the lateral impermeable boundaries.

flows through such a porous layer, it is well known that a pulse of tracer released into the flow spreads with time as $\sqrt{t}$ owing to the Fickian dispersion (Dagan and Fiori, 2003; Eames and Bush, 1999). Here, we demonstrate that, in addition, the probability that a streamline is diverted into a high permeability lens increases with distance from the boundaries, leading to a net cross-layer shear in the mean flow. At late times, the distortion of a parcel of tracer by this cross-layer shear eventually dominates the effect of Fickian dispersion, and the tracer spreads linearly with time in the along-flow direction. This is consistent with many field observations, which suggest that the along-flow length scale of the tracer increases approximately linearly with distance downstream (Gelhar et al., 1992).

In chapter 2, we quantify the magnitude of this mean shear based on the assumption that lenses are long and thin (figure 1.2(a)). We develop asymptotic solutions for the evolution of the depth-averaged concentration of a finite pulse of tracer released into the flow, showing how the spreading of the tracer is initially controlled by Fickian dispersion, but at longer times becomes dominated by the shear. In chapter 3, we extend our analysis to consider elliptical lenses of length comparable to the channel width (figure 1.2(b)). We discuss the implications of our results to tracer dispersal in a layered formation consisting of many layers of different vertical extent (figure 1.1). Although our present model is simplified, we repeat similar calculations in layers where the permeability varies smoothly about a mean value, and find analogous flow patterns.

In chapter 4, we consider a different type of rock in which the permeability is composed of cross-bedded layers—such as in fluvial systems or some aeolian deposits—in which coarse and fine particles are successively deposited, building up a high permeability along the bedding and much smaller permeability across the bedding planes. In many of these formations, the rock is essentially a composite of different zones of cross-bedding with different permeability ratio and different angles of bedding (Allen, 1963; Davis et al., 1993; Goggin et al., 1988). As a result, the junctions between successive bedding planes leads to a transition in the flow pattern (figure 1.2(c)). Consequently, the flow once again develops a mean shear. We present a series of numerical results to investigate the magnitude of this shear in a cross-bedded formation, showing how (i) the permeability ratio across the interface, and (ii) the interface angle may combine constructively to produce a larger shear, or may negate one another, reducing

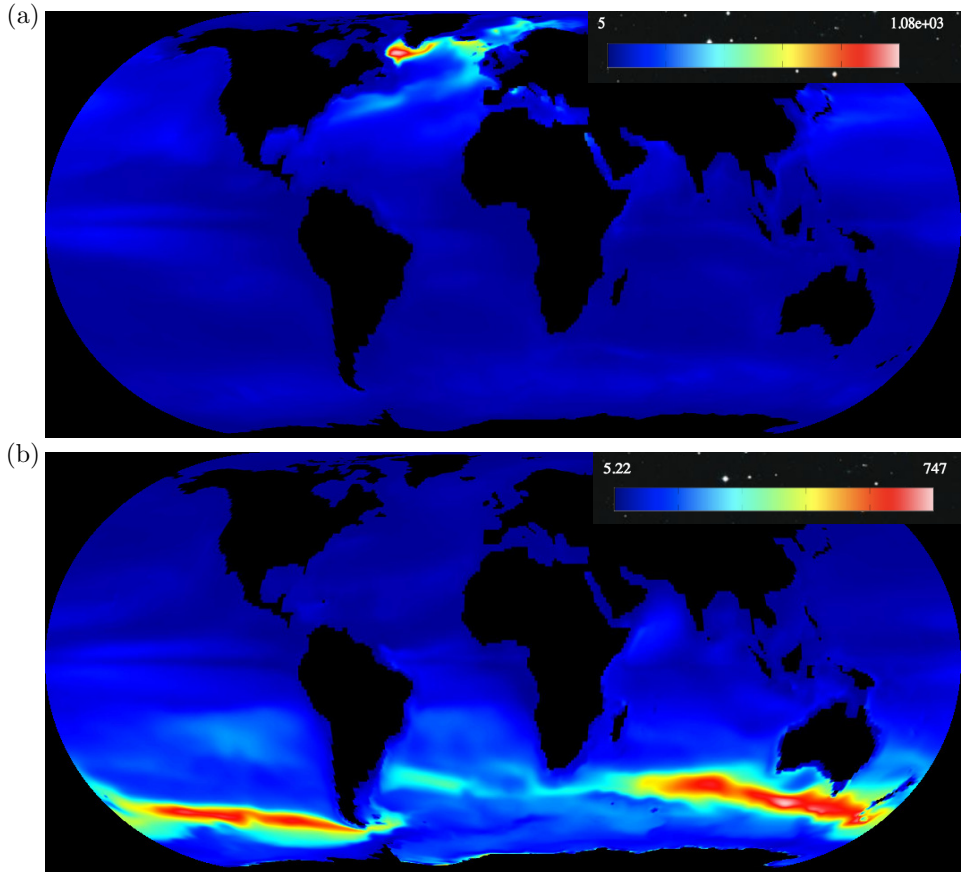

Figure 1.3 Surface mixed layer depth (in metres) in (a) January (boreal winter), and (b) August (boreal summer). Source: http://eddies.mit.edu/esglobe/.

or reversing the sign of the shear. We discuss some of the implications of this shear for modelling flow in such composite rocks.

1.2 Turbulent mixing in the ocean mixed layer

The ocean mixed layer is the region in the ocean directly underneath the air-sea interface. It is characterised by nearly uniform temperature and salinity throughout the layer. The depth of these layers is typically $\mathcal{O}(10-1000)$ m and exhibits large seasonal variations depending on the latitude. The mixing within these layers is driven by a range of factors. In the boreal winter, convection acts to deepen the mixed layer in the regions close to the North pole, predominantly around the Labrador and Greenland seas (figure 1.3(a)), whereas in the boreal summer, convection is strongest close to the South pole, producing deeper mixed layers close to the Antarctic (figure 1.3(b)).

The ocean mixed layer mediates the exchange of mass, momentum and energy between the ocean and the atmosphere (Kantha and Clayson, 2000). From a biological perspective, the ocean mixed layer is nutrient-poor, and its depth determines the average level of light seen by phytoplankton. Therefore, the mixing at the base of the ocean mixed layer is crucial for biological productivity (Kuhlbrodt et al., 2009).

In modelling the mixing in such flows, suppose that the fluid carries with it a tracer, ϕ, which is either active (e.g. temperature and salinity) or passive, that satisfies an advection–diffusion equation (Vallis, 2019),

$$\frac{\partial \phi}{\partial t} + \mathbf{u} \cdot \nabla \phi = \kappa \nabla^2 \phi, \tag{1.2}$$

where κ is the molecular diffusivity. For simplicity, if we assume that the flow is two-dimensional, and that the flow and the tracer have a mean and a fluctuating component ($\phi = \overline{\phi} + \phi'$), the mean equation is given by

$$\frac{\partial \overline{\phi}}{\partial t} + \frac{\partial}{\partial x}(\overline{u}\overline{\phi}) + \frac{\partial}{\partial z}(\overline{w}\overline{\phi}) = -\frac{\partial}{\partial x}(\overline{u'\phi'}) - \frac{\partial}{\partial z}(\overline{w'\phi'}) + \kappa \nabla^2 \overline{\phi}. \tag{1.3}$$

where $\overline{*} = \tau^{-1} \int_0^\tau * \, \mathrm{d}t$; τ is an appropriate averaging timescale. The goal then is to understand the evolution of a certain mean property, $\overline{\phi}$, without a detailed description of the turbulent fluctuating components of the flow and the tracer. This generally requires a parameterisation of the turbulent fluxes, $\overline{u'\phi'}$ and $\overline{w'\phi'}$, in the mean equation (1.3). Several parameterisations have been proposed to express the turbulent fluxes in terms of the mean gradients so that

$$\overline{u'\phi'} = -K \frac{\partial \overline{\phi}}{\partial x} \quad \text{and} \quad \overline{w'\phi'} = -K \frac{\partial \overline{\phi}}{\partial z}, \tag{1.4}$$

where K is a turbulent diffusivity. This reduces equation (1.3) to

$$\frac{\partial \overline{\phi}}{\partial t} + \frac{\partial}{\partial x}(\overline{u}\overline{\phi}) + \frac{\partial}{\partial z}(\overline{w}\overline{\phi}) = K \nabla^2 \overline{\phi} + \kappa \nabla^2 \overline{\phi}. \tag{1.5}$$

This idea of using a turbulent diffusivity, K, to represent the turbulent fluxes, although rather ad-hoc, has worked successfully through the use of many parameterisations (Kraus and Turner, 1967; Large et al., 1994; McWilliams and Sullivan, 2000; Mellor and Yamada, 1982; Reichl and Li, 2019). If model parameterizations are to describe the upper ocean mixing processes accurately, they must be strongly physically based. In chapter 5, we propose a new method to estimate an exact and unapproximated formulation for the flux in terms of

the property gradient. As an example, we consider an idealised problem of the turbulent mixing of a passive scalar in the ocean surface layer. Using numerical simulations, we parameterise the horizontally and temporally averaged fluxes as a functional of the horizontally and temporally averaged property gradients so that

$$\langle w'\phi' \rangle = -\int \mathrm{d}z' \mathcal{K}(z|z') \frac{\partial \langle \phi \rangle}{\partial z'}. \tag{1.6}$$

where $\langle * \rangle = \lim_{\tau \to \infty} \tau^{-1} \int_0^\tau * \, \mathrm{d}t$, and $\mathcal{K}(z|z')$ is the eddy diffusivity kernel which describes the vertical transport by eddies at any vertical location, z. In chapter 5, we estimate this kernel and demonstrate that the kernel contains information pertaining to the non-locality of the flow that is missing from a local diffusivity. This non-local behaviour might be especially important for transient processes that occur on short timescales, where the non-local fluxes could lead to qualitative macroscopic differences in properties in the ocean mixed layer.

Although several parameterisations have been defined in literature, the analysis presented in this chapter does not use any closure assumptions, and the functional form of the eddy diffusivity kernel is based on an unapproximated representation of the chosen physics. This type of formulation can be further extended to other problems in turbulence concerning the mixing of a passive scalar.

1.3 Dispersion and mixing in turbulent starting plumes

The study of turbulent plumes in uniform and stratified ambients has been of interest for many decades owing to their importance in numerous industrial and environmental processes (Hewitt, 2020; Morton et al., 1956; Woods, 2010). Morton et al. (1956) showed that the rate of entrainment of ambient fluid at a given height is proportional to the characteristic plume velocity at that height, and developed a series of self-similar solutions based on this assumption. These solutions have proven robust to many experimental observations and theoretical analyses. Turner (1962) explored the transient nature of buoyant plumes with an experimental investigation of the initial stages of formation of a turbulent buoyant plume, measuring the properties of the plume head which develops

Figure 1.4 Photograph of a plume (Mount Merapi, Indonesia). Source: Eastern Herald.

ahead of the steady plume. The key observation of his work was that the plume head rises at a speed that is approximately 0.6 times the characteristic velocity of the steady plume which develops behind the head.

Turner (1962), Middleton (1975), and more recently, Scase et al. (2009) have proposed theoretical models for the dynamics of the head of the plume building on the vortex-ring theory for a discrete buoyant thermal proposed by Turner (1957), although some uncertainty remains about the internal dynamics of the plume head (Scase et al., 2009). There is also little experimental evidence supporting the theory that with highly turbulent flow, the plume head behaves as a vortex ring. In chapter 6, we reassess the dynamics of a starting plume with a series of new experiments, exploring the balance of mass, momentum and buoyancy between the plume and the plume head. Our results imply that the buoyancy force exerted on the plume head plus the momentum flux supplied by the following plume exceeds the rate of change of momentum of the plume head, even including the added-mass of the plume head. We propose that the difference is associated with a drag force resulting from the displacement of ambient fluid around the plume head.

We test our model using experimental analysis of starting plumes in a stratified ambient, akin to starting plumes encountered in nature (figure 1.4). In a stratified ambient, the plume head is no longer self-similar, but assuming

that the plume head retains the same shape as in the unstratified case allows an initial estimate for the height of rise with time, which compares well with experimental data up to the point that the plume head reaches the maximum height of rise of the ensuing steady plume.

As well as the starting plume, these experiments may provide some new insights into the class of problems in which the source buoyancy flux of an established plume is rapidly increased from one value to another. In this case, it is likely that a plume head type structure, akin to the starting plume, may develop between the original and new plume (Scase et al., 2009, 2006).

Chapter 2

Dispersion in porous rocks with long and thin lenses

The material contained in this chapter and the next chapter has been submitted for publication in *Journal of Fluid Mechanics*, under the title 'Boundary-induced shear and tracer transport in heterogeneous porous rock' (Bhamidipati and Woods, 2020a).

2.1 Introduction

Quantification of flow in porous rocks is central to modelling oil and gas recovery, pollutant dispersal in groundwater, geothermal power production, and more recently, carbon sequestration (Bear, 1971; Bickle, 2009; Dagan, 1984; Saffman, 1959; Tompson and Gelhar, 1990; Woods, 2015). In modelling such flows, one of the challenges is associated with heterogeneities in the structure of the porous layer, which can lead to large scale dispersion in the flow (Cala and Greenkorn, 1986; Greenkorn and Kessler, 1969; Matheron and De Marsily, 1980; Srzic et al., 2013). In some studies, stochastic models have been used to describe the dispersion (Dagan, 1982; Gelhar et al., 1979; Meyer et al., 2010). These models often assume that the heterogeneities become decorrelated over some length scale leading to a mean transport process that is eventually Fickian. However, the complex structure of porous medium can lead to long-range velocity correlations which produce anomalous transport at early times (Berkowitz et al., 2000; Koch and Brady, 1988; Zavala-Sanchez et al., 2009).

Eames and Bush (1999), Dagan et al. (2003) and Janković et al. (2003) have derived valuable expressions for the effective dispersion coefficient in a heterogeneous medium assuming that the porous medium is composed of a random assemblage of lenses of different permeability. These models assume that the cross-flow scale of the domain is much larger than the size of each lens, and as a result, the streamlines all sample the same mean speed, irrespective of vertical position in the layer. Consequently, the heterogeneity eventually leads to a Fickian-type dispersion. This simplification is appropriate in a vertically extensive layer in which the cross-layer scale of the heterogeneity is much smaller than the vertical extent of the layer.

In this chapter we explore the role of the upper and lower boundaries on the structure of the flow in a heterogeneous permeable layer. We find that the mean speed associated with streamlines whose distance from the boundary is comparable to or smaller than the cross-layer scale of the heterogeneity is smaller than that of the streamlines in the centre of the channel. As an illustration of this effect, we present a numerical calculation of flow in a permeable channel, in which the permeability is log-normally distributed about a mean value. Figure 2.1(a) shows the streamlines of the flow and figure 2.1(b) shows the path followed by an initially vertical streak of dye released into the layer. The numerical scheme used to run this simulation is described in appendix A. The colours in figure 2.1(a) represent the permeability field generated using a fast Fourier transform method proposed by Dietrich and Newsam (1993), where red represents high permeability and blue represents low permeability. It may be seen that streamlines are diverted up and down within the layer in order to localise in the higher permeability zones. Figure 2.1(b) illustrates that the vertical pulse of tracer becomes sheared as it travels down the channel, with the flow speed greatest near the centre of the channel. Although the figure only presents one specific realisation, we have repeated such calculations for several comparable but random realisations and find analogous flow patterns.

In order to identify the processes which lead to the development of a shear in the mean flow profile in a heterogeneous porous layer, we examine some idealised models of heterogeneous porous layers. In §2.2, we examine the along-layer averaged flow which develops when there are a series of long and thin lenses along the channel, each at a different random cross-channel position. We primarily focus on lenses of high permeability but also consider lenses of low permeability for completeness. By examining the probability that a particular

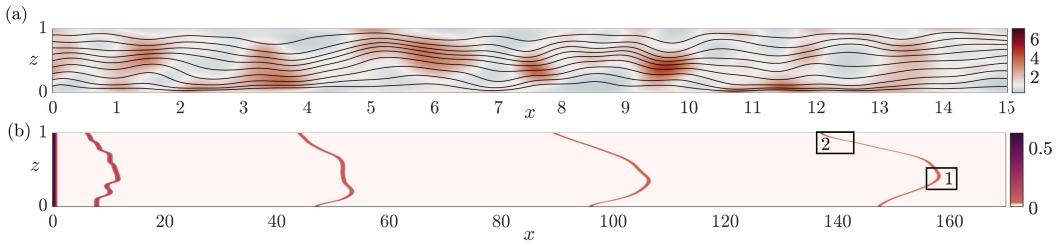

Figure 2.1 (a) The streamlines for the flow through a heterogeneous porous layer. The colours represent the permeability field generated using a fast Fourier transform method proposed by Dietrich and Newsam (1993). The permeability is log-normally distributed with mean permeability $\bar{k} = 0$ and standard deviation $\sigma_k = 0.5$. The horizontal correlation scale for the permeability field is $l_x = 1$ and the vertical correlation scale is $l_z = 0.4$, in a channel of width $H = 1$. Note that the figure in panel (a) is drawn to scale but only shows a section of the channel from $x = 0$ to $x = 15$. (b) (Not drawn to scale) The evolution of the concentration field, $c(x, z, t)$, for a Gaussian pulse of tracer released into the channel. The four profiles show the concentration at five different times. $t = 1, 10, 50, 100, 150$, after its initial release at $x = 0.25$, $t = 0$.

streamline passes through a lens located at a particular height in the channel, we derive an expression for (i) the along-layer averaged mean flow, $U(z)$, and (ii) the longitudinal dispersion coefficient, $D(z)$, as a function of the height in the channel. The dispersion arises when the flow migrates along a channel containing a series of lenses which are located at random positions across the channel. In §2.3, we use this continuum model to study the evolution of the depth-averaged concentration of tracer released into the layer as a function of distance along the layer, x. We show that the tracer undergoes a transition from Fickian dominated spreading at early times to shear dominated spreading at late times. Since some geological formations include both high and low permeability lenses, in §2.4 we generalise this analysis to account for variations in the permeability of the lenses. In §2.5, we consider the implications of these new results to the dispersion of the flow in a heterogeneous geological formation consisting of many layers, as compared to dispersal in a single deep layer of equivalent depth.

2.2 Development of shear flow in a bounded domain

To understand how the along-channel velocity field develops a shear in a heterogeneous porous layer, we consider an idealised pressure-driven flow through a layer of permeable rock of permeability k_1 which contains a series of lenses of permeability k_2 located along the channel at different random positions across the channel. We assume that the lenses are long and thin, with length l in the along-flow direction and height h in the cross-flow direction, while the channel has width H such that $l \gg H, h$. The lenses are placed so that the horizontal distance between successive lenses is much greater than the width of the channel, $(L - l) \gg H$. Figure 2.2(a) shows the numerical solution for the streamlines of the flow, through a layer containing lenses whose permeability is 10 times the background permeability, as calculated using the numerical method described in appendix A. Figure 2.2(b) illustrates the evolution in time of a pulse of dye, initially arranged as a vertical line across the layer; the dye which moves along the high permeability lenses stretches out ahead of the rest of the pulse of dye.

In order to calculate the mean flow speed along each streamline, we first estimate the probability that the streamline passes through a lens as a function of the position of the lens in the channel (§2.2.1). By considering the flow through an assemblage of such lenses, we estimate the expected travel time along different streamlines (§2.2.2). This demonstrates the development of a shear in the along-channel averaged flow (§2.2.3). We use this ensemble model as the basis for a continuum model for the evolution of tracer in terms of the mean speed, $U(z)$, and longitudinal dispersion, $D(z)$ (§2.2.4). We conclude the section by studying the dependence of this continuum model on the properties of the lenses (§2.2.5) and on the separation distance between lenses (§2.2.6).

2.2.1 Probability of individual streamlines passing through a lens

As may be seen in figure 2.2, except near the ends of the lenses, the flow is approximately parallel to the lateral boundaries, and so we expect the along-channel pressure gradient to be uniform across the channel. Therefore, for the

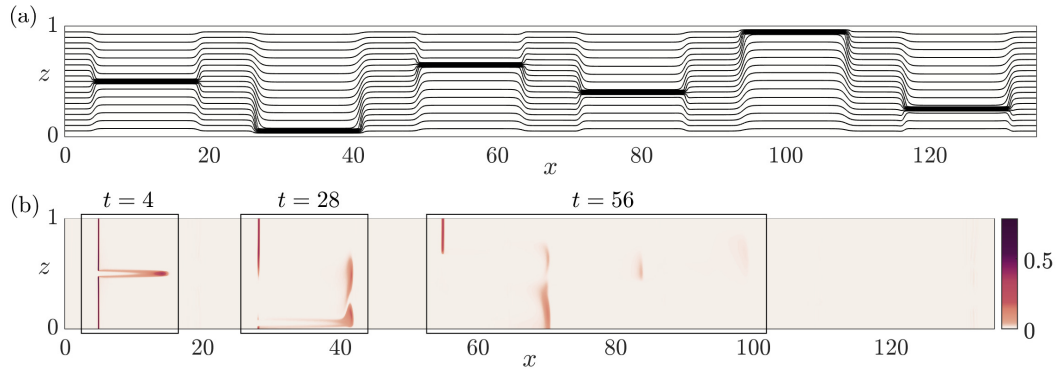

Figure 2.2 (a) The streamlines for the flow through an assemblage of randomly placed lenses in a channel. The lenses have length $l = 15$ in the along-flow direction and height $h = 0.05$ in the cross-flow direction, in a channel of width $H = 1$. The centres, $(x_c(i), z_c(i))$, of successive lenses, $i = 1, ..., n$, are given by $x_c(i) = (2i - 1)L/2$, where $L = 22.5$ is the horizontal distance between the centres of successive lenses $(L > l)$, and the vertical location of each lens is randomly chosen from a continuous uniform distribution, $0 \leq z_c(i) \leq H$. Here, the permeability of the lens relative to the background permeability is $k_2/k_1 = 10$. (b) The evolution of the concentration field, $c(x, z, t)$, for a Gaussian pulse of tracer released into the channel. The three boxes show the tracer at three different times, $t = 4, 28, 56$, after its initial release at $x = 0.25$, $t = 0$.

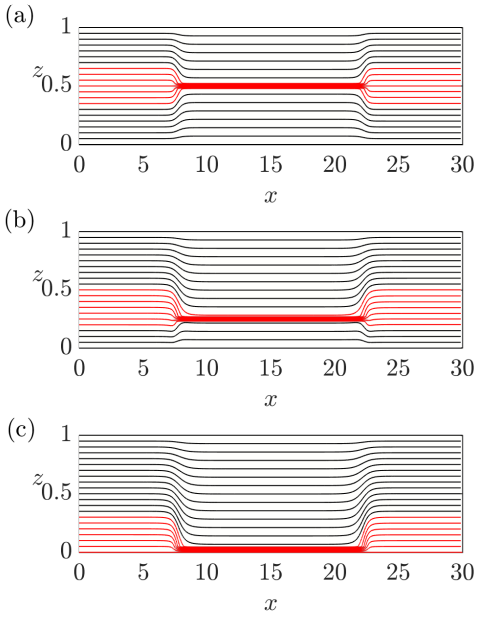

Figure 2.3 Panels (a)-(c) show the streamlines for the flow past a long and thin rectangular lens with permeability greater than background permeability ($k_2/k_1 = 10,\ l = 15,\ h = 0.05,\ H = 1$), located with its centre at $z_c = 0.5, 0.25, 0.025$ respectively. In each case, the lens diverts approximately 7 of 21 streamlines across the channel, as indicated in red.

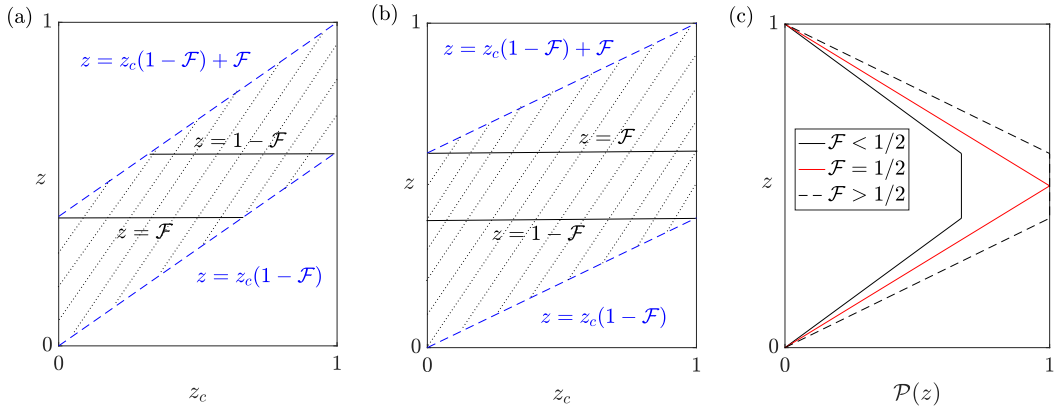

Figure 2.4 A lens whose centre is located at dimensionless height z_c diverts streamlines from the region $z_{min} \le z \le z_{max}$, where $z_{min} = z_c(1-\mathcal{F})$ and $z_{max} = z_c(1-\mathcal{F}) + \mathcal{F}$. Note that $z_{max} - z_{min} = \mathcal{F}$. Panels (a) and (b) show this zone of influence for an assemblage of lenses for the cases $\mathcal{F} = 0.4 (< 0.5)$ and $\mathcal{F} = 0.6 (> 0.5)$ respectively. For an assemblage of lenses, panel (c) shows the probability, $\mathcal{P}(z)$, that a streamline at height z goes through a lens as a function of the fractional flow, $\mathcal{F}$, through each lens. The three profiles shown in (c) correspond to $\mathcal{F} = 0.4, 0.5, 0.6$ for the cases $\mathcal{F} < 1/2$, $\mathcal{F} = 1/2$, and $\mathcal{F} > 1/2$ respectively.

flow past a single lens of permeability k_2 in a channel of permeability k_1, the flow speed is given by

$$u_i = -\frac{k_i}{\mu}\frac{\partial p}{\partial x} \quad \text{for} \quad i = 1, 2 \tag{2.1}$$

where u_2 and u_1 are the flow speeds inside and outside the lens respectively, and p is the pressure. If the total flux is $Q = u_1(H-h) + u_2 h$, then we can solve for the pressure gradient to determine the flow speeds.

$$u_2 = \frac{k_2 Q}{k_1(H-h) + k_2 h} \quad \text{and} \quad u_1 = \frac{k_1 Q}{k_1(H-h) + k_2 h}. \tag{2.2}$$

In the region of uniform permeability between successive lenses, the flow speed is given by $u_\infty = Q/H$. We deduce that a fraction $\mathcal{F}$ of the net flow passes through the lens where (cf. Woods (2015))

$$\mathcal{F} = \frac{k_2 h}{k_1(H-h) + k_2 h}. \tag{2.3}$$

Figures 2.3(a)-(c) show the pattern of streamlines as the flow passes a single lens located at three different vertical locations in the channel. In each case, approximately 7 out of the 21 streamlines across the channel are diverted into the lens, as highlighted in red. This is consistent with the fractional flow through the lens estimated using equation (2.3) ($\mathcal{F} \approx 0.34$).

Figure 2.3 illustrates that a lens whose centre is located at height z_c in the channel diverts streamlines from the region $z_c(1-\mathcal{F}) \le z \le z_c(1-\mathcal{F}) + \mathcal{F}$ of uniform parallel flow. In figures 2.4(a)-(b), the region between the dotted blue lines represents those streamlines in a uniform parallel flow which are diverted into a lens located at height z_c in the channel. For example, for $\mathcal{F} < 1/2$ (figure 2.4(a)), a streamline at height $z = \mathcal{F}$ passes through those lenses whose centres are located in the range $0 \le z_c \le \mathcal{F}/(1-\mathcal{F})$. The probability that a streamline which is originally at height z in a uniform flow passes through a lens which is randomly located in the channel is given by the length of the horizontal line at height z between the boundaries of the shaded zone in figures 2.4(a)-(b). With $\mathcal{F} < 1/2$ (figure 2.4(a)), the probability is less than 1 at all heights, while for $\mathcal{F} > 1/2$, there is an intermediate range of heights for which the probability is 1 (figure 2.4(b)). Based on figure 2.4(a), it follows that, for $\mathcal{F} < 1/2$, the

probability, $\mathcal{P}(z)$, that a streamline at height z is diverted through a lens is given by (see figure 2.4(c))

$$\mathcal{P}(z) = \begin{cases} \frac{z}{1-\mathcal{F}} & \text{for } z \leq \mathcal{F}, \\ \frac{\mathcal{F}}{1-\mathcal{F}} & \text{for } \mathcal{F} \leq z \leq 1-\mathcal{F}, \\ \frac{1-z}{1-\mathcal{F}} & \text{for } z \geq 1-\mathcal{F}. \end{cases} \tag{2.4}$$

Similarly, from figure 2.4(b), for $\mathcal{F} > 1/2$, a fraction of the streamlines near the centre of the channel pass through every lens in the channel, and therefore have a probability 1 of passing through a lens. The probability, $\mathcal{P}(z)$, is therefore given by (see figure 2.4(c))

$$\mathcal{P}(z) = \begin{cases} \frac{z}{1-\mathcal{F}} & \text{for } z \leq 1-\mathcal{F}, \\ 1 & \text{for } 1-\mathcal{F} \leq z \leq \mathcal{F}, \\ \frac{1-z}{1-\mathcal{F}} & \text{for } z \geq \mathcal{F}. \end{cases} \tag{2.5}$$

The case $\mathcal{F} = 1/2$ represents the limit for which only the streamline in the centre of the channel passes through every lens in the channel with probability 1. The probability for this limiting case is indicated in red in figure 2.4(c).

Given the probability of a streamline being diverted into a lens, in the next section, we calculate the travel times along individual streamlines across the channel.

2.2.2 Travel times along individual streamlines

In order to evaluate the travel times along individual streamlines, we begin by estimating the travel time along streamlines that are diverted through a lens and along those streamlines that do not pass through the lens. For the flow past a lens whose centre is located at (x_c, z_c), the expected travel time along a given streamline in moving through a region of length $L(> l)$, which is defined from $x = x_c(j) - L/2$ to $x = x_c(j) + L/2$, is given by the approximate expression

$$t_i = \frac{l}{u_i} + \frac{L-l}{u_\infty} \quad \text{for} \quad i = 1, 2 \tag{2.6}$$

where $i = 2$ corresponds to the streamlines that pass through the lens and $i = 1$ corresponds to the streamlines that do not pass through the lens (see equation

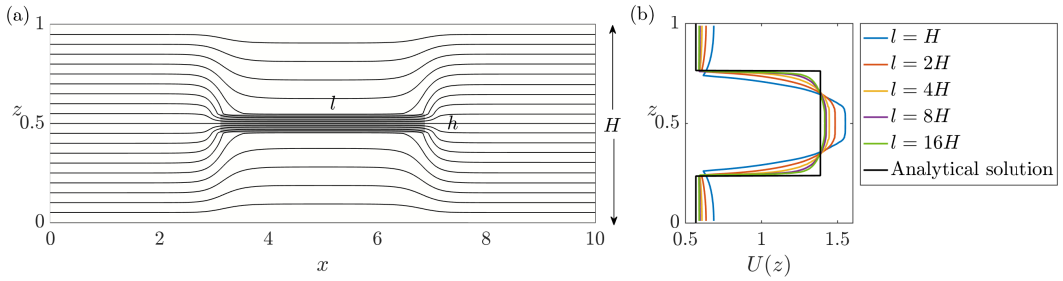

Figure 2.5 (a) Streamlines for the flow past a rectangular lens of length $l = 4H = 4$, width $h/H = 0.1$, and permeability ratio $k_2/k_1 = 10$. (b) The mean flow speed, $U(z)$, as estimated from equation (2.8) (black profile), and from numerical simulations for different values of the length of the lens, l. In each case the mean speed is estimated in the region $0 \le x \le 2l$, with the lens centred at $x = l$, so that the analytical solution is the same (cf. equation (2.8)).

(2.2)). Here we neglect the time to transition from parallel uniform flow to the parallel flow in the region containing the lens (cf. figure 2.2(a)). This approximation is valid in the case that the travel time across this transition zone is short compared to the travel time along the lens and in the uniform flow region between successive lenses. Since in the transition zone at the ends of the lenses the flow is two-dimensional and adjusts between these two parallel flow regimes over a region whose length scales with the width of the channel, $H(\ll l)$, we can neglect this adjustment zone when calculating the mean travel time of different streamlines provided that

$$\frac{H}{l} \ll \min\left(\frac{h}{H} + \frac{k_1}{k_2}\left(1 - \frac{h}{H}\right),\ \left(1 - \frac{h}{H}\right) + \frac{k_2}{k_1}\left(\frac{h}{H}\right)\right) \quad \text{and} \quad \frac{H}{l} \ll \left(\frac{L}{l} - 1\right), \tag{2.7}$$

where the two expressions within the right hand side of the first inequality correspond to the dimensionless travel times of the streamlines that pass through the lens and that do not pass through the lens, where the time has been scaled by Hl/Q. Given the travel time along individual streamlines (equation (2.6)), the mean flow speed along each streamline is thereby given by

$$U = \frac{L}{L/u_i + (L-l)/u_\infty} = \frac{u_i u_\infty}{u_\infty + (1 - l/L)u_i} \quad \text{for} \quad i = 1, 2. \tag{2.8}$$

In order to quantify the accuracy of this approximate solution for the mean flow speed, we compare this with the profiles of the mean flow speed obtained from the numerical simulations described in appendix A (figure 2.5). As an example, figure 2.5(a) shows the streamlines for the flow past a single lens of length $l = 4H$ placed in the centre of the channel. Figure 2.5(b) shows the mean flow speed, $U(z)$, as a function of the vertical location, z, in the channel. The different curves in figure 2.5(b) show the numerical calculations for several values of the length of the lens, l, where the channel width is kept constant ($H = 1$). In each case, the mean flow speed is calculated in the region $0 \leq x \leq L = 2l$, where the centre of the lens is at $(x_c = l, z_c = 0.5)$ (see appendix A). The black curve in figure 2.5(b) represents the approximate solution for the mean flow speed obtained from equation (2.8), which depends on the fractional flow, $\mathcal{F}$, through the lens estimated from equation (2.3). The figure shows that results from the full numerical simulations are well approximated by equation (2.8) as the length of the lens relative to the channel width is increased, in accordance with equation (2.7).

2.2.3 Flow through an assemblage of lenses

Given the travel time along individual streamlines and the probability of a streamline being diverted into a lens, we can now calculate the average travel time, and hence the mean speed, along individual streamlines in a channel which contains many lenses in sequence. We assume that the horizontal locations of successive lenses are given by $x_c(j) = (2j-1)L/2$ for $j = 1, ..., n$ $(L > l)$.

With a series of lenses, each located in sequence down the channel but at a series of random positions across the channel, there is a range of possible travel times along each streamline. For the flow past one lens, we assume that a streamline at height z in the channel has two possible travel times, t_2 and t_1, each with probability $\mathcal{P}(z)$ and $(1 - \mathcal{P}(z))$ respectively, corresponding to streamlines which enter the lens and those which flow around the lens (cf. §2.2.1 and §2.2.2). For flow past two lenses, there are three possible travel times, $2t_2$, $(t_2 + t_1)$, and $2t_2$, each with probability, $\mathcal{P}^2(z)$, $2\mathcal{P}(z)(1 - \mathcal{P}(z))$, and $(1 - \mathcal{P}(z))^2$ respectively. After n lenses, there are $(n + 1)$ possible travel times, each with probabilities given by the terms in the binomial expansion of $(\mathcal{P}(z) + (1 - \mathcal{P}(z)))^n$. In figure 2.6, we plot this discrete distribution of probabilities of travel times for the flow along three specific streamlines located

at three heights, $z = 0.15, 0.25, 0.5$. This is shown by the blue curves in figure 2.6 corresponding to the cases in which the tracer has passed through $n = 1, 5, 10$ and 50 lenses.

In the limit of large n, this binomial distribution of residence times converges to a normal distribution for $0 < \mathcal{P} < 1$, so that the residence time distribution (RTD) is given by

$$\mathrm{RTD}(x = nL, z, t) = \frac{1}{\sqrt{2\pi n\sigma_t^2(z)}} \exp\left(\frac{(t - nt_m(z))^2}{2n\sigma_t^2(z)}\right). \tag{2.9}$$

This is shown by the red curves in figure 2.6. The mean travel time, $t_m(z)$, and the variance of travel time, $\sigma_t^2(z)$, are determined from the probability $\mathcal{P}(z)$ (cf. figure 2.4(c)) and are given by

$$t_m(z) = t_2\mathcal{P}(z) + t_1(1 - \mathcal{P}(z)), \tag{2.10a}$$
$$\sigma_t^2(z) = (t_2 - t_1)^2\mathcal{P}(z)(1 - \mathcal{P}(z)), \tag{2.10b}$$

where t_2 and t_1 are travel times along the streamlines that pass through the lens and along the streamlines that do not pass through the lens (equation (2.6)).

Note that for a streamline with $P = 0$ (a streamline at the boundary) or $P = 1$ (a streamline that passes through every lens in the channel), $\sigma_t^2(z) = 0$. Figure 2.7(a) shows the root mean squared difference, $\epsilon(z)$, between the discrete probabilities and the prediction for a normal distribution (equation (2.9)) at each height z in the channel. For a given number of lenses, the difference is smallest when $\mathcal{P} = 1/2$ and increases as $\mathcal{P} \to 0$ or 1. We define the vertical average of the root mean squared difference, $\bar{\epsilon}$, as a function of the number of lenses that the flow has passed through. Figure 2.7(c) shows that $\bar{\epsilon}$ decays rapidly as the number of lenses that the flow has passed through increases, with $\bar{\epsilon} < 0.1$ for $n \geq 3$ lenses and $\bar{\epsilon} < 0.02$ for $n \geq 20$ lenses.

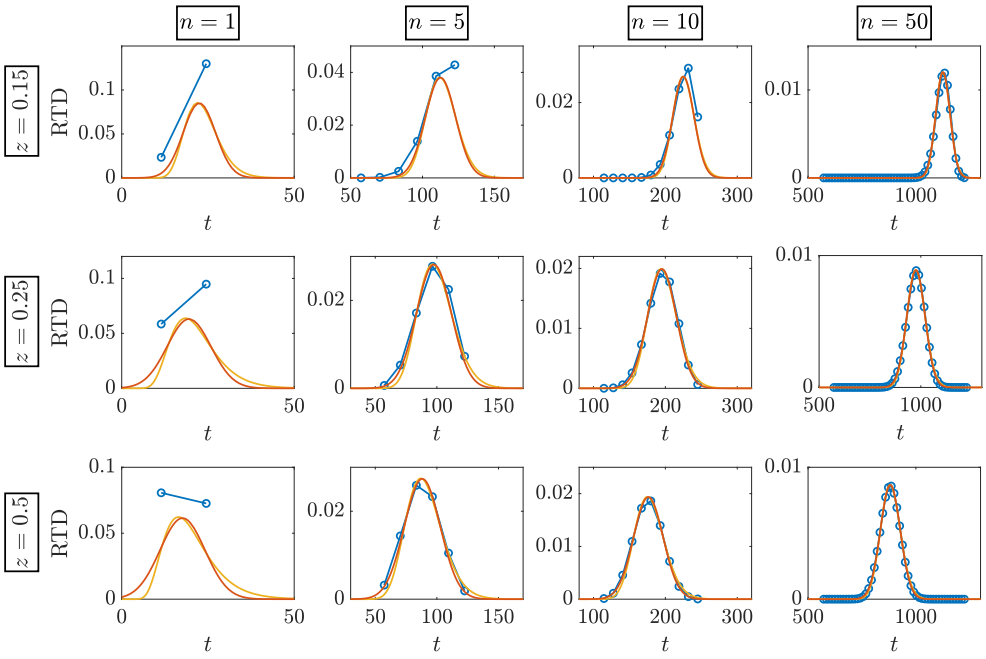

Figure 2.6 Residence time distributions (RTD) at three different vertical locations in the channel for a pulse of tracer released instantaneously into the flow at $x = 0$, $t = 0$. The arrival times are estimated at the downstream location $x = nL$ once the tracer has passed through $n = 1, 5, 10, 50$ lenses respectively and are shown here at three vertical locations, $z = 0.15, 0.25, 0.5$. The blue curves represent the discrete probabilities described in §2.2.3, normalised so that the area under each curve is 1. The red curves are given by equation (2.9). The yellow curves are obtained using the continuum model for the flow given by equation (2.14). The profiles shown here correspond to lenses with $k_2/k_1 = 10$, $h/H = 0.05$, $l/H = 10$, and $L = 2l = 20$.

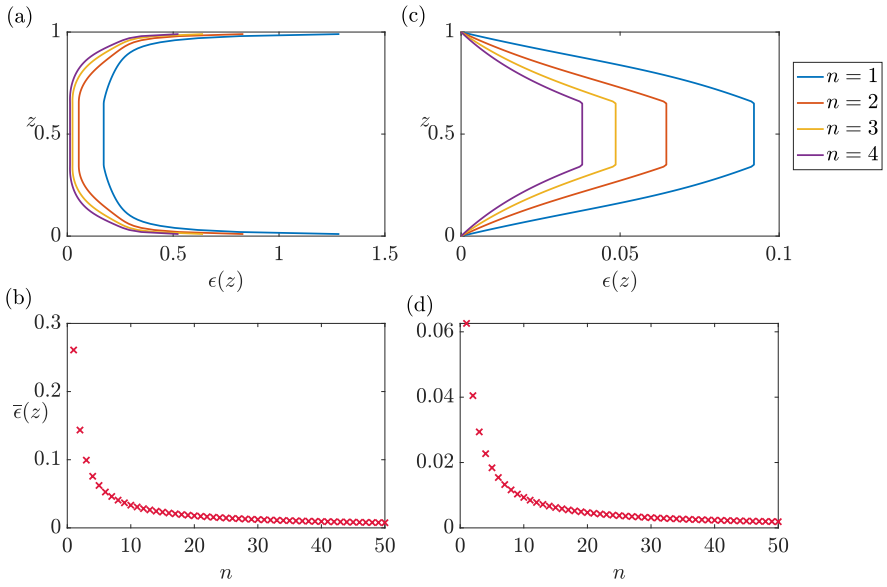

Figure 2.7 (a) The root mean squared difference between the discrete probability (blue curves in figure 2.6) and the normal approximation to the binomial distribution (red curves in figure 2.6) at each vertical height, z, in the channel. (c) The root mean squared difference between equation (2.9) (red curves in figure 2.6) and the residence times obtained from the continuum model given by equation (2.14) (yellow curves in figure 2.6) at each vertical height, z, in the channel. The four curves (purple, blue, green, yellow) in panels (a) and (c) correspond to the root mean squared difference after the flow has passed through $n = 1, 2, 3, 4$ lenses respectively. Panels (b) and (d) show the vertically averaged root mean squared difference, $\bar{\epsilon}$, corresponding to panels (a) and (c), as a function of the number of lenses, n, that the mean flow has passed through.

2.2.4 Continuum model for the flow through an assemblage of lenses

The residence time distribution (RTD, equation (2.9)) describes the probability distribution for tracer arrival at a specific location downstream of each lens as a function of time, t. However, many models are based on studying the distribution of tracer in space and its evolution in time. Following the work of Levenspiel and Smith (1957), we expect that the tracer concentration over a distance L can be described by a mean flow, $U(z)$, related to the mean travel time, and a longitudinal dispersion coefficient, $D(z)$, according to the relations (cf. equation (2.10))

$$U(z) = \frac{L}{t_m(z)} \quad \text{and} \quad D(z) = \frac{1}{2}L^2\frac{\sigma_t^2(z)}{t_m^3(z)}. \tag{2.11}$$

The evolution of tracer concentration at each height z can then be expressed in terms of the along-channel averaged conservation equation,

$$c_t + U(z)\, c_x = D(z)\, c_{xx}, \tag{2.12}$$

provided that $x = nL \gg D/U$, which requires that

$$n \gg \frac{\sigma_t^2(z)}{2t_m^2(z)} \gg \frac{(t_2 - t_1)^2\mathcal{P}(z)(1-\mathcal{P}(z))}{2(t_2\mathcal{P}(z) + t_1(1-\mathcal{P}(z)))^2}. \tag{2.13}$$

If a pulse of tracer of unit volume is injected instantaneously into the fluid at $t = 0$, equation (2.12) has a well-known solution,

$$c(x,z,t) = \frac{c_o H}{2\sqrt{\pi D(z)t}} \exp\left(-\frac{(x - U(z)t)^2}{4D(z)t}\right). \tag{2.14}$$

For comparison in figure 2.6, we have used the solution given by equation (2.14) to estimate the distribution of arrival times at $x = nL$ for a pulse of tracer released instantaneously into the flow at $x = 0$ and $t = 0$. This is shown by the yellow curves in figure 2.6. The root mean square difference between the continuum model given by equation (2.14) (yellow curves) and the normalised probability distribution of arrival times given by equation (2.9) (red curves) is calculated at each height, z, and is represented by $\epsilon(z,n)$ for the flow past n lenses (figure 2.7(b)). We take a vertical average of the root mean squared difference and denote it as $\bar{\epsilon}(n)$ (figure 2.7(b)). We find that $\bar{\epsilon} < 0.05$ for $n \geq 2$

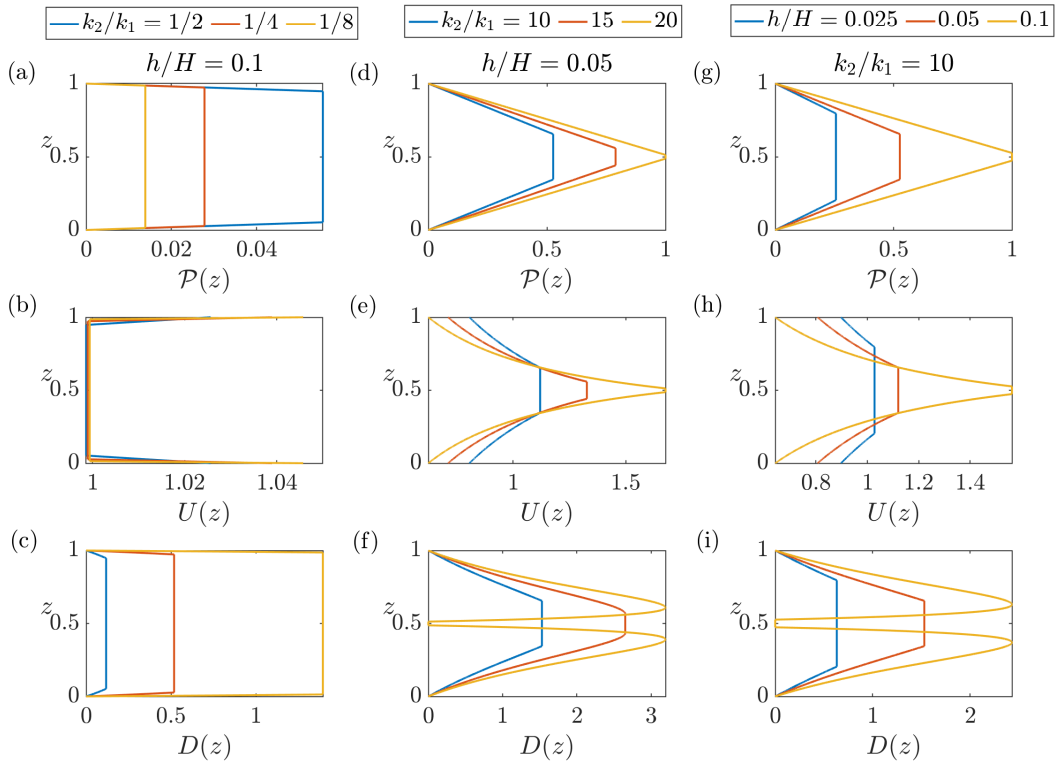

Figure 2.8 $l/H = 10$, $L = 2l = 20$. The profiles of the probability, $\mathcal{P}(z)$ (cf. figure 2.4(c)), mean speed, $U(z)$, and dispersion coefficient, $D(z)$ (equation (2.11)), for a range of values of permeability ratio, k_2/k_1, and width ratio, h/H, of the lens to the channel. Panels (a)-(c) correspond to low permeability lenses with $h/H = 0.1$. Panels (d)-(f) correspond to high permeability lenses with $h/H = 0.05$. Panels (g)-(i) correspond to high permeability lenses with $k_2/k_1 = 10$ and varying width ratio h/H.

(figure 2.7(d)). Furthermore, note that equations (2.14) (yellow curves) and (2.9) (red curves) are analogous once the flow has advanced sufficiently far so that $x \gg D/U$.

As seen in figure 2.7(d), we find that the continuum model given by equation (2.14) provides a good approximation for the expected travel time of tracer once the tracer has passed through $n \geq 2$ lenses. We therefore use profiles of mean speed, $U(z)$, and longitudinal dispersion coefficient, $D(z)$, to describe the transport of tracer as it passes through an assemblage of lenses. It is also important to note that equation (2.14) strictly represents the probability distribution of the arrival of tracer at a particular point in space and time, although we refer to $c(x, z, t)$ as the concentration of tracer.

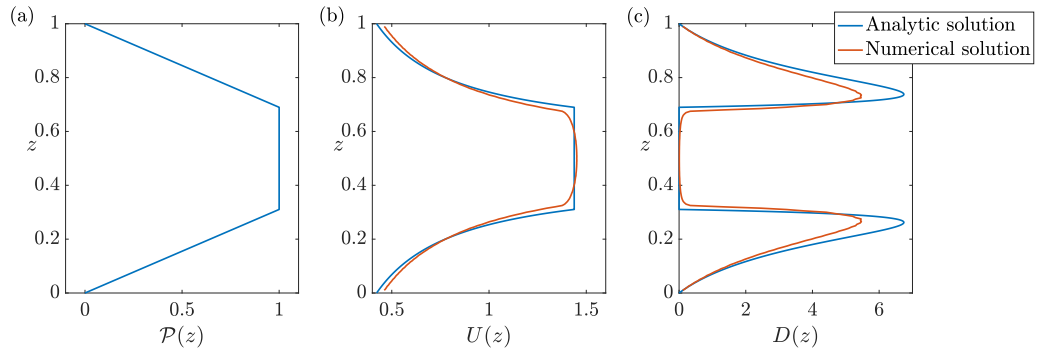

Figure 2.9 $k_2/k_1 = 20$, $h/H = 0.1$, $l/H = 10$, $L = 2l = 20$. The profiles of the probability, $\mathcal{P}(z)$ (cf. figure 2.4(c)), mean speed, $U(z)$, and dispersion coefficient, $D(z)$ (equation (2.11)), compared to the equivalent profiles from the numerical simulations. The numerical solution shown here is obtained by calculating the travel times along individual streamlines for $N = 101$ vertical positions of the lens in the channel. In the Nth numerical simulation, the lens has vertical position given by $z_c = (i-1)H/(N-1)$ (see appendix A).

2.2.5 Dependence on the properties of the lenses

Figure 2.8 shows the profiles of probability, $\mathcal{P}(z)$ (cf. figure 2.4(c)), mean speed, $U(z)$, and longitudinal dispersion coefficient, $D(z)$ (equation (2.11)), for a range of values of the permeability ratio, k_2/k_1, and width ratio, h/H, of the lens to the channel. Note that $k_2/k_1 < 1$ represents lenses with permeability lower than the background permeability, which we refer to as low permeability lenses, and $k_2/k_1 > 1$ represents high permeability lenses. Figure 2.8 illustrates that the shear becomes stronger as either (i) the magnitude of the permeability contrast between the lens and the background is increased, or (ii) as the cross-layer width of the lens relative to the channel increases, since this leads to a greater fractional flow through the lens.

As the fractional flow through a lens increases, the probability of a streamline passing through a lens increases (cf. figure 2.4(c)). As a result, the shear becomes increasingly stronger as the permeability contrast, k_2/k_1, and the width ratio, h/H, increase. On the other hand, for a low permeability lens, the fractional flow is always a small fraction of the net flow, and so the probability, $\mathcal{P}(z)$, is nearly constant across the channel except in a narrow region near the top and bottom boundaries (figures 2.8(a)-(c)). As a result, there is a narrow region of shear near each boundary and the mean speed in the centre of the channel is uniform.

For fractional flow $\mathcal{F} \geq 1/2$, a fraction of streamlines near the centre of the channel go through all lenses, with a probability of 1 (cf. figure 2.4(c) and figure 2.9(a)). Therefore, the travel times along all of these streamlines is constant, and consequently, the travel time variance, σ_t^2, and the longitudinal dispersion coefficient, D, are zero along those streamlines (figure 2.9(c)). The fluid parcels travelling along these streamlines are simply advected with a constant mean flow speed, with the shear confined to a region closer to the edge of the channel (figure 2.9(b)). However, in practice, the streamlines which are diverted to the region close to the edge of the lens have a different transition time adjusting from parallel uniform flow to parallel flow in the lens, than those which pass through the centre of the lens (see figure 2.5), and this leads to a small dispersion coefficient along those streamlines. We can quantify this dispersion with a full numerical simulation of the flow (see appendix A). The profiles of $U(z)$ and $D(z)$ using the full numerical solution are shown in figures 2.9(b)-(c). We find that in our numerical simulations, the transition zone near the ends of the lenses leads to a somewhat smoother distribution of the mean speed and dispersion coefficient at the edges of the region where all streamlines pass through every lens. However, inside this region, the dispersion coefficient, $D(z)$, is very small, as expected from the idealised approximate solution.

2.2.6 Dependence on the separation distance between lenses

The profiles in figure 2.8 correspond to an assemblage of lenses where the horizontal distance between successive lenses, $(L-l)$, is equal to the length of individual lenses, l. This assumes that the flow readjusts over a distance $\ll l$ after passing through each lens. As L/l is increased, the flow passes through a region of length $(L-l)$ with nearly parallel flow before entering the next lens (cf. equation (2.6)). The variation of mean speed, $U(z)$, and the longitudinal dispersion coefficient, $D(z)$, with height, z, in the channel are shown in figure 2.10 for a range of values of L/l. This illustrates the reduction in the magnitude of shear as the horizontal distance between successive lenses is increased since the shear due to the lenses is averaged with the uniform flow which develops between successive lenses (equation (2.8)). Similarly, we also see a reduction in the magnitude of the dispersion coefficient corresponding to a reduction in the variance of the travel times (cf. equation (2.11)).

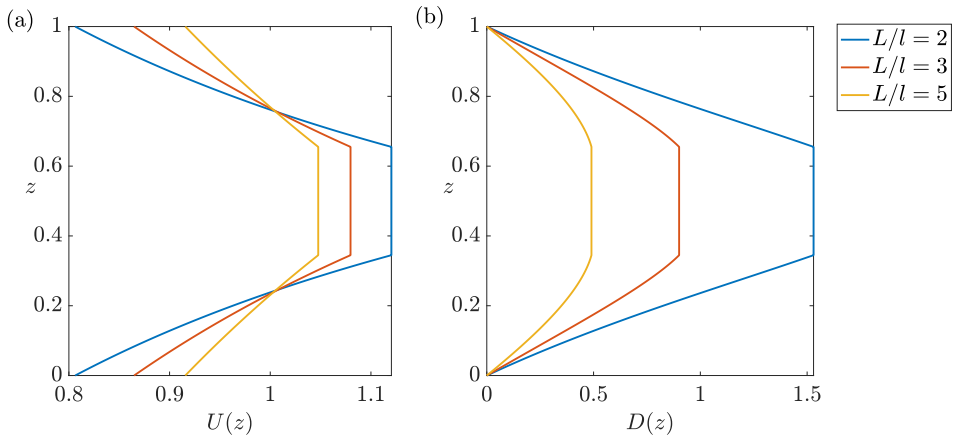

Figure 2.10 $k_2/k_1 = 10$, $h/H = 0.05$. The profiles of mean speed, $U(z)$, and dispersion coefficient, $D(z)$, shown here for different values of the separation distance between successive lenses, $(L - l)$.

2.3 Depth-averaged model for tracer transport

Given the continuum description for the probability distribution of a pulse of tracer released into the flow, we now explore the evolution of the vertical integral of the concentration as a function of time and horizontal distance from the point of release. This depends on the properties of $U(z)$ and $D(z)$ which vary with the vertical location in the channel. We develop an asymptotic model for the long time depth-averaged distribution of a pulse of tracer, and we explore the adjustment to this long time solution from the initial Fickian spreading of a pulse of tracer as the shear becomes more dominant in controlling the spreading.

Figures 2.11(b)-(e) show the evolution of a pulse of tracer released into the channel at $x = 0$, $0 < (z/H) < 1$, and $t = 0$ as determined by the solution to equation (2.12). The channel consists of lenses of permeability ratio $k_2/k_1 = 10$ and width ratio $h/H = 0.05$. The figures correspond to the concentration profile, $c(x, z, t = nL/\bar{U})$, estimated using equation (2.14) after the tracer has passed through $n = 1, 10, 100, 1000$ lenses respectively. The red dotted line corresponds to the mean location of the tracer front, which is advection-driven with speed $U(z)$. The variance around this mean profile corresponds to the expected spreading due to the random positioning of lenses in the domain. Although we have developed this two-dimensional picture of the tracer dispersal, it is useful to extract the depth-averaged properties of the tracer in order to

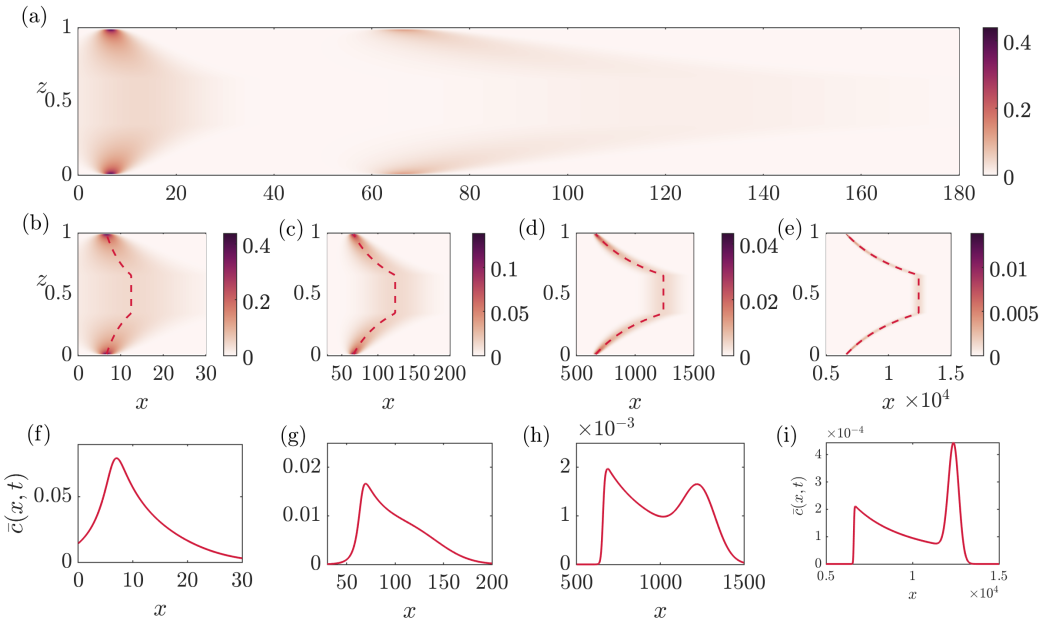

Figure 2.11 $k_2/k_1 = 10$, $h/H = 0.05$, $l/H = 10$. (a) Evolution of tracer concentration at two different times after its initial release at $x = 0$, $t = 0$. In panels (b)-(e), the colours correspond to the concentration, $c(x, z, t = nL/\bar{U})$, after it has passed through $n = 1, 10, 100, 1000$ lenses respectively, where the time taken to go through n lenses is given by $t = nL/\bar{U}$. Panels (f)-(i) show the corresponding depth-averaged profiles, $\bar{c}(x, t = nL/\bar{U})$, for the concentration profiles shown in panels (b)-(e) respectively.

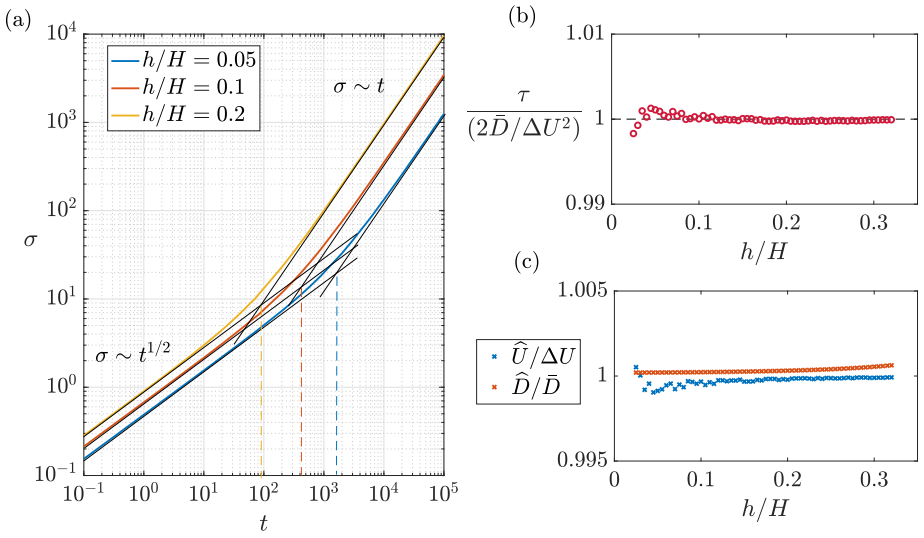

Figure 2.12 $k_2/k_1 = 2$, $l/H = 10$. (a) The standard deviation, σ, plotted as a function of time, t, for three different values of width ratio, h/H, showing the transition from Fickian to shear-driven spreading of tracer. (b) The red circles represent the non-dimensional transition time, $\tau/(2\bar{D}/\Delta U^2)$, as a function of the width ratio, h/H. The transition time, τ, is estimated numerically as the intersection between the two black curves in panel (a). The black dotted line in panel (b) represents $\tau = 2\bar{D}/\Delta U^2$. (c) Variation of $\widehat{D}/\bar{D}$ and $\widehat{U}/\Delta U$ for a range of values of h/H where $\sigma = (2\widehat{D}t)^{1/2}$ and $\sigma = \widehat{U}t$ as represented by the black lines in panel (a).

build a one-dimensional model of the tracer transport in this heterogeneous porous channel. We define a depth-averaged concentration,

$$\bar{c}(x,t) = \frac{1}{H}\int_0^H c(x,z,t)\mathrm{d}z. \tag{2.15}$$

Figures 2.11(f)-(i) show this depth-averaged concentration profile once the tracer has passed through $n = 1, 10, 100, 1000$ lenses respectively. Based on these depth-averaged profiles, we have estimated the mean position of the centre of mass of tracer, $x_m(t)$, and the variance of longitudinal extent of the tracer, relative to the mean, $\sigma^2(t)$, as

$$x_m(t) = \frac{\int_{-\infty}^{\infty}\bar{c}(x,t)x\mathrm{d}x}{\int_{-\infty}^{\infty}\bar{c}(x,t)\mathrm{d}x}, \tag{2.16a}$$

$$\sigma^2(t) = \frac{\int_{-\infty}^{\infty}\bar{c}(x,t)(x-x_m(t))^2\mathrm{d}x}{\int_{-\infty}^{\infty}\bar{c}(x,t)\mathrm{d}x}. \tag{2.16b}$$

Figure 2.12(a) illustrates the evolution of the variance of the tracer, σ, with time, t, corresponding to the calculations shown in figure 2.11. At early times, σ grows as $t^{1/2}$ but at late times, the spreading of tracer becomes controlled by the effective mean shear and grows linearly with time t. We define $\widehat{D}$ by fitting the curve $\sigma \approx (2\widehat{D}t)^{1/2}$ to the numerical data at early times (dispersion controlled regime), while at late times, we define $\widehat{U}$ by fitting the curve $\sigma \approx \widehat{U}t$ (shear controlled regime) (figure 2.12(a)). We expect the transition from the early to the long time regime to be given by a transition time, τ, which is found by matching the early time and late time solutions, $\tau = 2\widehat{D}/\widehat{U}^2$. Furthermore, using the properties of the mean flow and dispersion at each height in the channel, we can define the following quantities

$$\Delta U^2 = \frac{1}{H}\int_0^H (U(z) - \bar{U})^2 \mathrm{d}z, \tag{2.17a}$$

$$\bar{U} = \frac{1}{H}\int_0^H U(z)\mathrm{d}z, \tag{2.17b}$$

$$\bar{D} = \frac{1}{H}\int_0^H D(z)\mathrm{d}z. \tag{2.17c}$$

Figure 2.12(b) shows the non-dimensional transition time, $\tau/(2\bar{D}/\Delta U^2)$, plotted for different values of the cross-layer scale of the lens relative to the channel width, h/H. We find that the difference between the black dotted line and the red curves is less than 0.1% for $0.025 \leq h/H \leq 0.32$, suggesting that to leading order, the transition time may indeed be described as $\tau \approx 2\bar{D}/\Delta U^2$. Consequently, the quantities defined in equation (2.17) may be used to provide an estimate for $\widehat{D}$ and $\widehat{U}$ as obtained from the numerical results (figure 2.12(a)). Indeed, figure 2.12(c) shows $\widehat{D}/\bar{D}$ and $\widehat{U}/\Delta U$ as a function of h/H, illustrating that $\widehat{D}$ and $\widehat{U}$ are within 0.01% of $\bar{D}$ and ΔU. Some of the fluctuations in the figures 2.12(b)-(c) may be a result of the limits of our numerical calculation.

2.3.1 Asymptotic solutions for the depth-averaged profile

Figure 2.13(a) shows a typical profile of the late-time depth-averaged concentration. For the flow with a given mean speed and dispersion, the evolution of

the depth-averaged concentration can be determined asymptotically at long times. This is described in the following sections for the case $\mathcal{F} < 1/2$, but these results can be readily generalised to the case $\mathcal{F} > 1/2$.

Regions with constant $U(z)$ and $D(z)$

At the leading edge of the flow, the profiles of the mean speed and dispersion, $U(z)$ and $D(z)$, are constant over a region $1 - \mathcal{F} \leq (z/H) \leq \mathcal{F}$. Therefore, in this region, the tracer advects with constant velocity, U_o, and spreads horizontally with a constant dispersion coefficient, D_o. The depth-averaged concentration in this region is therefore given by,

$$\bar{c}(x,t) = \frac{1}{H}\int_{\mathcal{F}H}^{(1-\mathcal{F})H} \frac{c_o H}{2\sqrt{\pi D_o t}} \exp\left(-\frac{(x-U_o t)^2}{4D_o t}\right) \mathrm{d}z, \tag{2.18}$$

where $U_o = U(z/H = 1/2) = U(\mathcal{F} \leq (z/H) \leq 1 - \mathcal{F})$ and $D_o = D(z/H = 1/2) = D(\mathcal{F} \leq (z/H) \leq 1 - \mathcal{F})$. Equation (2.18) may be expressed in the simpler form

$$\bar{c}(x,t) = \frac{c_o H(1-2\mathcal{F})}{2\sqrt{\pi D_o t}} \exp\left(-\frac{(x-U_o t)^2}{4D_o t}\right). \tag{2.19}$$

Figure 2.13(c) shows the product of the depth-averaged concentration, $\bar{c}(x,t)$, and $\sqrt{t}$ as a function of the normalised along-channel position, as calculated from a numerical solution of equation (2.12). This illustrates the convergence of the numerical solution at the leading edge to the asymptotic solution given by equation (2.19) at late times.

Regions with finite but smoothly varying $U(z)$ and $D(z)$

In the regions $0 < (z/H) \leq \mathcal{F}$ and $1 - \mathcal{F} \leq (z/H) < 1$, the profiles of $U(z)$ and $D(z)$ vary smoothly and so the tracer is sheared out. By symmetry, the depth-averaged concentration in this region is given by,

$$\bar{c}(x,t) = \frac{2}{H}\int_{0}^{\mathcal{F}H} \frac{c_o H}{2\sqrt{\pi D(z) t}} \exp\left(-\frac{(x-U(z)t)^2}{4D(z)t}\right) \mathrm{d}z. \tag{2.20}$$

At long times, at distance x downstream, the concentration of the tracer pulse at a given depth z_o decreases to zero at distances greater than a few multiples of the scale $\sqrt{D(z_o)t}$ where z_o is defined by the relation $x = U(z_o)t$.

If we move upwards or downwards a small distance δz, then to leading order, the pulse of tracer will have mean along-channel position $(U(z_o) + \delta z\, U'(z_o))t$. Therefore, at along-channel position $x = U(z_o)t$, the tracer concentration will fall to zero for distances greater than several multiples of the length scale $\delta z = \sqrt{D(z_o)t}/U'(z_o)t$ from the reference height z_o. At long times, the integral in equation (2.20) is dominated by the region $(z_o - n\delta z < z < z_o + n\delta z)$, where $n\delta z \ll H$ and $n \gg 1$, and has an approximate form

$$\bar{c}(x,t) \approx \frac{2}{H}\int_{-n\delta z}^{n\delta z} \frac{c_o H}{2\sqrt{\pi D(z_o)t}} \exp\left(-\frac{U'^2(z_o)t}{4D(z_o)}Z^2\right)\mathrm{d}Z, \tag{2.21}$$

where $Z = (z - z_o)$. At long times, we can evaluate the integral by extending the limits to infinity, which leads to the asymptotic result

$$\bar{c}(x,t) \approx \frac{2c_o H}{|U'(z_o)|t} \tag{2.22}$$

since $\int_{-\infty}^{\infty} \exp(-z^2)\mathrm{d}z = \sqrt{\pi}$.

Regions with finite $U(z)$ and $D(z) = 0$

At the boundaries of the domain, $z/H = 0$ and $z/H = 1$, the dispersion coefficient $D(0) = 0$ since the travel time variance, σ_t^2, is zero at the boundaries. By symmetry, at $z/H = 0$ and $z/H = 1$, the depth-averaged concentration is given by

$$\bar{c}(x,t) = \frac{2}{H}\int_0^{H/2} \frac{c_o H}{2\sqrt{\pi D(z)t}} \exp\left(-\frac{(x - U(z)t)^2}{4D(z)t}\right)\mathrm{d}z. \tag{2.23}$$

At large times, at along-channel position $x = U(0)t$, the integrand in equation (2.23) is dominated by the region $0 < z < n\delta z = n\sqrt{D'(0)t}/U'(0)t \ll H$, where $n \gg 1$. Now we can approximate the integral using a Taylor series expansion near $z = 0$, leading to the asymptotic result

$$\bar{c}(x,t) \approx \frac{2}{H}\int_0^{n\delta z} \frac{c_o H}{2\sqrt{\pi D'(0)tz}} \exp\left(-\frac{U'^2(0)t}{4D'(0)}z\right)\mathrm{d}z. \tag{2.24}$$

For large t, this has the approximate solution

$$\bar{c}(x,t) \approx \frac{2c_o H}{|U'(0)|t} \tag{2.25}$$

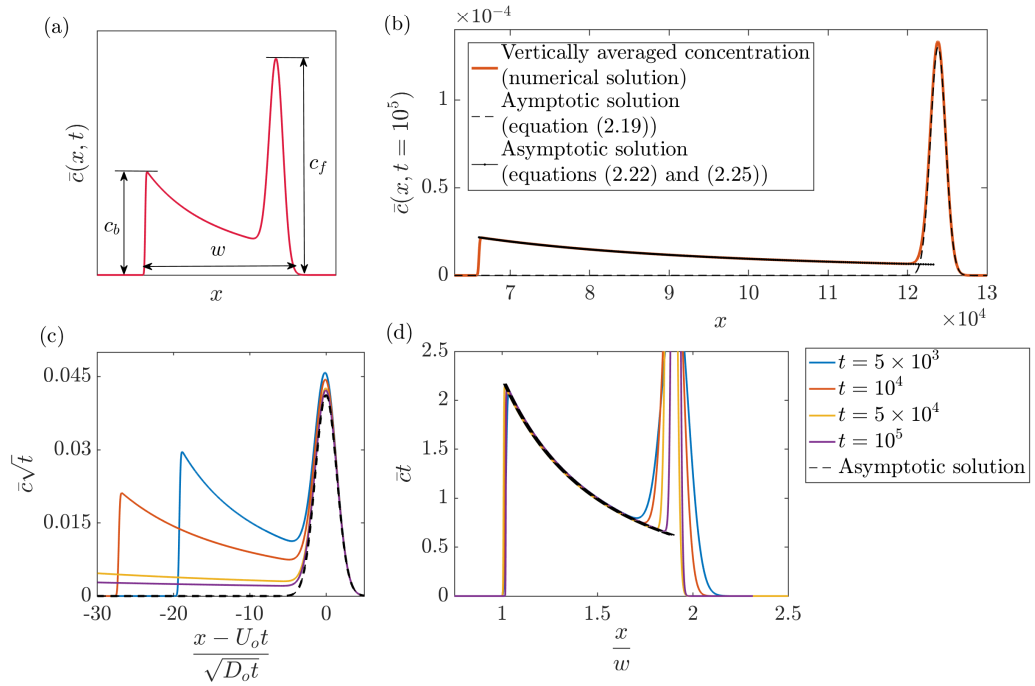

Figure 2.13 $k_2/k_1 = 10$, $h/H = 0.05$, $l/H = 10$. (a) Schematic of the depth-averaged concentration, $\bar{c}(x,t)$, showing the maximum concentration at the front, c_f, maximum concentration at the back, c_b, and the width of the pulse of tracer, w. (b) The depth-averaged concentration of tracer, $\bar{c}(x,t)$, plotted at $t = 10^5$ based on the depth-averaged concentration profile estimated using the numerical solution (orange curve) and the asymptotic solutions described in §2.3.1 (black curves). (c) The product of the depth-averaged concentration and $\sqrt{t}$, plotted as a function of the normalised along-channel position, $(x - U_o t)/\sqrt{D_o t}$, at several times illustrating the convergence of the front profile to the asymptotic solution given by equation (2.19) at late times. (d) The product of the depth-averaged concentration and time, t, plotted as a function of the normalised along-channel position, x/w, at several times, illustrating the convergence of the profile to the asymptotic solution given by equations (2.22) and (2.25) behind the leading edge at late times.

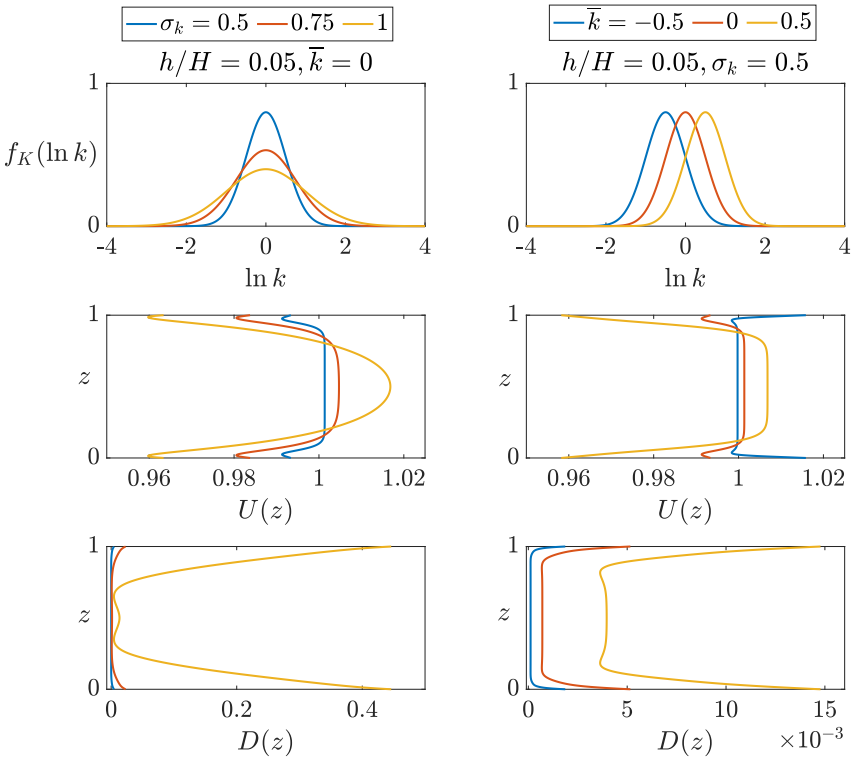

Figure 2.14 For a given log-normal distribution of permeability, the figure shows the profiles of log-normal probability density function (equation (2.26)), mean speed, $U(z)$, and dispersion coefficient, $D(z)$ (equation (2.11)), for a range of values of standard deviation, σ_k, and mean permeability, $\bar{k}$, of the log-normal permeability distribution of the lenses. In these calculations, $L = 2l = 20$.

since $\int_0^\infty (1/\sqrt{z}) \exp(-z) \mathrm{d}z = \sqrt{\pi}$. Figure 2.13(d) shows the product of the depth-averaged concentration, $\bar{c}(x,t)$, and time, t, as a function of the normalised along-channel position, highlighting the convergence of the depth-averaged concentration profile behind the leading edge at long times. Figure 2.13(b) shows a comparison of the depth-averaged concentration profile from the full numerical solution of the flow and using the solutions described above at a late time, illustrating the convergence to the asymptotic solutions described in this section.

2.4 Log-normal distribution of lenses

Geological formations are often composed of regions with different permeability. Observational data suggests that the distributions of permeability in geological formations follow a log-normal distribution (Law, 1944). Assuming that the

formation is composed of long lenses with a log-normal distribution of permeability, the probability, $P_K(k)$, of a certain permeability, k, is given by a log-normal probability density function, $f_K(k)$. defined as

$$f_K(k) = \frac{1}{k\sigma_k\sqrt{2\pi}} \exp\left(- \frac{(\ln k - \bar{k})^2}{2\sigma_k^2} \right) \implies P_K(a \leq k \leq b) = \int_a^b f_K(k)\mathrm{d}k, \tag{2.26}$$

so that $\ln(K)$ is normally distributed, $K \sim \mathcal{N}(\bar{k}, \sigma_k^2)$. For an assemblage of lenses in a channel with a log-normal distribution of permeability given by equation (2.26), the mean travel time, $T_m(z)$, and the variance relative to this mean, σ_T^2, are given by (cf. equation (2.10))

$$T_m(z) = \int_0^\infty t_m(k; z) f_K(k)\mathrm{d}k, \tag{2.27a}$$

$$\sigma_T^2(z) = \int_0^\infty t_m^2(k; z) f_K(k)\mathrm{d}k - T_m^2(z). \tag{2.27b}$$

The profiles of $U(z)$ and $D(z)$ can then be obtained by substituting equation (2.27) for the mean and variance of travel time in equation (2.11). The resulting profiles of the mean flow speed, $U(z)$, and the longitudinal dispersion coefficient, $D(z)$, are shown in figure 2.14 for a range of values of $\bar{k}$ and σ_k. The profiles show that the shear and dispersion increase with increasing $\bar{k}$ or σ_k since the formation includes more high permeability lenses which divert a large fraction of the flow (cf. figure 2.8). Furthermore, the case with $\bar{k} = -0.5$ represents a channel with lenses whose mean permeability is less than the background permeability, and so the direction of shear is reversed. This is in accordance with the profiles of shear obtained for low permeability lenses, as shown in figure 2.8. In figure 2.14, the profiles of the mean shear for different mean permeability, $\bar{k}$, further highlight that in a geological formation, having high permeability baffles increases the shear significantly relative to a formation with thin low permeability baffles.

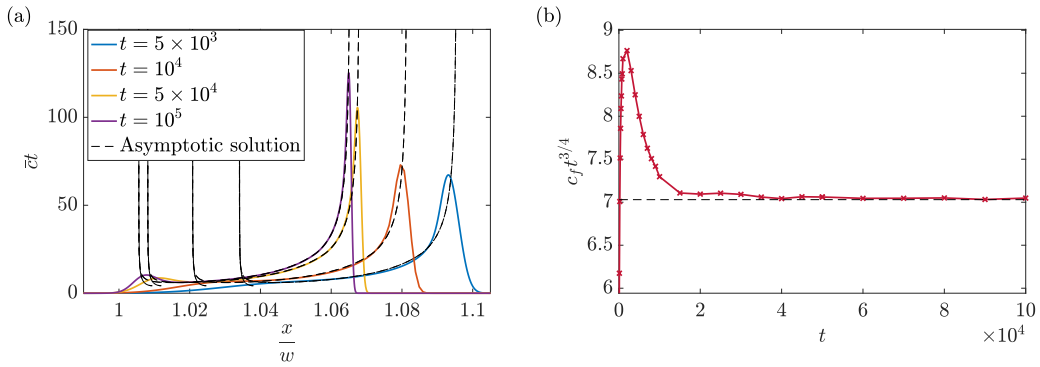

Figure 2.15 Calculations are shown here for a log-normal distribution of lenses with $\bar{k} = 0$, $\sigma_k = 1$, $h/H = 0.05$, $l/H = 10$. The asymptotic solutions are described in §2.4.1. (a) The product of the depth-averaged concentration and time, t, plotted as a function of the normalised along-channel position, x/w, at several times, illustrating the convergence of the profile to the asymptotic solution given by equation (2.30) at late times. (b) The product of the maximum concentration at the leading edge, c_f, and $t^{3/4}$ plotted as a function of time, t, showing convergence to equation (2.29) at long times. The black dotted line represents $c_f t^{3/4} = \eta_o$ (cf. equation (2.29)).

2.4.1 Asymptotic solution for the depth-averaged profile

In the case of a log-normal distribution of lenses, the profile of the mean flow speed, $U(z)$, varies gradually across the channel (see figure 2.14). At $z_o = 0.5$ we find that $U'(z_o) = 0$, and so the late-time depth-averaged concentration at along-channel position $x = U(0.5)t$ is dominated by the region a distance $n\delta z$ above and below $z_o = 0.5$, where $\delta z = (16D(0.5)/U''2(0.5)t)^{1/4}$, leading to the approximate expression for the depth-averaged concentration

$$\bar{c}(x,t) \sim \frac{c_o H}{2\sqrt{\pi D(0.5)t}} \int_{-n\delta z}^{n\delta z} \exp\left(-\frac{U''^2(0.5)t}{16D(0.5)} z^4\right) \mathrm{d}z, \tag{2.28}$$

where $n\delta z \ll H$ and $n \gg 1$. In this limit, the integral is given in terms of the Gamma function,

$$\bar{c}(x = U(0.5)t, t) \sim \frac{c_o H}{4\sqrt{\pi D(0.5)}} \left(\frac{16D(0.5)}{U''^2(0.5)t^3}\right)^{1/4} \Gamma\left(\frac{1}{4}\right) = \eta_o t^{-3/4} \tag{2.29}$$

since $\int_{-\infty}^{\infty} \exp(-az^4)\mathrm{d}z = \Gamma(1/4)/(2\sqrt[4]{a})$. Behind the leading edge, i.e., for $z \neq 0.5$ and at along-channel position $x = U(z_o)t$, the concentration follows the same solution as in §2.3.1,

$$\bar{c}(x,t) \approx \frac{2c_o H}{|U'(z_o)|t}. \tag{2.30}$$

Figure 2.15(a) shows the product of the depth-averaged concentration, $\bar{c}(x,t)$, and time, t, as a function of the normalised along-channel position, illustrating the convergence of the depth-averaged profile behind the leading edge to the asymptotic solution given by equation (2.30) at long times. Figure 2.15(b) shows the convergence of the front concentration, c_f, to the asymptotic solution given by equation (2.29) at long times.

2.5 Summary

In this chapter, we have analysed the dispersion of a passive tracer in a pressure-driven flow through a confined porous medium consisting of a random assemblage of long and thin lenses. We show that owing to the boundaries, a shear develops in the mean flow along the layer. We show that this shear controls the late time spreading of tracer injected into the flow, in contrast to the earlier phases of the spreading, which are controlled by Fickian dispersion associated with the heterogeneities (Dagan and Fiori, 2003; Eames and Bush, 1999).

In formations where the thickness of individual layers is typically $1-10$ m, and in which the permeability is log-normally distributed, the distance for transition from Fickian to shear-driven spreading can vary from $100-10000$ m for lenses of thickness $0.1-1$ m (figure 2.16). For example, for a layer in which $H = 10$ m and in which the permeability of the lenses is log-normally distributed with mean permeability $\bar{k} = 0$ and standard deviation $\sigma_k = 1$, the transition distance $d_\tau = \tau\bar{U}$ is shown as a function of h/H in figure 2.16(a). Figure 2.16(b) illustrates the strength of shear as a function of h/H, which shows that the shear becomes weaker as $h/H \to 0$, leading to a sharp increase in the distance for transition as the cross-layer width of the heterogeneity is decreased relative to the width of the individual layers. In the calculations shown here, the transition distance is $\mathcal{O}(1)$ km, illustrating that in layers consisting of thin heterogeneity with $h/H \ll 1$ or in layers with cross-layer

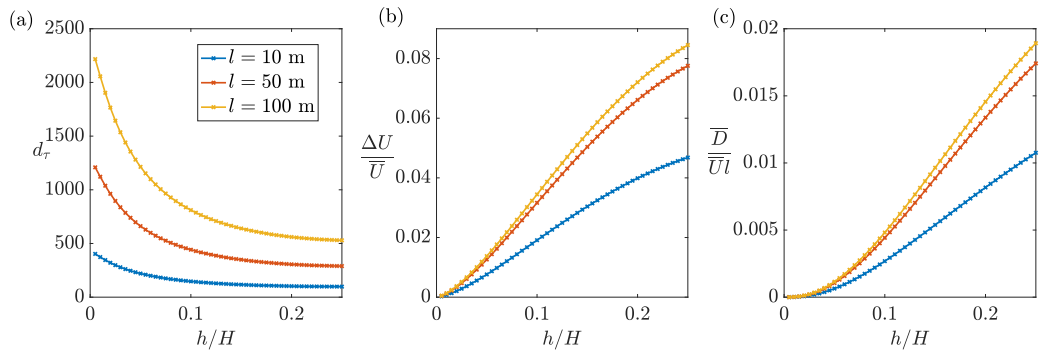

Figure 2.16 For a log-normal permeability distribution with $\bar{k} = 0$, $\sigma_k = 1$, the figure shows (a) the transition distance $d_\tau = \tau\bar{U}$, (b) the dimensionless strength of shear, $\Delta U/\bar{U}$, and (c) the dimensionless mean dispersion coefficient, $\bar{D}/\bar{U}l$, as a function of the cross-layer width of the heterogeneity to the width of the layer, h/H. The colours represent the length of the heterogeneity, l, in metres. In all cases, the horizontal separation distance, $(L - l)$, between successive lenses is 10 m, and the width of the channel is $H = 10$ m.

scale $H = 1$ metre, the distance for transition could range from as large as $\mathcal{O}(10)$ km to as small as $\mathcal{O}(10 - 100)$ m. Accurate estimate of the dispersion therefore requires quantification of the length scales of such heterogeneity in porous formations.

In the context of pollutant dispersal in groundwater, the initial width and vertical location of the pollutant determines how far the pollutants spread in the rock. Figure 2.1 shows two parcels of fluid, marked 1 and 2, one located at the centre of the formation and located close to the impermeable boundary at the top. As the figure illustrates, a parcel close to the centre travels approximately 15% farther in the along-flow direction than the parcel close to the edge, and the parcel close to the edge is more spread out due to larger dispersion near the boundary (see profiles of $U(z)$ and $D(z)$ for a log-normal distribution of permeability in figure 2.14). In a more heterogeneous rock where the permeability variations are larger and where the strength of shear is even larger, the difference in distance travelled between the two parcels could be significantly amplified. Furthermore, in the case of carbon sequestration, a difference in density and viscosity between carbon dioxide and the ambient brine could lead to a further amplification of this shear-driven spreading. Although the analysis for this specific case is beyond the scope of this thesis, this would form a fascinating and important extension of the present work.

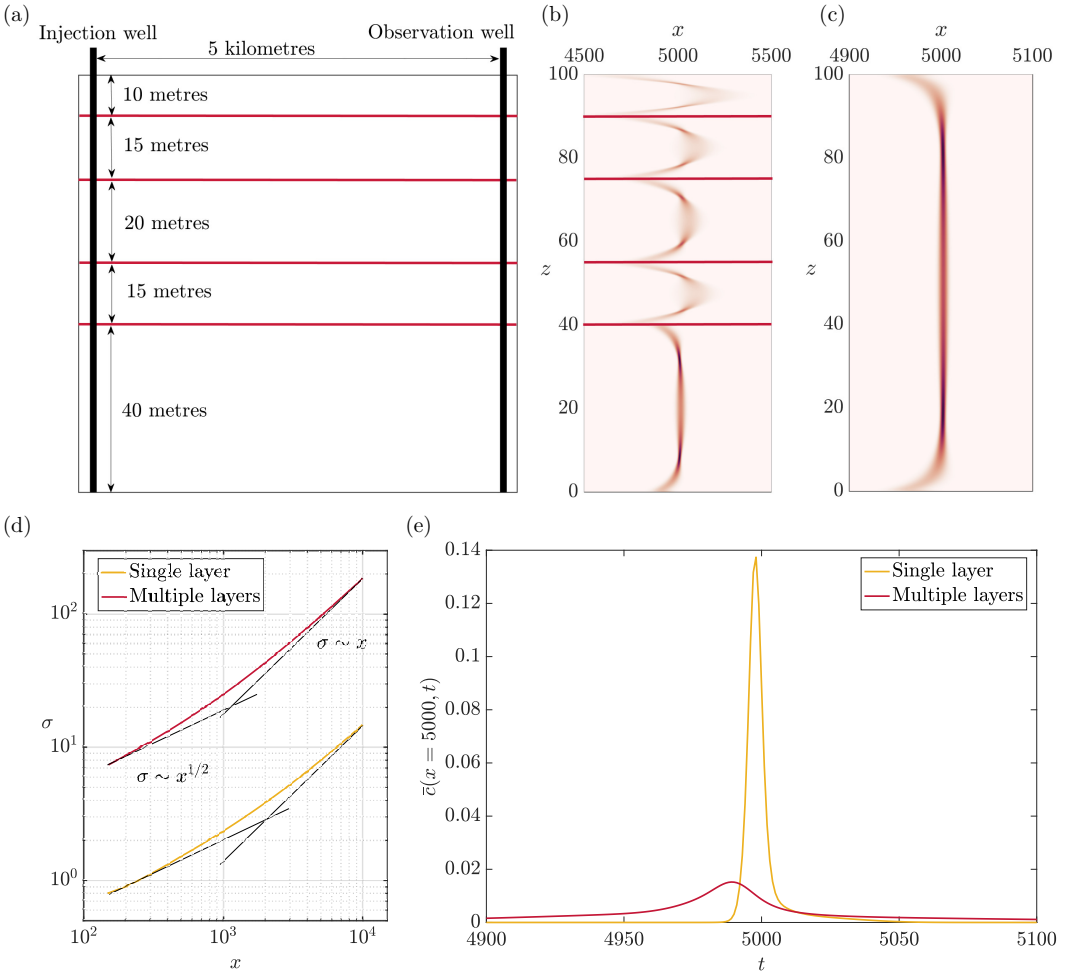

Figure 2.17 (a) A schematic of a layered heterogeneous formation, in which the total height of the layer is 100 m. The red horizontal lines represent low permeability layers which may or may not be fully impermeable. A pulse of tracer is released into the channel through the injection well (at $x = 0$) and sampled at an observation well which is located 5 km downstream (at $x = 5000$ m). The layers are assumed to consist of long thin lenses ($l = 100$ m and $h = 1$ m) and have the same log-normal distribution of permeability (mean permeability $\bar{k} = 0$ and standard deviation $\sigma_k = 1$). Panels (b) and (c) show the tracer concentration at $t = 5000$ assuming that the low permeability layers are impermeable and fully permeable respectively. (d) The standard deviation of the tracer, σ, plotted as a function of distance downstream, x, as it migrates down the layered heterogeneous rock. (e) The vertically averaged concentration profile, $\bar{c}(x, t)$, sampled at the observation well located at $x = 5000$, as a function of time, t, in a layered formation and in a formation with a single layer of equivalent depth.

Porous formations are often layered with high permeability layers alternating with thin low permeability layers of shale or clay. These low permeability layers may either be fully impermeable or have fractures causing fluid to migrate from one layer into another (see figure 2.17). In such formations, proper quantification of the locations of fractures is important in interpreting the results from tracer tests. For example, if a pulse of tracer is released into the formation through the injection well, and the formation consists of five layers with vertical extent 10, 15, 20, 15, and 40 m respectively, with each layer having the same properties, the spreading of tracer differs significantly depending on the permeability of the low permeability layers (figures 2.17(b)-(c)). An observation well located downstream of the injection well samples the vertically averaged concentration profile of the tracer as it arrives. As figure 2.17(e) illustrates, this observed profile can differ significantly depending on the properties of the low permeability layer. Assuming that the low permeability layers are fully permeable gives a weaker shear profile, whereas in fact tracer may be much more spread out due to the strong shear in individual layers. Additionally, at long times, the standard deviation of the pulse of tracer grows as x once the shear dominates the initial Fickian spreading (figure 2.17(d)).

Chapter 3

Dispersion in porous rocks with elliptic lenses

The material contained in this chapter and the previous chapter has been submitted for publication in *Journal of Fluid Mechanics*, under the title 'Boundary-induced shear and tracer transport in heterogeneous porous rock' (Bhamidipati and Woods, 2020a).

3.1 Introduction

In chapter 2, we examined the shear which arises as a result of a series of laterally extensive and relatively thin rectangular lenses of different permeability within a porous layer. On reaching each lens, the streamlines partition between those which move through the lens and those which remain in the surrounding formation. For a distribution of lenses along the channel which are located at random positions across the channel, we identified that streamlines near the boundary of the domain were less likely to pass through a lens than those in the centre of the domain. This leads to the generation of an effective shear in the flow when averaged over many lenses along the channel. In this chapter, we extend the analysis done in the previous chapter to consider the flow through elliptical lenses with length comparable to the channel width. In this limit, there is now a distribution of travel times associated with the different streamlines, depending on the time each streamline spends within the lens. We use numerical simulations to estimate the travel times along individual streamlines for the flow through individual lenses.

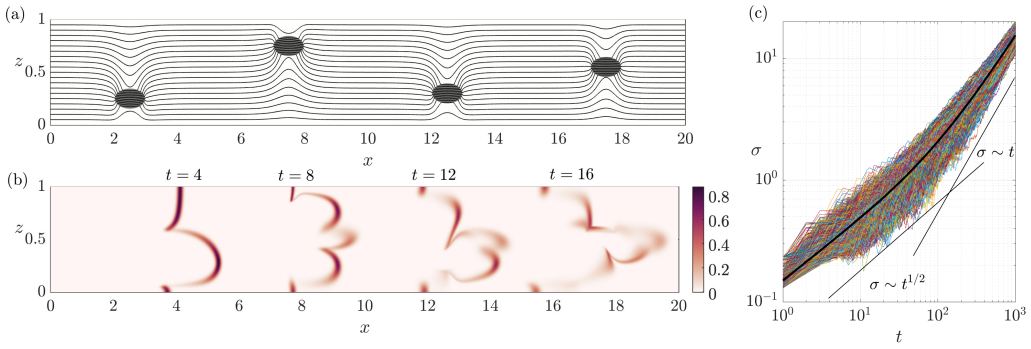

Figure 3.1 (a) Streamlines for flow through $n = 4$ lenses which are a horizontal distance $L = 5$ apart and at vertical locations $z_c = 0.25, 0.75, 0.3, 0.55$. (b) The plot shows the concentration, $c(x, z, t)$, of a pulse of dye at four times, $t = 4, 8, 12, 16$, after its initial release at $x = 0.25$ and $t = 0$. (c) The standard deviation of the spread of tracer, σ, plotted versus time, t, for 5000 realisations of the porous rock. The black curve represents the mean of the individual realisations.

Figure 3.1(a) shows the streamlines for a typical flow past four elliptical lenses, and 3.1(b) shows the shape of a pulse of dye as it passes each of the lenses in succession, illustrating the distortion of the dye. The numerical scheme used to generate these figures is described in appendix A. In order to quantify this distortion, and its variation as a function of the distance downstream, we have generated 5000 realisations of a porous channel with each realisation including a series of lenses whose centres are spaced a distance $L = 5$ apart. The vertical position of each lens is chosen to have a random position across the channel, each selected from one of the 81 uniformly distributed values in the interval $[0, 1]$. We have then calculated the standard deviation of the travel time, after each lens, for all streamlines in each of the 5000 realisations, relative to the mean of each individual realisation. In figure 3.1(c), we show how the standard deviation varies with the time, t, to go past each lens, $t = nL/\bar{U}$ where n is the number of lenses, illustrating that the standard deviation, σ, initially grows with a power law $t^{1/2}$ but then changes to increase as t. This change in behaviour is analogous to the results presented in chapter 2, and we now show that owing to the lenses, the flow again develops a mean shear along the channel.

To demonstrate the importance of the shear, we examine the migration of a pulse of tracer through a vertically confined channel, in which there is a dilute and random distribution lenses of different permeability (cf. Cala and

Greenkorn (1986), Dagan et al. (2003)). In §3.2, we consider flow through a permeable layer which contains a series of elliptically shaped lenses of length $l = H$ and $h = 0.2H$, where H is the channel width, and whose centres are distributed randomly across the layer. Again we demonstrate that the presence of impermeable boundaries leads to development of a shear in the mean flow. In §3.3, we show that once the flow has passed through $n \geq 4$ lenses the spreading of the tracer may be modelled in terms of a spatially averaged longitudinal flow, $U(z)$, combined with a Fickian dispersion coefficient, $D(z)$, associated with the random positioning of the lenses. Using this continuum model we demonstrate that a pulse of tracer released into the flow undergoes a transition from Fickian spreading at early times to shear-driven spreading at late times consistent with our numerical simulations. We also demonstrate that as the size of the pulse of tracer relative to the width of the channel decreases, the time of transition from Fickian spreading to shear-driven spreading increases. In §3.4, we consider the implications of these new results to the dispersion of the flow in a heterogeneous geological formation. We demonstrate that the initial cross-flow length-scale of a pulse of tracer, and its position relative to the upper and lower boundaries of the flow domain, have an important impact on the mean speed and the dispersal of the tracer by the flow in our model heterogeneous porous layers. Therefore quantifying this shear is key to building upscaled models for pollutant dispersal in groundwater flows, radioactive waste disposal, and the dispersion of contaminants in other porous flows.

3.2 Development of shear flow in a bounded domain

We focus on the flow through elliptical lenses of permeability k_2 embedded in a domain of background permeability k_1. Each elliptic region has length l in the along-flow direction and width h in the cross-flow direction, where $l/H \sim \mathcal{O}(1)$ and $h/H \sim \mathcal{O}(0.01 - 1)$. We use numerical simulations to solve for the travel times along individual streamlines (see appendix A).

3.2.1 Travel times with a single lens in the channel

In order to model the flow through an assemblage of elliptical lenses, we begin by considering the flow past a single lens in order to estimate the travel times

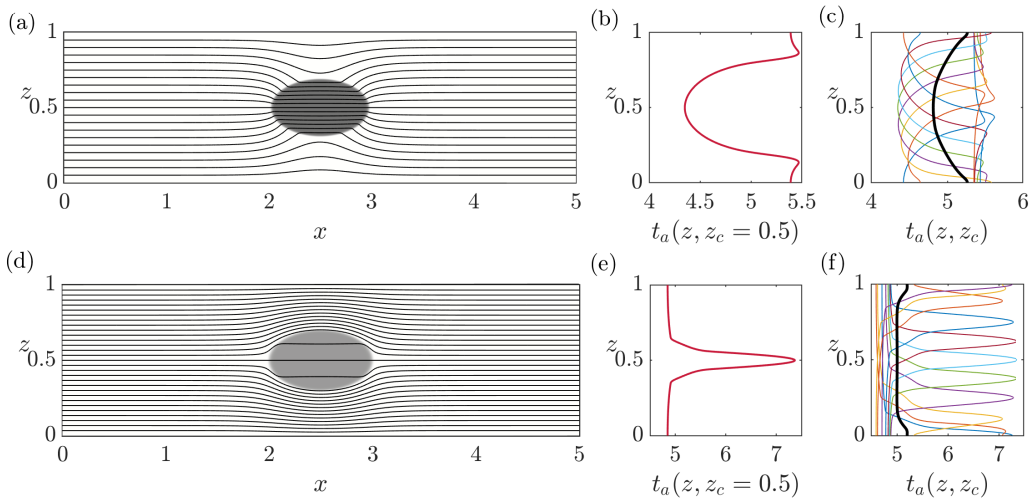

Figure 3.2 Panels (a)-(c) correspond to the calculations for a high permeability lens with $k_2/k_1 = 4$ and $h/H = 0.4$, and panels (d)-(f) correspond to a low permeability lens with $k_2/k_1 = 1/4$ and $h/H = 0.4$. Panels (a) and (d) show the streamlines illustrating the distortion of flow through the high permeability lens and through the low permeability lens respectively. Panel (b) and (e) show the corresponding tracer arrival times, $t_a(z, z_c)$, at $x = 5$ for a pulse of passive tracer released instantaneously into the flow at $x = 0$, $t = 0$, corresponding to the lens shown in (a) and (d) respectively. Panels (c) and (f) show the tracer arrival times, $t_a(z, z_c)$, as a function of the vertical location, z, in the channel. The different curves represent the arrival times for different vertical locations, z_c, of the lens in the channel. The black line represents the mean travel time, $t_m(z)$, obtained by averaging $N = 81$ curves for the high and low permeability lenses respectively.

along individual streamlines. Figures 3.2(a),(d) show typical examples of the streamlines for flow through a single lens placed in a channel with its centre at $(x_c, z_c) = (2.5, 0.5)$, with permeability ratio $k_2/k_1 = 4$ and $k_2/k_1 = 1/4$ respectively. We calculate the travel times, $t_a(z, z_c)$, along different streamlines from a location $x = x_c - L/2$ upstream of the lens to $x = x_c + L/2$ downstream of the lens by integrating along each streamline (see appendix A). This is shown in figures 3.2(b),(e) for $L = 5$, corresponding to the lenses in figures 3.2(a),(d).

For a lens of given permeability and aspect ratio, the travel times, $t_a(z, z_c)$, depend on the vertical location, z_c, of lens in the channel. Figures 3.2(c),(f) show the vertical distribution of arrival times for 9 locations of the lens across the channel, given by $z_c = 0, 0.125, 0.25, 0.375, 0.5, 0.625, 0.75, 0.875, 1$. For any N discrete values of z_c between $z = 0$ and $z = 1$, we can estimate a mean travel time, $t_m(z)$, and a variance of travel time, $\sigma_t^2(z)$, at each height, z. These are given by

$$t_m(z) = \frac{1}{N} \sum_{z_c=0}^{1} t_a(z, z_c), \tag{3.1a}$$

$$\sigma_t^2(z) = \frac{1}{N} \sum_{z_c=0}^{1} (t_a(z, z_c) - t_m(z))^2. \tag{3.1b}$$

Given the travel times along individual streamlines, we now provide a framework to model the flow through an assemblage of lenses assuming that the lenses are randomly distributed in the cross-flow direction and that they are sufficiently far apart horizontally so that their flow fields are decorrelated.

3.2.2 Flow through an assemblage of lenses

In the case of long and thin lenses, on entering or leaving the lens, the flow adjusts rapidly over a short distance compared to the length of the lens. For lenses of length comparable to the width of the domain, the lateral extent over which the flow is influenced by the lens may be several multiples of the lens dimension. Figures 3.2(a),(d) show that as the flow approaches and then passes through a lens, the streamlines become distorted as fluid is diverted into the lens, and downstream of the lens the flow then gradually returns to a uniform flow. We define the zone of influence of the lens, L_{cr}, to be the horizontal

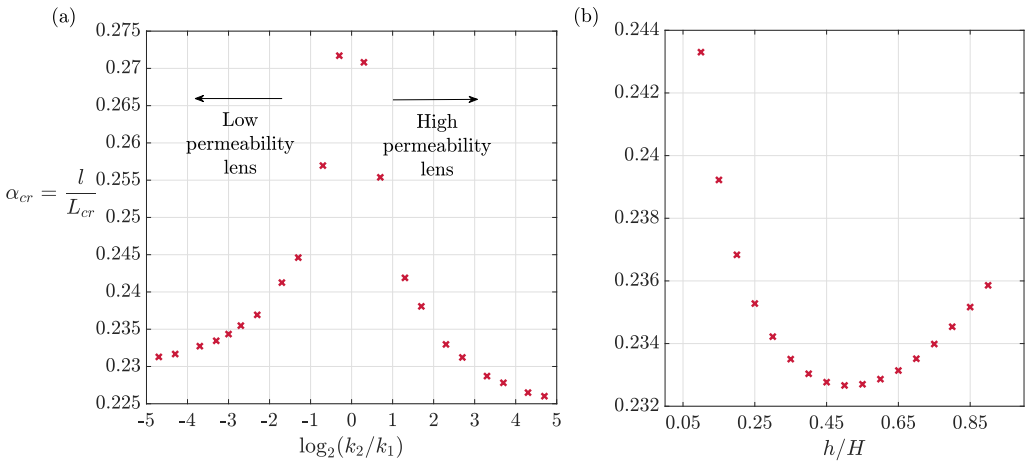

Figure 3.3 $\alpha_{cr} = l/L_{cr}$ plotted as a function of (a) the ratio of the permeability of the lens to the background permeability, k_2/k_1, and (b) the ratio of the width of the lens to the channel width, h/H. In (a), $h/H = 0.4$, and in (b), $k_2/k_1 = 8$.

distance such that for $x_c - L_{cr}/2 < x < x_c + L_{cr}/2$, the horizontal velocity, $u(x, z)$, across the channel deviates by more than 0.001% of the uniform far-field flow.

Figure 3.3 shows the variation of $\alpha_{cr} = l/L_{cr}$ with the width ratio, h/H, and the permeability ratio, k_2/k_1. As seen from figure 3.3(a), the vertical extent of the lens, h, has a significant effect on the value of L_{cr} since the domain is bounded in the cross-flow direction. The coefficient, $\alpha_{cr} = l/L_{cr}$, provides an approximation for the horizontal distance between successive lenses in a channel so that the flow fields associated with individual lenses can be assumed to be independent. In the following analysis, to illustrate the effects, we consider the case in which the lenses are dilute, so that the flow fields do not interact ($L \geq L_{cr}$).

We consider the flow through an assemblage of n lenses in the channel where the locations of the centres of the successive lenses $i = 1, ..., n$ are given by $x_c(i) = (2i - 1)L/2$, where L is the horizontal distance between successive lenses, and $z_c(i)$ is randomly chosen from the N positions across the channel given by $z = 0, 1/(N - 1), 2/(N - 1), ..., 1$. In all calculations presented in this chapter we choose $N = 81$ positions of the lens across the channel, but the results are not sensitive to this precise value for $N \geq 81$. Based on figure 3.3, we choose a dilution coefficient $\alpha = l/L \approx 0.2 < \alpha_{cr}$ so that lenses are in the dilute limit ($l = 1,\ L = 5$).

3.2.3 Continuum model for the flow through an assemblage of lenses

Recall that the mean travel time and travel time variance estimated using equation (3.1) vary with the vertical location, z, in the channel. As described in the previous chapter, we therefore expect that the concentration of a passive tracer released into the flow can be described by the mean flow, $U(z)$, and a longitudinal dispersion coefficient, $D(z)$, associated with the random positioning of the lenses within the channel. We estimate a mean flow speed, $U(z)$, and the longitudinal dispersion coefficient, $D(z)$, at each height in the channel as (cf. equation (3.1))

$$U(z) = \frac{L}{t_m(z)} \quad \text{and} \quad D(z) = \frac{1}{2}L^2\frac{\sigma_t^2(z)}{t_m^3(z)}, \tag{3.2}$$

where the equation describing the tracer concentration is given by

$$c_t + U(z)\, c_x = D(z)\, c_{xx}. \tag{3.3}$$

If a pulse of tracer of unit volume is injected instantaneously into the fluid at $t = 0$, equation (3.3) has a well-known solution,

$$c(x, z, t) = \frac{H}{2\sqrt{\pi D(z)t}} \exp\left(- \frac{(x - U(z)t)^2}{4D(z)t} \right). \tag{3.4}$$

The validity of this continuum model is demonstrated in terms of the difference between the model prediction estimated using equation (3.3) and the probability distribution of arrival times of tracer at locations $x = nL$ and at a series of vertical heights within the layer. Using the N travel times, $t_a(z, z_c)$, for each lens, i, placed at N possible vertical locations, $z_c(i)$, in the channel, we obtain a range of N^n arrival times at each vertical location, z, once the tracer has passed through an assemblage of n lenses. We use these N^n travel times to plot a residence time distribution for the tracer at different vertical locations once the tracer has passed through n lenses. This is shown by the histograms in figure 3.4. The number of bins, N_{bins}, to plot the histograms using the N^n travel times is estimated using Sturges' formula (Sturges, 1926),

$$N_{bins} = \lceil \log_2(N^n) \rceil + 1. \tag{3.5}$$

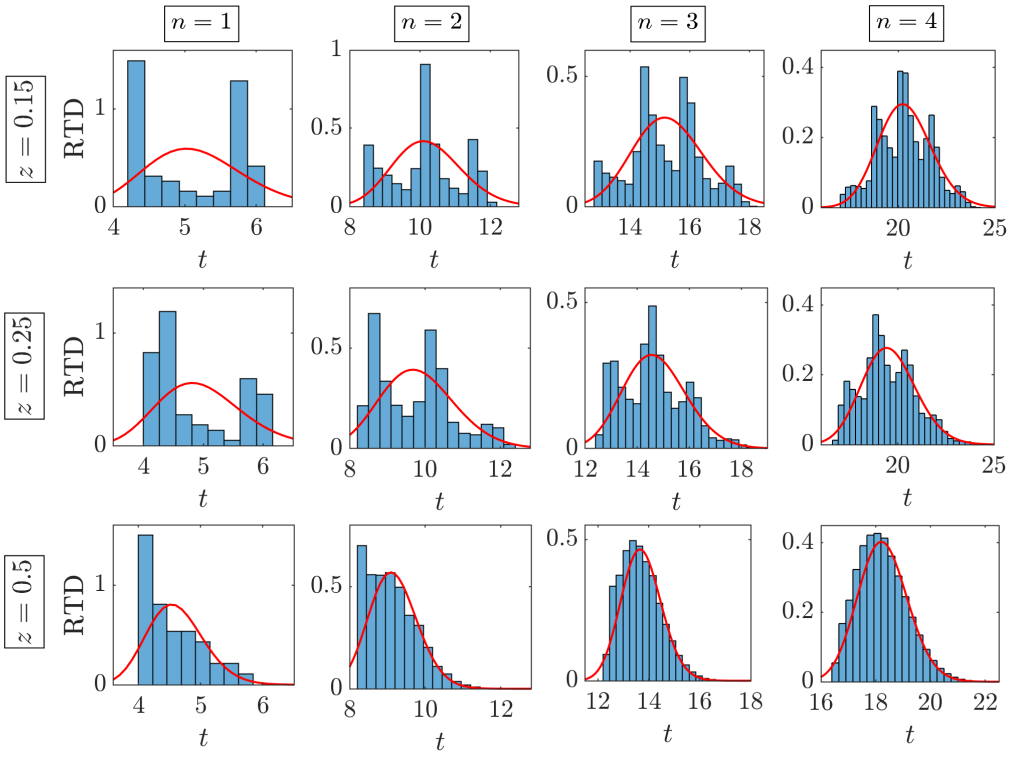

Figure 3.4 Residence time distributions (RTD) at three different vertical locations, z, in the channel and for a pulse of tracer released instantaneously into the flow at $x = 0$, $t = 0$. The arrival times are estimated at the downstream location $x = nL$ once the tracer has passed through $n = 1, 2, 3, 4$ lenses respectively and are shown here at three vertical locations, $z = 0.15, 0.25, 0.5$. The histograms are binned using Sturges' formula which uses $\lceil \log_2(N^n) \rceil + 1$ bins. The red curve is obtained using the continuum model for the flow given by equation (3.4). The permeability ratio of the lenses is $k_2/k_1 = 16$ and the width ratio is $h/H = 0.4$. In all calculations, $L = 5l = 5$.

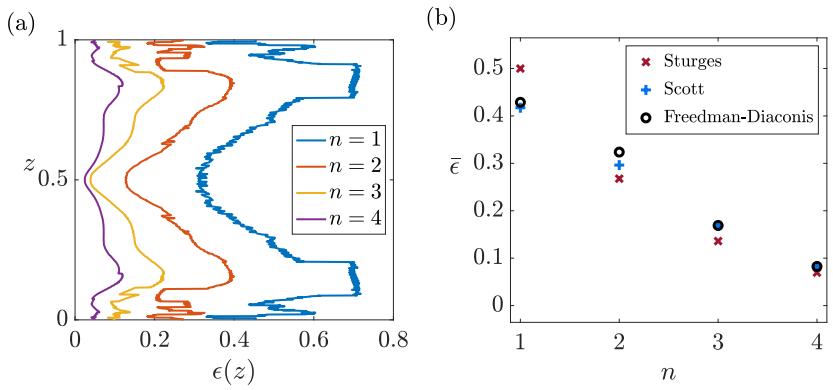

Figure 3.5 (a) The root mean squared difference between the histogram and the red curve in figure 3.4 at each vertical height, z, in the channel. The four curves (blue, red, yellow, purple) correspond to the root mean squared difference after the tracer has passed through $n = 1, 2, 3, 4$ lenses respectively. (b) Vertically averaged root mean squared difference, $\bar{\epsilon}$, as a function of the number of lenses, n, that the tracer has passed through. The symbols represent the different binning methods used to obtain the histograms (Freedman and Diaconis, 1981; Scott, 1979; Sturges, 1926). The permeability ratio of the lenses is $k_2/k_1 = 16$ and the width ratio is $h/H = 0.4$.

Figure 3.4 shows the normalised model prediction given by equation (3.4) at three different vertical heights in the layer, $z = 0.15, 0.25, 0.5$, once the tracer has passed through $n = 1, 2, 3, 4$ lenses respectively. We define a root mean squared difference, $\epsilon(z)$, between the normalised model prediction (red curves) and the probability distribution given by the histograms at each height, z, in the layer. This is shown in figure 3.5(a) once the tracer has passed through $n = 1, 2, 3, 4$ lenses. We define the vertical average of the root mean squared difference, $\bar{\epsilon}$, and find that $\bar{\epsilon} < 0.1$ once the tracer has passed through $n \geq 4$ lenses (figure 3.5(b)). This result is independent of the specific discretisation method with which we determine the probability distribution of arrival times (Freedman and Diaconis, 1981; Scott, 1979; Sturges, 1926) once the tracer has passed through $n \gg D/UL$ lenses.

Figures 3.6(a)-(f) show the profiles of mean speed, $U(z)$, and longitudinal dispersion coefficient, $D(z)$, for a range of permeability ratios and for a number of width ratios of the lens to the formation. As mentioned earlier, the cross-layer shear is maximal near the boundary, and extends a distance from the boundary which increases with the cross-layer scale of the heterogeneity.

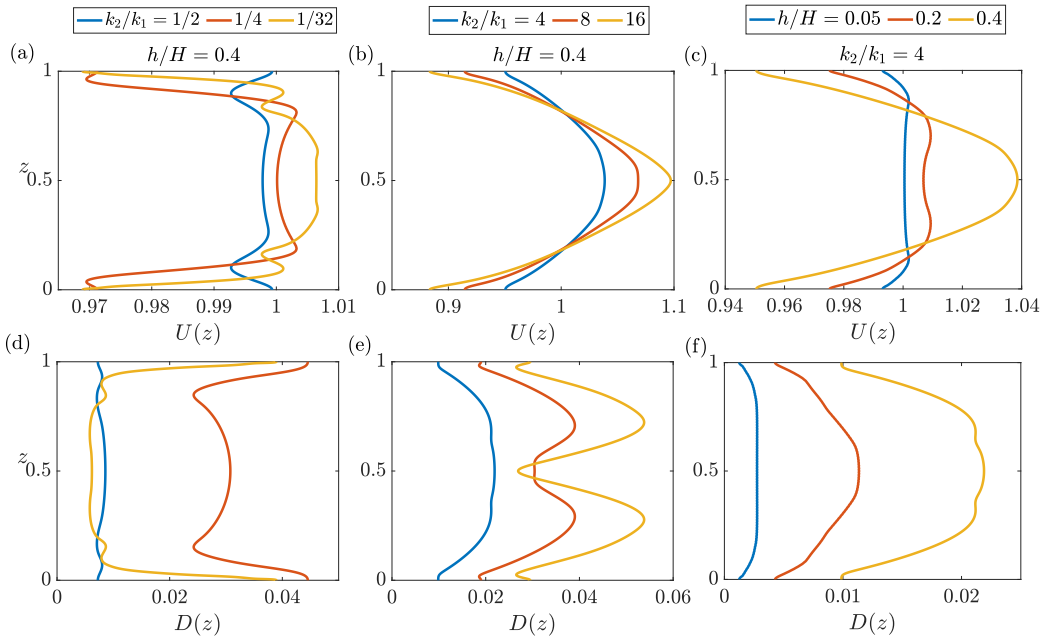

Figure 3.6 The mean speed, $U(z)$, and the longitudinal dispersion coefficient, $D(z)$, plotted for a range of values of the permeability ratio, k_2/k_1, and the width ratio, h/H, of the lens to the channel. In all calculations, $L = 5l = 5$.

3.3 Depth-averaged model for tracer transport

Figures 3.7(b)-(e) show the evolution of a pulse of tracer released into the channel at $x = 0$, $0 < z < 1$, and $t = 0$. The channel consists of lenses of permeability ratio $k_2/k_1 = 4$ and width ratio $h/H = 0.4$. The figures correspond to the concentration profile, $c(x, z, t = nL/\bar{U})$, estimated using equation (3.4) after the tracer has passed through $n = 10, 100, 1000, 10000$ lenses respectively. The white dotted line corresponds to the mean location of the tracer front, which is advection-driven with speed $U(z)$. The variance around this mean profile corresponds to the expected spreading due to the random positioning of lenses in the domain. Figures 3.7(f)-(i) show the corresponding depth-averaged profiles, $\bar{c}(x, t = nL/\bar{U})$, for the concentration profiles shown in figures 3.7(b)-(e) respectively.

Since the profiles of $U(z)$ and $D(z)$ vary smoothly across the channel, we expect that at late times the depth-averaged concentration is given by the

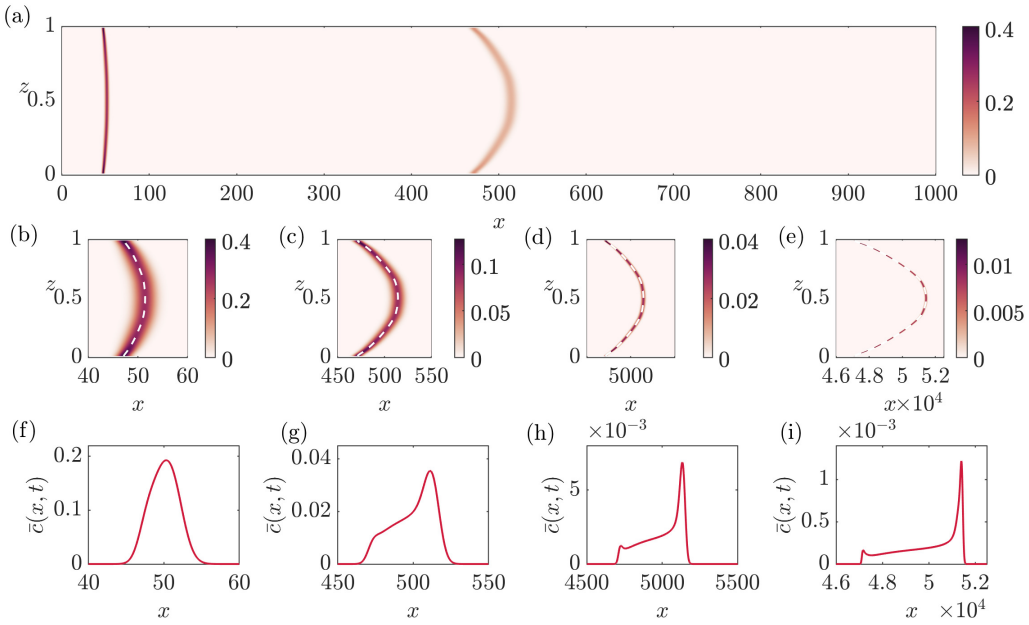

Figure 3.7 $k_2/k_1 = 4$, $h/H = 0.4$. (a) Evolution of tracer concentration at two different times after its initial release at $x = 0$, $t = 0$. In panels (b)-(e), the colours correspond to the concentration, $c(x, z, t = nL/\bar{U})$, after it has passed through $n = 10, 100, 1000, 10000$ lenses respectively, where the time taken to go through n lenses is given by $t = nL/\bar{U}$. Panels (f)-(i) show the corresponding depth-averaged profiles, $\bar{c}(x, t = nL/\bar{U})$, for the concentration profiles shown in panels (b)-(e) respectively.

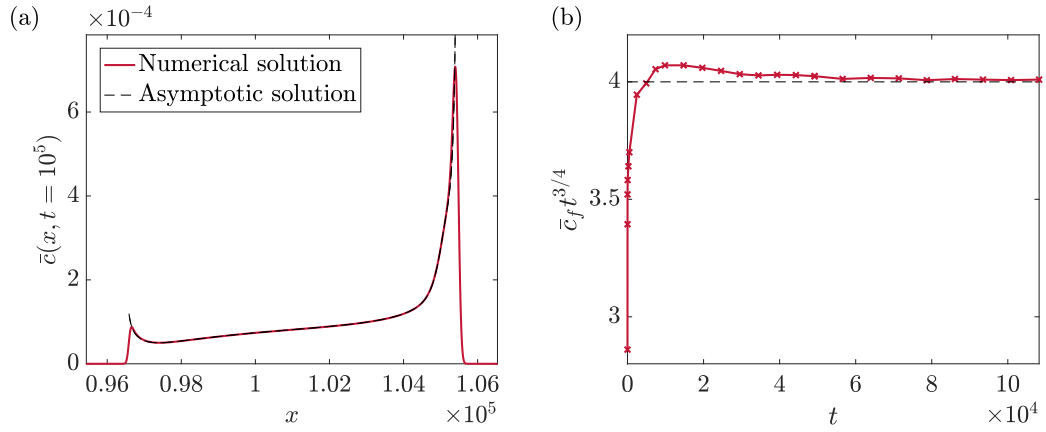

Figure 3.8 $k_2/k_1 = 4$, $h/H = 0.4$. (a) The depth-averaged tracer concentration, $\bar{c}(x,t)$, plotted at $t = 10^5$ estimated using the numerical solution (red curve) and the asymptotic solution given by equation (3.7) (black curve), illustrating the convergence to the asymptotic solution behind the leading edge. (b) The product of the maximum concentration at the leading edge, c_f, and $t^{3/4}$ plotted as a function of time, t, showing convergence to equation (3.6) at long times. The black dotted line represents $c_f t^{3/4} = \eta_o$ (cf. equation (3.6)).

asymptotic solutions described in the previous chapter for the leading edge. At $x = U(0.5)t$,

$$\bar{c}(x,t) \sim \frac{c_o H}{4\sqrt{\pi D(0.5)}} \left(\frac{16 D(0.5)}{U''^2(0.5) t^3} \right)^{1/4} \Gamma\left(\frac{1}{4}\right) = \eta_o t^{-3/4}, \tag{3.6}$$

and behind the leading edge, for $x = U(z_o)t$, the concentration follows the asymptotic solution given by

$$\bar{c}(x,t) \approx \frac{2 c_o H}{|U'(z_o)| t}. \tag{3.7}$$

Figure 3.8(a) shows the convergence of the depth-averaged profile behind the leading edge to the asymptotic solution given by equation (3.6) at long times. Figure 3.8(b) shows the convergence of the front concentration, c_f, to the asymptotic solution given by equation (3.7) at long times.

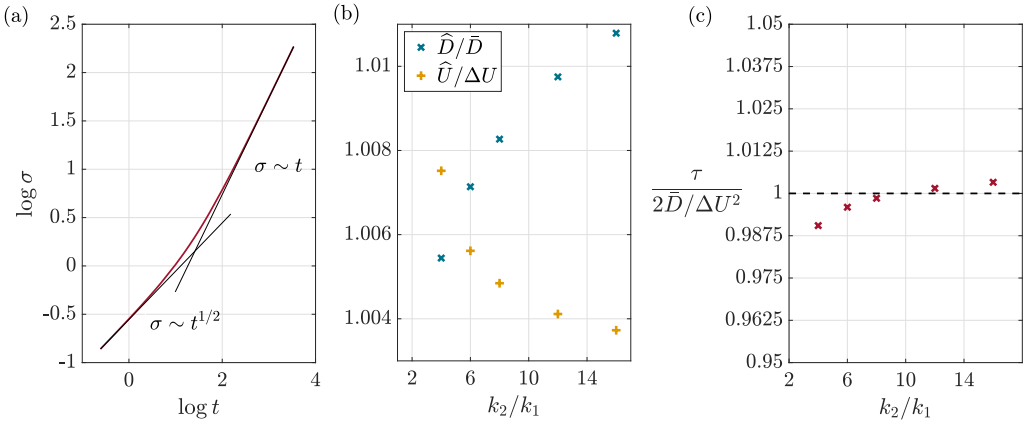

Figure 3.9 (a) The standard deviation, σ, plotted as a function of time, t, for $k_2/k_1 = 12$. (b) Variation of $\widehat{D}/\bar{D}$ and $\widehat{U}/\Delta U$ for different permeability ratios, where $\sigma = (2\widehat{D}t)^{1/2}$ and $\sigma = \widehat{U}t$ are represented by the black lines in panel (a). (c) The non-dimensional transition time, $\tau/(2\bar{D}/\Delta U^2)$, plotted as a function of the permeability ratio of the lenses for $h/H = 0.4$. The transition time, τ, is estimated numerically as the intersection between the two curves in panel (a). The black dotted line in panel (c) represents $\tau = 2\bar{D}/\Delta U^2$.

3.3.1 Transition from Fickian to shear-driven spreading of tracer

Figure 3.9(a) illustrates a typical example of how the variance of position of the tracer, σ, increases with time, t. Recall that the variance, σ, is obtained from the depth-averaged concentration profile, $\bar{c}(x,t)$, as

$$\sigma^2(t) = \frac{\int_{-\infty}^{\infty} \bar{c}(x,t)(x - x_m(t))^2 \mathrm{d}x}{\int_{-\infty}^{\infty} \bar{c}(x,t)\mathrm{d}x}, \quad \text{where} \quad x_m(t) = \frac{\int_{-\infty}^{\infty} \bar{c}(x,t)x\mathrm{d}x}{\int_{-\infty}^{\infty} \bar{c}(x,t)\mathrm{d}x}. \tag{3.8}$$

Our results show that at early times, spreading is Fickian and grows at a rate proportional $t^{1/2}$. However, at late times, the spreading of tracer is controlled by the effective mean shear and grows as t. Using the early time and late time results, we define $\widehat{D}$ and $\widehat{U}$ as given by the two curves $\sigma = (2\widehat{D}t)^{1/2}$ and $\sigma = \widehat{U}t$ (figure 3.9(a)). We also define the transition time to be given by the time at which these early time and long time solutions match, $\tau = 2\widehat{D}/\widehat{U}^2$.

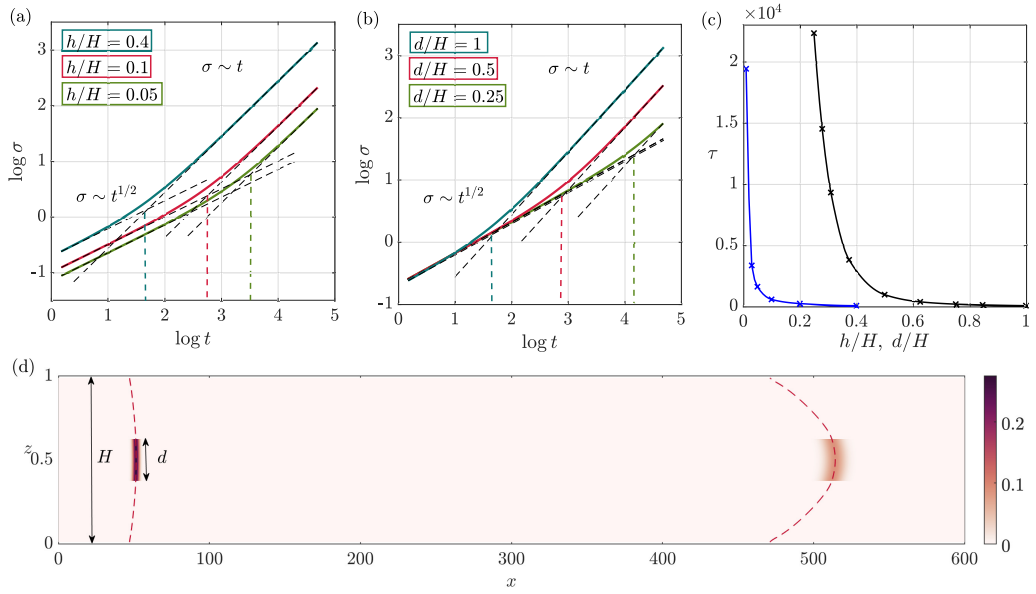

Figure 3.10 Calculations are shown here for high permeability lenses with $k_2/k_1 = 4$. In panels (a) and (b), the standard deviation, σ, is plotted as a function of time, t, for different values of the ratio of the width of the lens to the channel width, h/H, and the ratio of the vertical width of the initial pulse of tracer to the channel width, d/H. In (a), $d/H = 1$, and in (b), $h/H = 0.4$. (c) The transition time, $\tau = 2\bar{D}/\Delta U^2$, plotted as a function of h/H (blue curve) and d/H (black curve). (d) Evolution of a pulse of tracer of initial width d in a channel of width H after its initial release at $x = 0$ and $t = 0$. Here, $d/H = 0.25$. The figure illustrates how the more localised pulse of tracer only experiences a fraction of the total shear, indicated by the red dotted lines, as compared to the wider pulse of tracer shown in figure 3.7(a).

Using the properties of the mean flow and dispersion at each height in the channel, we can define the following quantities as in the previous chapter,

$$\Delta U^2 = \frac{1}{H}\int_0^H (U(z) - \bar{U})^2 \mathrm{d}z, \tag{3.9a}$$

$$\bar{U} = \frac{1}{H}\int_0^H U(z)\mathrm{d}z, \tag{3.9b}$$

$$\bar{D} = \frac{1}{H}\int_0^H D(z)\mathrm{d}z. \tag{3.9c}$$

These quantities may be used to provide an estimate for $\widehat{D}$ and $\widehat{U}$ as obtained from the numerical results (figure 3.9(a)). Indeed, figure 3.9(b) shows $\widehat{D}/\bar{D}$ and $\widehat{U}/\Delta U$ as a function of k_2/k_1, illustrating that for $1 < k_2/k_1 \leq 16$, $\widehat{D}$ and $\widehat{U}$ are within 1% of $\bar{D}$ and ΔU respectively. Figure 3.9(c) shows the non-dimensional transition time, $\tau/(2\bar{D}/\Delta U^2)$, plotted as a function of the permeability ratio of the lenses, k_2/k_1. We find that the difference between the black dotted line and the red-crosses is less than 1% for $1 < k_2/k_1 \leq 16$. Hence to leading order, the transition time may once again be described as $\tau \approx 2\bar{D}/\Delta U^2$. The monotonic trend in figure 3.9(c) is a result of the limits of our numerical calculation.

As demonstrated earlier, the shear intensity increases with the permeability ratio, k_2/k_1, and the width ratio, h/H, of the lens to formation. As the shear strength increases, the transition from dispersion to advection-driven spreading of the tracer occurs sooner, as seen in figure 3.10(a). Here, the transition time is estimated as $\tau = 2\bar{D}/\Delta U^2$. It is also relevant to observe that a localised patch of tracer of initial width $d < H$ only experiences a fraction of the velocity difference between the centre and boundary of the layer, as illustrated in figure 3.10(d) (cf. figure 3.7(a)). As a result, as d/H decreases, the transition time from dispersive spreading to shear-controlled spreading increases, as seen in figure 3.10(b), in which the variation of the standard deviation of a pulse of tracer as a function of time is shown for three different initial values of d/H.

In earlier numerical modelling studies of Janković et al. (2003), the calculations model a very small pulse of tracer initially located in the centre of the channel ($d/H \approx 0.04 - 0.06$), and hence the effect of the shear associated with the boundaries would not be seen until very far downstream, beyond the scale of the modelling. This is illustrated in figure 3.10(c), which shows a steep increase in transition time for $d/H < 0.5$ or $h/H < 0.1$. In a real system in

which tracer is injected into an aquifer from a well, then depending on the perforation distribution in the well, the tracer may initially span a significant width of the layer, so that if the size of heterogeneities is comparable the layer width, the transition to the regime of shear-driven longitudinal spreading may occur sooner than predicted by models based on the spread of very localised pulses of tracer.

3.4 Summary

In this chapter, we have analysed the dispersion of a passive tracer in a pressure-driven flow through a confined porous medium consisting of a dilute and random assemblage of elliptical lenses. We show that owing to the boundaries, a shear develops in the mean flow along the layer. This controls the late time spreading of tracer injected into the flow according to the fractional strength of the shear, $\Delta U/\bar{U}$, and the distance downstream, x, so that $\sigma \approx \frac{\Delta U x}{\bar{U}} \sim \mathcal{O}(0.01 - 0.1)x$. This is in contrast to the earlier phases of the spreading, which are controlled by Fickian dispersion associated with the heterogeneities (Dagan and Fiori, 2003; Eames and Bush, 1999), and which lead to a standard deviation which increases as $\sigma \approx \sqrt{\frac{2\bar{D}x}{\bar{U}}}$, where $\bar{D}$ is the mean dispersivity associated with the randomness of the heterogeneity. We have described the transition between these two regimes as a function of the shear and mean dispersion. We expect this transition time to be key in determining the applicability of models that describe anomalous transport of tracer in a porous formation.

Many field observations of the dispersion of tracer in porous rocks, although noisy and much more complex than our idealised model, suggest that the standard deviation of the tracer increases approximately linearly with distance downstream (Gelhar et al., 1992). For example, a linear regression on high reliability field-scale data of Gelhar et al. (1992) suggests that $\sigma \sim \mathcal{O}(0.1 - 1)x$. The development of shear in the mean flow, associated with the finite vertical extent of the layer coupled with the heterogeneities within the layer, may help in rationalising such observations. It may be that in a layered porous formation, the effect of the horizontal boundaries plays a key role in producing a mean shear within each layer and hence the linear rate of spreading of the cloud of tracer with distance downstream, as shown in the present simplified model. Although the analysis presented in this chapter is strictly only applicable for a porous medium where the lenses are in the dilute limit, in the cases where

this assumption cannot be applied, we expect the dispersion to be significantly enhanced due to the formation of preferential pathways through the channel.

Furthermore, figure 3.10(d) suggests that the initial width of the pulse of tracer controls whether the spreading is Fickian or shear-driven. If tracer is injected into an aquifer from a well, then depending on the perforation distribution in the well, the tracer may initially span a significant depth of the layer, so that if the size of heterogeneities is comparable to the layer depth, the transition to the regime of shear-driven longitudinal spreading may occur sooner than predicted by models based on the spread of very localised pulses of tracer. In the numerical calculations of Janković et al. (2006), the plumes of tracer were in fact comparable in scale to the domain width. However, the heterogeneity scale in those calculations was very small compared to the channel width ($h/H \approx 0.01$). Hence the tracer needs to travel a very long distance downstream before becoming influenced by the shear (cf. figure 3.10(a)).

Chapter 4

Shear generation in a composite layer of cross-bedded porous rock

The material contained in this chapter has been submitted for publication in the *Journal of Fluid Mechanics*, under the title 'Shear generation in composite cross-bedded porous rock' (Bhamidipati and Woods, 2020b).

4.1 Introduction

Characterising flow through heterogeneous porous rocks remains a major challenge for modelling contaminant dispersion in aquifers, the pathways followed by CO_2 during sequestration in subsurface aquifers, and the dispersion of chemicals which are injected into oil fields for enhanced recovery. In many sedimentary deposits, the sediment has bedding planes characterised by two values of permeability, parallel and normal to the direction of deposition. Owing to the time dependence of sedimentation processes, especially in fluvial and shallow marine settings, such deposits tend to be highly layered, with the direction of the bedding and of the interface between layers often being in different directions (Allen (1963), see figure 1). For example, Davis et al. (1993) found that in the Sierra Ladrones formation, there were laterally extensive layers, over 100 m long but only 1-2 m deep, composed of a series of cross-bedded rock elements, with different orientations and anisotropy. Developing upscaled models for the flow through such formations is challenging (Dagan, 1979); there

are models to predict the effective permeability of such formations (Goggin et al., 1988; Tidwell and Wilson, 2000) and in reservoir simulation, models often use effective vertical and horizontal permeabilities (Begg and King, 1985; Durlofsky, 1991; Nordahl and Ringrose, 2008; Pickup et al., 1995).

In a vertically confined but laterally extensive layer of cross-bedded rock, with permeability k_1 and k_2 in the directions θ_i and $\pi/2 - \theta_i$ relative to the boundaries, the effective permeability parallel to the boundaries is (figure 4.1(c))

$$\bar{k} = \frac{k_1 k_2}{k_1 \sin^2\theta_i + k_2 \cos^2\theta_i}. \tag{4.1}$$

In order to maintain a flow parallel to the boundaries, there needs to be a pressure gradient in both vertical and horizontal directions. The net direction of this pressure gradient relative to the boundaries, θ_p, is given by (cf. Woods (2015))

$$\theta_p = \tan^{-1}\left(\frac{p_z}{p_x}\right) \quad \text{where} \quad \frac{p_z}{p_x} = \frac{(k_2/k_1 - 1)\sin\theta_i \cos\theta_i}{\sin^2\theta_i + (k_2/k_1)\cos^2\theta_i}. \tag{4.2}$$

This angle of deviation of the pressure gradient is shown in figures 4.1(d)-(e) as a function of the permeability ratio, k_2/k_1, and the direction of the bedding planes relative to the boundary, θ_i. It is seen the pressure gradient is tilted towards the direction of lower permeability, and that this tilt depends on the inclination of the bedding and increases with the permeability ratio of this bedding, k_2/k_1.

In a typical flow channel within a formation, there may be several elements of rock with different orientation or magnitude of the cross-bedding, and with inclined boundaries relative to the flow direction (figure 4.1(a)). The change in the direction and magnitude of the pressure gradient in moving from one element to another can lead to significant distortion of the streamlines, as observed in some laboratory experiments reported by Klise et al. (2008). However, although there has been some stochastic modelling of the role of the interfaces on the distortion of streamlines by using a model with different correlation lengths in the vertical and horizontal directions (Corbett and Jensen, 1992; Desbarats, 1989; Deutsch, 1989), there is incomplete understanding of the basic controls on the dispersion of tracer moving through such a formation.

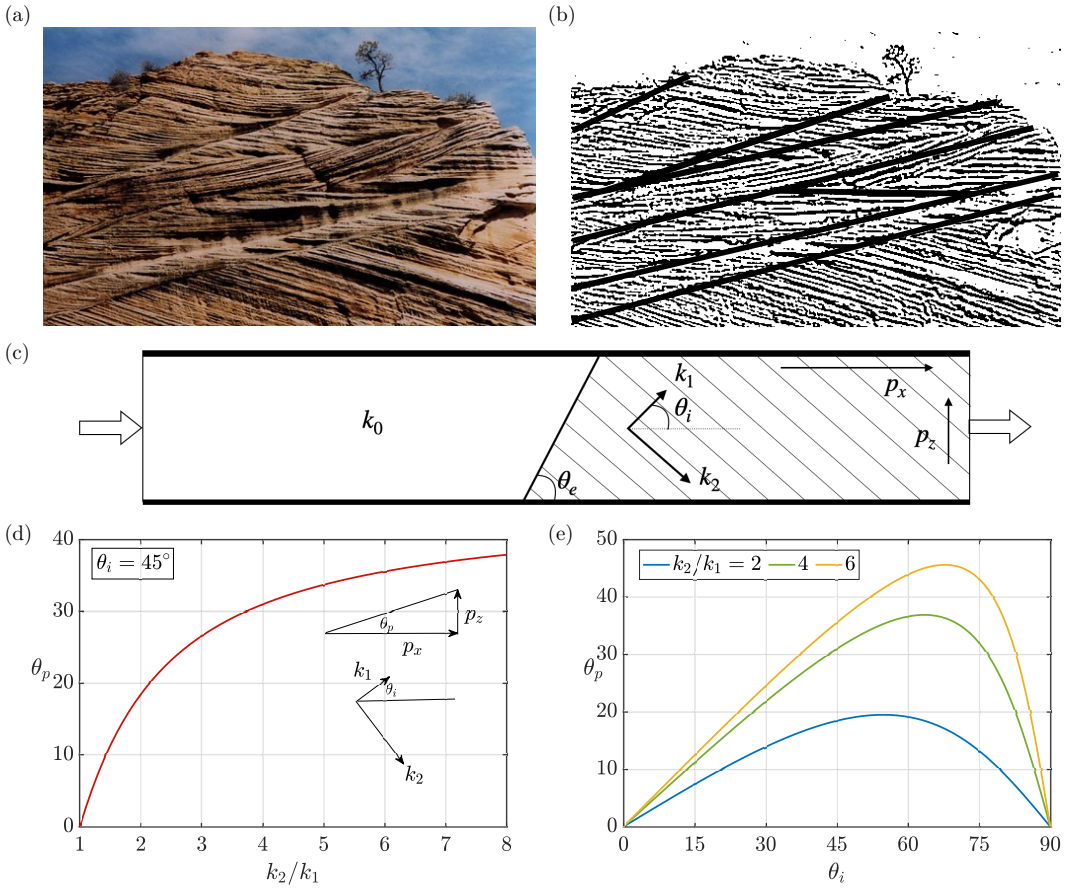

Figure 4.1 (a) Cross-bedding in Navajo Sandstone near Lake Powell, Arizona, USA. (b) The corresponding digitised image of the photograph shown in panel (a), where the boundaries between coherent cross-bedded zones are identified by the thick black lines. (c) A schematic of the model setup in our idealised problem. Within the cross-bedded layer to the right of the interface, the permeability is k_2 and k_1, along and across the bedding, and the bedding planes are inclined at an angle θ_i to the lateral boundaries. The interface between the two individual zones of rock is tilted at an angle θ_e to the lateral impermeable boundaries. The interface at $z = 0.5$ is centred at $x = x_c$. (d)-(e) The variation of the direction of the downstream pressure gradient, θ_p which is required to maintain flow parallel to the boundaries, as a function of (d) the permeability ratio, k_2/k_1, and (e) the angle of the bedding planes, θ_i (equation (4.2)).

In this chapter we explore the structure of the cross-layer shear which develops in a confined channel as a result of the distortion of the flow when passing (i) through an inclined interface between two isotropic elements of rock of different permeability (§4.2); and (ii) from an isotropic to an anisotropic element of rock, with a vertical boundary between the two layers (§4.3). We then combine these results, to provide new understanding of the shear flow which typically develops in such composite layers (§4.4 and §4.5). Recognition of this cross-layer shear is key for prediction of pollutant dispersal and for modelling the dispersion of a pulse of chemical treatment fluid often injected into such reservoirs.

To illustrate the different flow patterns and predict the shear, we use numerical solutions based on flow in a long thin channel, as shown in figure 4.1(c), where the permeability gradually changes from $K_1 = k_0$ and $K_2 = k_0$ in the isotropic layer and $K_1 = k_1$ and $K_2 = k_2$ in the cross-bedded layer (see appendix A).

4.2 Shear generation across a tilted interface in a confined channel

If the interface between two isotropic layers of different permeability, which are confined between two impermeable parallel boundaries, is tilted relative to the boundaries, then a transition zone develops across which the pressure gradient adjusts from the upstream to the downstream value. In figures 4.2(a)-(d) this may be seen both in terms of the distortion to the streamlines (thin black curves), the distortion to the surfaces of constant pressure near the interface (thin coloured lines), and also the motion of a streak of dye (thick line). The interface is shown with a thick black line; a similar graphical scheme is used for all subsequent plots illustrating the flow in this chapter.

In panels (a)-(b), the region to the right of the interface has the higher permeability, $\bar{k} = 4k_0$. Streamlines at the base of the channel therefore reach the higher permeability zone sooner, and so have a shorter travel time through the domain. In turn, the streaks of dye released into the flow upstream, as shown by the (a) blue and (b) orange lines, become sheared out towards the base of the layer. In figures 4.2(c)-(d), the region to the right has a lower permeability, and so along the streamlines at the base of the channel, the flow

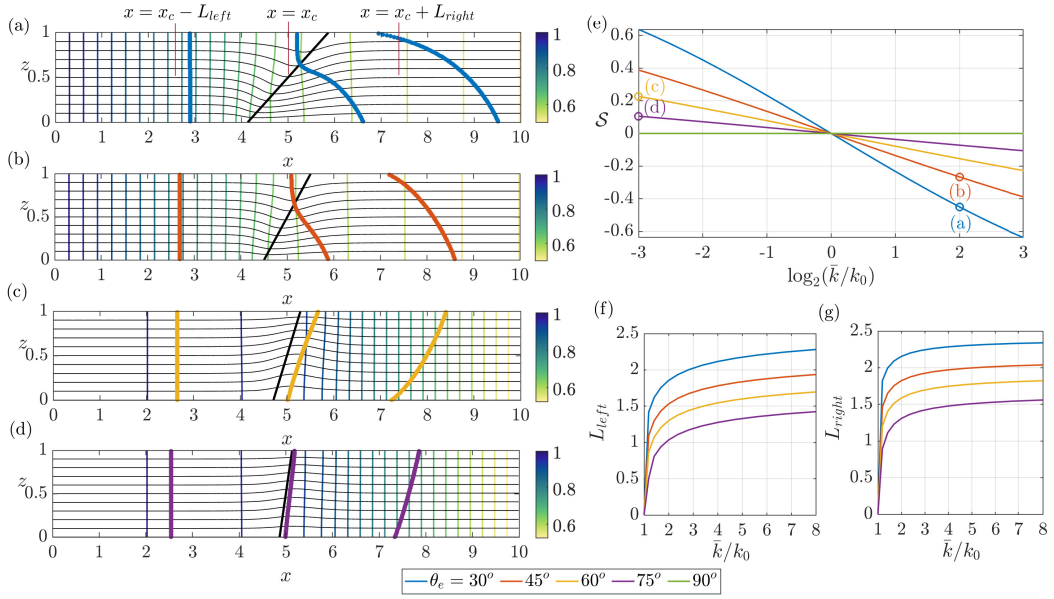

Figure 4.2 (a)-(d) The thick black line shows the interface between two isotropic zones of rock with permeability k_0 to the left and $\bar{k}$ to the right. The thin coloured lines indicate contours of constant pressure, $p(x, z)$, and the thin black curves show the streamlines of the flow. The thick coloured lines show the location of a line of tracer at three times after the initial release at $x = 0$ and $t = 0$ (in blue, orange, yellow and purple respectively). In panels (a) and (b), $\bar{k} = 4,\ k_0 = 1$. In panels (c) and (d), $\bar{k} = 1/8,\ k_0 = 1$. (e) The shear strength, $\mathcal{S}$, is shown as a function of the permeability ratio, $\bar{k}/k_0$, with the results for panels (a)-(d) labelled on this figure. In panels (f) and (g), the transition distances from uniform flow upstream of the interface, L_{left}, to uniform flow downstream of the interface, L_{right}, are shown as a function of the permeability ratio, $\bar{k}/k_0$ (see panel (a)). In all panels, the colours correspond to the angle of the interface between the two regions, θ_e, as indicated at the bottom of the figure.

slows down on passing through the interface. Thus the streak of dye at the base of the layer lags that higher in the formation, leading to a shear in the opposite sense to panels (a) and (b).

The strength of the shear generated in the transition zone depends on the permeability contrast and the angle of inclination of the interface. To quantify this shear, we first define the transition zone as being the region $x_c - L_{left} < x < x_c + L_{right}$, in which the horizontal velocity, $u(x, z)$, at some point across the channel deviates by more than 0.5% of the uniform far-field flow (see figure 4.2(a)), where x_c is at the centre of the interface. Figures 4.2(f)-(g) show the variation of the size of the transition zone as a function of the permeability ratio between the two regions, $\bar{k}/k_0$, for a range of angles of inclination of the interface. We then estimate the travel times, $t_a(z)$, along individual streamlines at each height z in the layer by integrating along each streamline in the region, $(x_c - L/2) < x < (x_c + L/2)$, where the interface is centred at along-channel position $x = x_c$ and where $(L > 2\max(L_{left},\ L_{right}))$. We repeat similar calculations for all permeability ratios and interface angles considered in this chapter. Note also that in all our calculations, we integrate over a region of length $L = 5$ since this always exceeds the length of the transition zone for the choice of parameters shown in this chapter.

We can define a dimensionless shear strength, $\mathcal{S}$, as

$$\mathcal{S} = \frac{U(z=H) - U(z=0)}{\bar{U}}, \quad \text{where} \quad U(z) = \frac{L}{t_a(z)} \quad \text{and} \quad \bar{U} = \frac{1}{H}\int_0^H U(z). \tag{4.3}$$

Figure 4.2(e) shows this shear strength as a function of the permeability contrast across the interface for interfaces with angles of tilt $\theta_e = 30°,\ 45°,\ 60°,\ 75°$ and 90°. Note that the shear has the same size but changes sign under the mapping $k_1/k_2 \to k_2/k_1$.

4.3 Shear production at a vertical interface with an anisotropic layer

When the region downstream of the interface is cross-bedded, the pressure gradient associated with the uniform flow downstream is directed at an angle to the boundaries, as seen by the contours of constant pressure in figures 4.3(a)-(c)

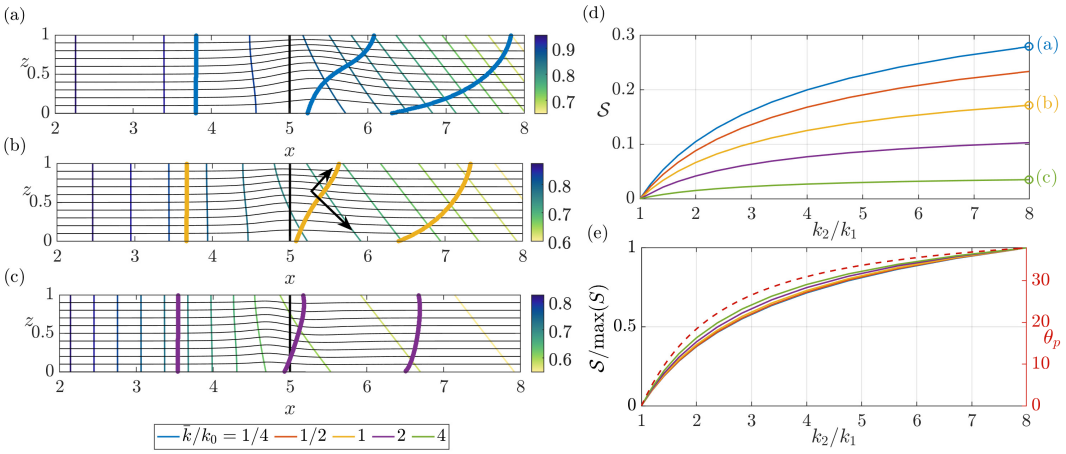

Figure 4.3 (a)-(c) Streamlines (thin black curves), pressure contours (thin coloured lines) and tracer location (in thick blue, yellow and green lines respectively) at three times after the initial release, for the flow through a porous layer in which the region $x < 5$ is isotropic with permeability $k_0 = 1$, and the region $x > 5$ is cross-bedded with the permeability ratio across and along the layers, $k_2/k_1 = 8$. In these calculations, $\theta_i = 45°$ as indicated by the black arrows in panel (b). (d) Variation of the shear strength, $\mathcal{S}$, as a function of k_2/k_1, for five values of the effective along-layer permeability of the cross-bedded zone, $\bar{k}/k_0$. (e) The normalised shear strength, $\mathcal{S}/\max(\mathcal{S})$ (solid lines), and the direction of the downstream pressure gradient in the cross-bedded region (dotted line, cf. figure 4.1(d)), as a function of the permeability ratio, k_2/k_1.

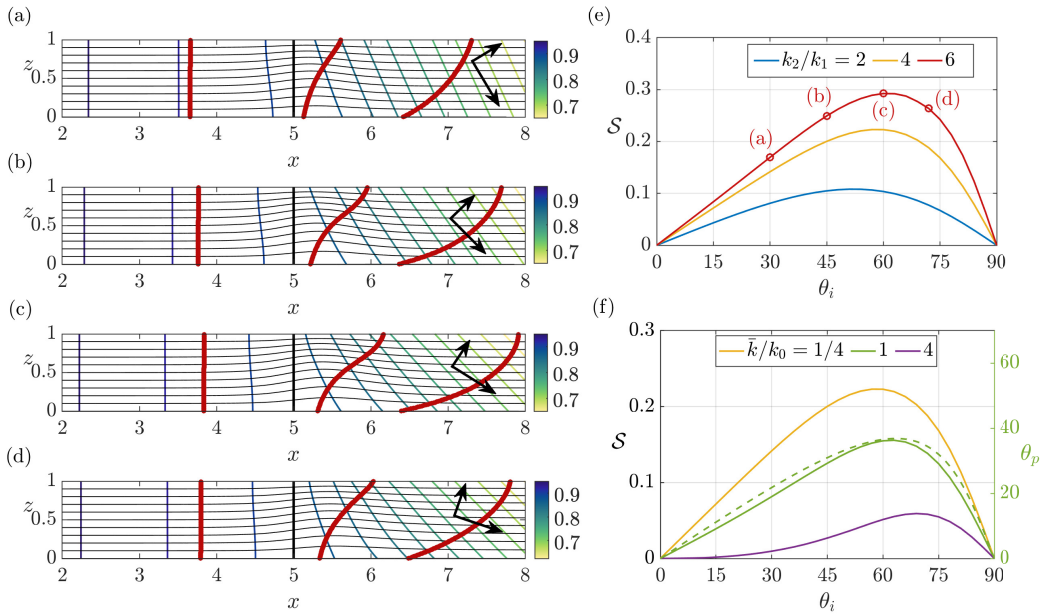

Figure 4.4 (a)-(d) Streamlines (thin black curves), pressure contours (thin coloured lines) and tracer locations (thick red lines) at three times after the initial release at $x = 2$ and $t = 0$ into a porous layer with isotropic permeability for $x < 5$ and which is cross-bedded for $x > 5$, with the ratio of permeability along and across the beds $k_2/k_1 = 6$. The cross-bedding is oriented at angles $\theta_i = 30°$ (a), $45°$ (b), $60°$ (c) and $72°$ (d), as indicated by the thick arrows on each panel. (e)-(f) Variation of the shear strength, $\mathcal{S}$, as a function of the angle of cross-bedding, θ_i, for different values of (e) k_2/k_1, with $\bar{k}/k_0 = 1/4$, and (f) $\bar{k}/k_0$ with $k_2/k_1 = 4$. The flow realisations in panels (a)-(d) are shown in panel (e). The dotted line in panel (f) corresponds to the direction of the downstream pressure gradient in the cross-bedded region (cf. figure 4.1(e)) for $k_2/k_1 = 4$ and $\bar{k}/k_0 = 1$.

(cf. figure 4.1(d)-(e)). The pressure gradient tilts towards the direction of the lower permeability in the cross-bedded zone, as shown by the shorter black arrow in panel (b). This leads to a weakening of the pressure gradient at the base of the interface which results in the development of a net shear in the transport of the tracer (blue, yellow and green lines) across the interface zone since the flow is weaker near the base than at the top of the zone. The calculations in figures 4.3(a)-(c) correspond to a bedding angle of 45° and a permeability contrast within the cross-bedded layer of 1:8.

Figures 4.3(a)-(c) illustrate the dependence of the shear on the effective horizontal permeability change across the interface. With a decrease in effective along-layer permeability from 1 to 0.25 (panel (a)), the pressure gradient becomes larger downstream and this amplifies the difference in the speed between the top and the base of the layer near the interface, as may be seen by the deformation of the streamlines. As a result a significant shear develops. When the effective permeability downstream equals that upstream (panel (b)), a significant shear still develops owing to the change in direction of the pressure gradient, although the shear is weaker. When the effective along-layer permeability is 4 times larger than that upstream (panel (c)), the pressure gradient becomes weaker downstream of the interface and this reduces the difference in the flow speed between the top and base of the interface, as may be seen by the much smaller deformation of the streamlines, thereby leading to a much smaller shearing of the tracer as it passes through the interface.

In figure 4.3(d) we illustrate the change in the magnitude of the shear as the permeability contrast in the cross-bedded layer, k_2/k_1, changes. These calculations were made while keeping the mean permeability constant in the cross-bedded region; the closer the internal permeability ratio of the cross-bedded region, k_2/k_1, is to unity, the smaller the shear (cf. figure 4.1(d)). On rescaling, the curves in panel (d) appear to collapse (panel (e)), and the trend follows the increase in magnitude of the direction of the pressure gradient relative to the boundary, θ_p, as k_2/k_1 increases, as shown by the dashed line (cf. figure 4.1(d)). .

The above calculations focus on the case that the cross-bedded region has bedding plane of 45°. If the orientation of the bedding planes change, then the direction of the downstream pressure gradient will also change (figures 4.1(e)) and in turn this will impact the shear. In figures 4.4(a)-(d), we illustrate the change in the shear, as illustrated by the distortion of the line of tracer on

passing through an interface into a cross-bedded region, when the orientation of the bedding planes changes from 30° to 72°. The black arrows show the direction of the permeability in each case. Figure 4.4(d) illustrates the variation of the shear with angle θ_i for three values of k_2/k_1; the red curve corresponds to panels (a)-(d). As the permeability ratio, k_2/k_1, decreases towards unity (yellow and blue lines) with an effective permeability of the downstream layer, $\bar{k} = k_0/4$, the shear also decreases. For a given permeability ratio in the cross-bedded region, k_2/k_1, then as the direction of the bedding plane θ_i changes, the magnitude of the shear follows the magnitude of the direction of the pressure gradient relative to the boundaries, θ_p, as may be seen by comparing the solid and dashed green lines in figure 4.4(f) (cf. figure 4.1(e)). This figure also illustrates that the magnitude of the shear increases as the effective permeability of the cross-bedded region in the along-layer direction becomes smaller.

4.4 Shear generation in anisotropic layers with a tilted interface

We now explore the interaction between the two different mechanisms of generating shear: shear production at an inclined interface between two zones of different permeability (§4.2) and shear production at an interface between an isotropic and a cross-bedded layer (§4.3). In figure 4.5, we illustrate the change in flow pattern as the tilt of the interface at a boundary between an isotropic and a cross-bedded layer is changed, and figure 4.6 illustrates the corresponding shear strength, for three values of the effective permeability in the cross-bedded layer relative to the isotropic layer.

For reference, in figure 4.5, the central row of panels, with a vertical interface as indicated by the solid black line, illustrates the difference between an anisotropic layer with a small effective permeability (left) and with a high effective permeability (right). In the low permeability case, tilting the interface in the direction of the pressure gradient (upper two panels, left-hand side) increases the shear since the effect of the tilted interface combines with the effect of the anisotropy. Tilting the interface in the opposite sense leads to a reduction in the shear and eventually a reversal as the tilt dominates the effect of the cross-bedding (lower left-hand panels). In contrast, with a more permeable cross-bedded layer, the shear is quite small when the interface is

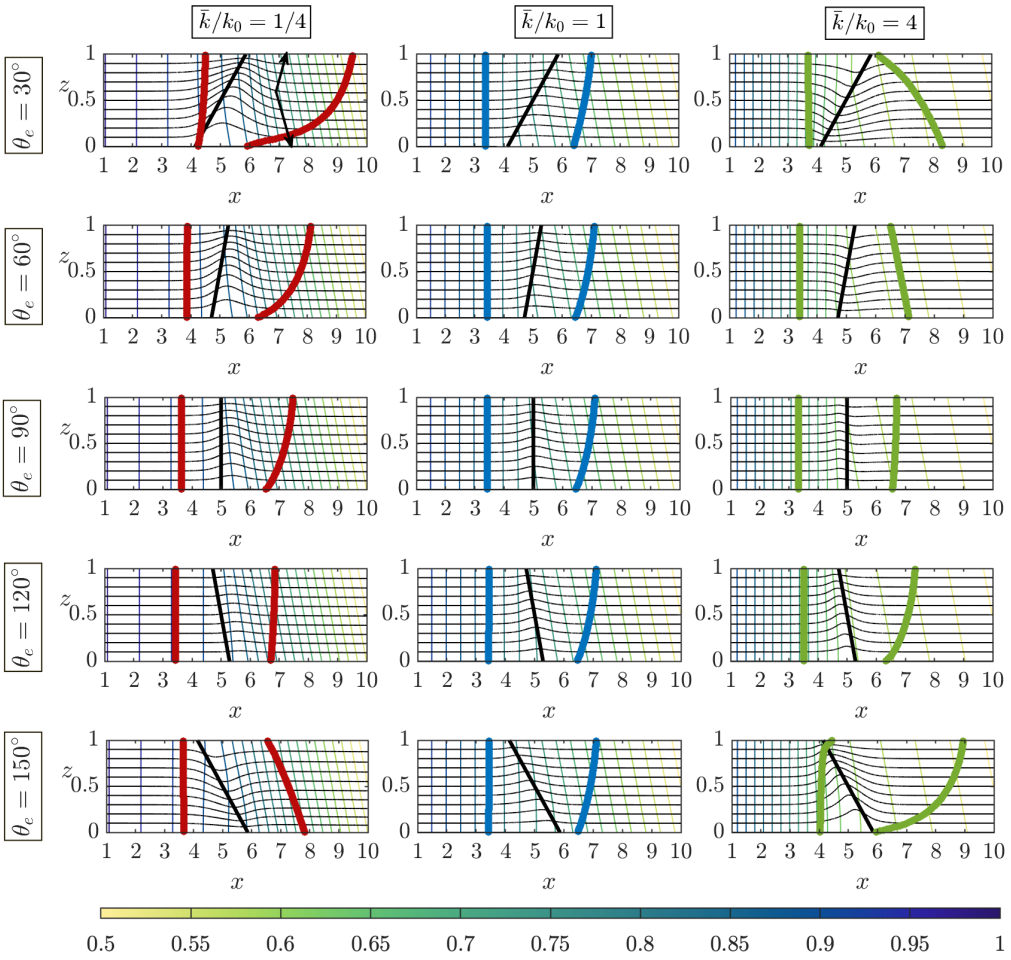

Figure 4.5 Streamlines are shown with the thin black curves, pressure contours with the thin coloured lines, the location of line of tracer at two times is shown with a thick coloured line. In all calculations, the region to the left of the interface, indicated with a solid black line, is isotropic with permeability k_0 and the region to the right is cross-bedded with the bedding permeability ratio $k_2/k_1 = 4$ and angle of bedding $\theta_i = 45°$ as indicated by the arrows in the top left panel. Each row and column corresponds to a different value of mean permeability, $\bar{k}/k_0$, for the cross-bedded region, and a different angle of the interface, θ_e, as indicated.

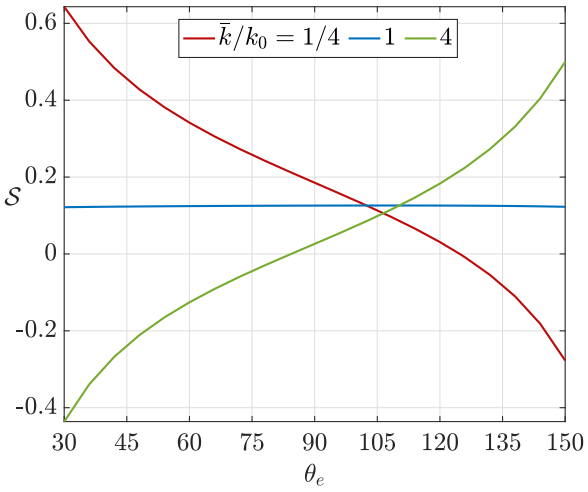

Figure 4.6 The shear strength, $\mathcal{S}$, is shown as a function of the angle of the interface, θ_e. The different curves correspond to $\bar{k}/k_0 = 1/4,\ 1,\ 4$. The streamlines and pressure contours along each curve are shown in figure 4.5 with the same colour scheme in both figures.

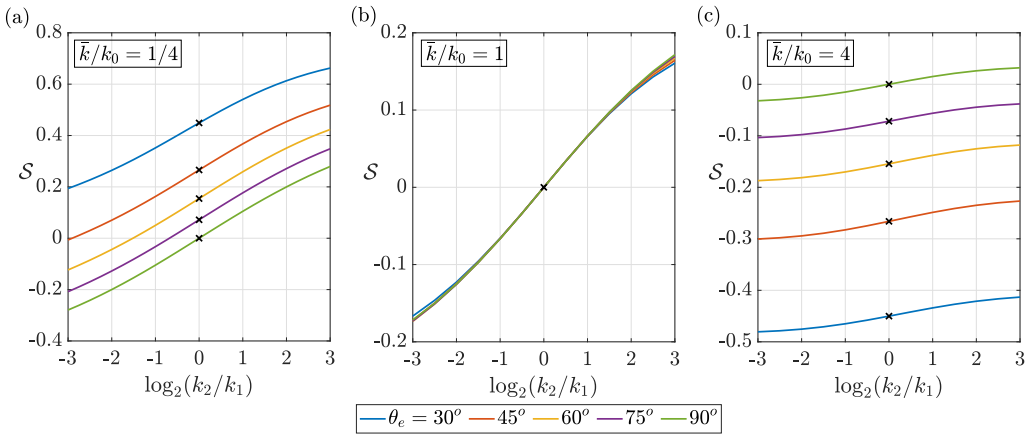

Figure 4.7 The shear strength, $\mathcal{S}$, is shown as a function of the strength of the permeability ratio across the cross-bedding, k_2/k_1, with $\bar{k}/k_0 = 1/4$ (a), 1 (b) and 4 (c). The colours correspond to the angle of the interface with the isotropic layer upstream, $\theta_e = 30°,\ 45°,\ 60°,\ 75°$ and $90°$. In all calculations, $\theta_i = 45°$. The black crosses indicate isotropic blocks with $k_2 = k_1$.

vertical (middle right-hand panel; cf. figure 4.3). Since the pressure gradient is weaker downstream, then tilting the interface causes the direction of the pressure gradient to tilt in the opposite sense as the tilt of the interface. If tilt of the interface is in the same sense as the direction of the pressure gradient downstream, then the interface counteracts the effect of the cross-bedding (top right-hand panels), and eventually can lead to an overall reversal of the sense of the shear. If the interface tilt is opposite to the direction of the pressure gradient in the cross-bedded layer (lower right-hand panels), the effect of the tilt now combines with the cross-bedding to enhance the shear. The middle column of panels in figure 4.5 shows that if the effective permeability in the downstream cross-bedded element, $\bar{k}$, is the same as that upstream then the shear is relatively small, and is little affected by the tilt of the interface; it is primarily dominated by the adjustment of the flow since the direction of the pressure gradient is not parallel to the boundaries in the cross-bedded layer far downstream.

Figure 4.7 summarises these results, and also illustrates the sensitivity of the shear to the permeability ratio in the cross-bedded zone, with the shear being enhanced by a larger permeability ratio as expected from figure 4.3. Also, the figure illustrates how the shear depends on the orientation of the interface, with the different lines corresponding to different interface orientations. Indeed, the shear can reverse in sign when interface-induced shear dominates, as already noted in figure 4.5. Figure 4.7(b) also shows the insensitivity of the shear to the angle of tilt in the case that the effective permeability downstream matches that in the isotropic layer upstream (cf. the middle column of panels in figure 4.5).

4.5 Summary

We find that in a composite permeable rock, bounded above and below by impermeable boundaries, and composed of discrete zones of permeable rock, the adjustment of the flow from one zone to the next can lead to distortion of the flow and the generation of a net vertical shear in the averaged flow through the formation. This shear arises from a combination of the inclination of the interface between adjacent zones of rock with different permeability, and also from the change in direction of the pressure gradient as the flow moves from one zone to another, since in cross-bedded layers, the pressure gradient is typically

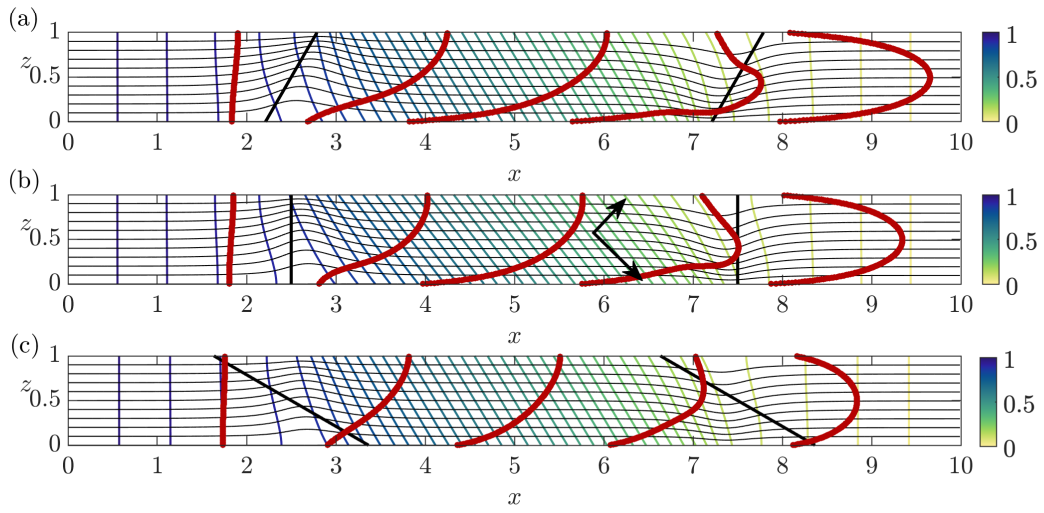

Figure 4.8 Streamlines (thin black curves), pressure contours (thin coloured lines) and tracer locations (thick red lines) at five times after release from $x = 0$. The porous layer consists of an isotropic rock of permeability k_0, while the central trapezoidal region of length $d = 5$ is a cross-bedded zone with permeability ratio across the bedding planes $k_2/k_1 = 4$, and mean effective permeability along the layer $\bar{k}/k_0 = 1/4$. The angle of the bedding is $\theta_i = 45°$, and the direction of permeability within this region is indicated by the arrows in panel (b). Panels (a)-(c) correspond to interface angle $\theta_e = 60°,\ 90°,\ 150°$ respectively (cf. figure 4.5).

not aligned with the direction of the flow (figure 4.1). We have demonstrated how these two different effects may interact and compete, thereby enhancing or reducing the magnitude and the sense of the shear.

In the models presented in this chapter we focus on a single interface to expose the fundamental controls, but in a composite rock, there will likely be multiple zones of rock with multiple associated interfaces. Since the shear associated with each interface typically exhibits a curvature, so that the shear becomes stronger nearer the slower part of the velocity profile (figures 4.2-4.5), then on averaging the flow across multiple interfaces, this is likely to lead to a more symmetrical velocity profile, with a maximum speed near the centre of the channel. Although there are many more calculations which can be carried out, as one simple illustration of this effect we consider the net shear which arises when a finite trapezoid shaped element of cross-bedded material with parallel interfaces is embedded in a uniform porous layer, as shown in figures 4.8(a)-(c). When the interfaces are sufficiently far apart, the transition zone of the pressure gradient for the two interfaces are independent, and the shear associated with each interface are additive. Since the second interface produces a shear which is the mirror image of the first interface, the net effect is a symmetrical velocity profile downstream; as with the earlier results presented in this chapter, the tilted interface may enhance (panel (a)) or reduce (panel (c)) the shear associated with the cross-bedding (panel (b)).

The present results identify that in composite cross-bedded formations bounded by impermeable rock, the flow can develop a strong shear. Using simplified 'effective permeability' values in the direction of the flow for simulation of the transport of tracer, or of a fluid–fluid interface, misses out the effects of shear, which is central for predicting the dispersion and stretching of the flow within this type of bounded porous layer.

Chapter 5

Turbulent mixing in the ocean mixed layer

The material contained in this chapter has been published in *Ocean Modelling*, under the title 'Turbulent mixing of a passive scalar in the ocean mixed layer' (Bhamidipati et al., 2020).

5.1 Introduction

The ocean mixed layer mediates the exchange of mass, momentum and energy between the ocean and the atmosphere (Kantha and Clayson, 1994). The depth of these layers can range from tens to thousands of meters and exhibits large seasonal variations depending on the latitude. The mixing within the surface layer is driven by a range of factors. In the winter or at night, the mixing is largely driven by the convection due to radiative heat loss to the atmosphere, whereas during the summer, the mixing is mainly shear-driven, since the wind stress at the surface is the primary mixing agent. Although the surface wind stress acts to stir light water downwards, most of this energy dissipates rapidly within the top $25 - 30$ m of the ocean. During the summer, increased solar heating of the surface water leads to more stable density stratification, reducing the penetration of wind-driven mixing. Wintertime cooling over the ocean always reduces stable stratification, allowing a deeper penetration of wind-driven turbulence but also generating plumes that can penetrate to great depths (Kraus and Turner, 1967). Therefore, regionally, the mixed layer can become much deeper when convective processes are active (Kara et al., 2003).

From a biological perspective, the ocean mixed layer is nutrient-poor, and its depth determines the average level of light seen by phytoplankton. Therefore, the mixing at the base of the ocean mixed layer is crucial for biological productivity. Since marine biological net primary production is the first step in the food chain of marine organisms, its decline could have severe consequences for fish stock and fisheries (Kuhlbrodt et al., 2009). Biological productivity is also important from a climate point of view: carbon fixation by phytoplankton constitutes a biological pathway for removing some of the anthropogenic CO_2 introduced into the atmosphere. Therefore primary production is also of considerable interest to oceanographers because it contributes significantly to global photosynthesis and ocean carbon uptake (Riebesell et al., 2007; Takahashi et al., 2009).

5.1.1 A review of parameterisations

Proper parameterisation of turbulent mixing in the ocean surface layer is crucial to simulate dynamics in the ocean interior, air–sea exchanges, and sea surface temperature correctly. If model parameterisations are to describe the upper ocean mixing processes accurately, they must be strongly physically based. The existing parameterisations of mixed layer dynamics range from the simple bulk mixed layer models (Kraus and Turner, 1967; Niiler and Kraus, 1977; Price et al., 1986) to models including non-local effects of mixing (Large et al., 1994). The bulk mixed layer model of Kraus–Turner uses an integrated form of the turbulent kinetic energy (TKE) equation, in which the balance is between the generation of turbulence by wind driven mixing and convection, with the work done in overturning the deep stable stratification (Kraus and Turner, 1967). Although such bulk models are popular, they might lose distinctive features such as the non-local transport because of the vertical integrals, and the assumption of homogenisation may breakdown.

Other models require equations for turbulent kinetic energy and its rate of dissipation to estimate the vertical eddy diffusivity. These equations come from carrying out Reynolds decomposition on the Navier–Stokes equations, into a mean flow and a fluctuating component. Since these equations are no longer closed, closure assumptions are required (Acreman and Jeffery, 2007). Common to several of the first-order closure schemes is the assumption that the fluxes depend linearly on the property gradient, with an appropriate constant of

proportionality, which is the eddy diffusivity (cf. §1.2). Other parameterisations have represented the eddy diffusivity as a function of the Richardson number (Pacanowski and Philander, 1981).

Mellor and Yamada (1982) present a second-order turbulent closure model which solves equations for the turbulent kinetic energy and its product with the turbulent length scale. This second-order closure comes from an assumption that the turbulent energy produced by shear and convection is balanced locally by turbulent dissipation. The K-Profile parameterisation (KPP) scheme represents the turbulent mixing of buoyancy using a diffusion equation which has a vertically varying diffusivity along with a counter-gradient term which accounts for non-local transport, whereas the transport of passive tracers is still treated locally (Large et al., 1994). There have also been significant advancements towards enhancement of the KPP scheme, to include the effects of bottom boundary layer (Durski et al., 2004) and Langmuir turbulence (McWilliams and Sullivan, 2000; Smyth et al., 2002). Non-local effects have also been incorporated into schemes other than KPP such as the bulk mixed-layer models (Price et al., 1986), but these are generally ad-hoc.

Recent efforts to parameterise mixing in the ocean boundary layer include the works of Qiao et al. (2004), McWilliams et al. (2009), Li and Fox-Kemper (2017), Reichl and Hallberg (2018), and Reichl and Li (2019). On the other hand, some plume type atmospheric models include a non-local aspect for the transport of a passive tracer since the plumes transport the tracer from the level they start from (Romps and Kuang, 2011; Tan et al., 2018). The work on transilient theory (Stull, 1984, 1993; Stull and Kraus, 1987) is valuable in describing the theory and the merits of such an approach to model the non-local vertical transport by eddies in the upper ocean. The transilient matrix, $\mathcal{K}$, describes the vertical transport by eddies, where each column corresponds to an initial height and each row corresponds to a final height: the element $\mathcal{K}_{ij}$ describes transport from z_j to z_i. If this matrix can be diagnosed for a convecting fluid, it can provide valuable information on the non-local transport by eddies (Romps and Kuang, 2011).

5.1.2 Model description

We begin with a general statement of the relationship between the ensemble mean gradients, $\mathcal{G}_i(x, y, z, t)$, and the ensemble mean fluxes, $\mathcal{F}_i(x, y, z, t)$, of

a scalar (where the subscript represents different components). For a passive scalar, the equation for the fluctuations (the deviations from the mean) is linear and is forced by the advection of the mean gradients by the fluctuating velocity; therefore the scalar fluctuations and the fluxes are linear functionals of the mean gradients:

$$\mathcal{F}_i(x,y,z,t) = -\int \mathcal{K}_{ij}(x,y,z,t|x',y',z',t')\mathcal{G}_j(x',y',z',t')\,\mathrm{d}x'\,\mathrm{d}y'\,\mathrm{d}z'\,\mathrm{d}t', \tag{5.1}$$

where the summation convention is used for repeated indices.

In this chapter, we focus on estimating this exact formulation of the flux as a functional of the property gradient, using high resolution simulations to determine the form of the functional. For the mixed layer, we can reduce the order of the kernel by assuming that the statistics have no horizontal variation so that it becomes $\mathcal{K}(z,t|z',t')$. Finally, to further simplify the computation and the portrayal of the kernel, we will deal with the statistically steady state. This will be appropriate if the time-scales for the changes in the tracer distribution or the other mixed layer properties are slow enough. Furthermore, we use temporal and spatial averages instead of ensemble averages. In this idealised case, the appropriate eddy diffusivity kernel, $\mathcal{K}(z|z')$, describes the vertical transport by eddies at any vertical location z arising from gradients at z'.

We emphasise that the work presented in this chapter does not propose a new parameterisation; to do that, many of the effects such as winds and time-dependence would need to be brought back in and examined carefully. Instead, our study provides insight into how fluxes are related to gradients, gives an example of such a calculation, and, we hope, suggests approaches to parameterisation.

For simplicity, we restrict our focus to convection-driven mixing using an idealised 2D surface layer of the ocean, where a balance of fluxes persists long enough for the system to reach a dynamical equilibrium. Although 3D effects appear soon after the onset of convective instability, the 2D problem can describe both the instability and some of the effects of non-linearity. For example, Taylor and Ferrari (2010) find good agreement of the mean profiles and turbulent features between 2D and 3D large eddy simulations of slantwise convection with a horizontal buoyancy gradient, forced by either surface wind

stress or surface buoyancy flux. Furthermore, while 2D simulations do not work well for fingering convection in the limit of low Prandtl number Garaud and Brummell (2015), Schmalzl et al. (2004) find that, for higher values of the Prandtl number ($Pr > 1$), the flow structure and global quantities (e.g., Nusselt number and Reynolds number) exhibit similar behaviour in 2D and 3D simulations. In the context of atmospheric boundary layer convection, Moeng et al. (2004) have found that certain properties, such as the vertical distribution of heat flux, are not sensitive to the choice of 2D versus 3D, although the same may not hold true when there is a mean shear. The authors argue that 2D models can be themselves thought of as a parameterisation of 3D physics.

In §5.2, we discuss the basic equations governing the 2D system and derive an equation for the mixed layer depth (MLD), based on a balance between the imposed fluxes. We also present the results from our 2D DNS to describe the evolution of buoyancy in the domain. In §5.3, we use passive tracers to describe the turbulent mixing in terms of an eddy diffusivity kernel, and propose a method to compute the kernel based on a proper representation of the physics. Although the analysis in this section is strictly only applicable for a passive scalar, in §5.4 we compare the diagnosed buoyancy fluxes to our estimate using the kernel and the corresponding buoyancy gradients. Finally, in §5.5, we discuss the relevance of this study and indicate further directions for future work.

5.2 Governing equations

We begin with the two-dimensional Boussinesq equations.

$$\nabla \cdot \mathbf{u} = 0, \tag{5.2a}$$

$$\frac{\partial \mathbf{u}}{\partial t} + (\mathbf{u} \cdot \nabla)\mathbf{u} = -\frac{\nabla p}{\rho_o} + \nu \nabla^2 \mathbf{u} + b\hat{z}, \tag{5.2b}$$

$$\frac{\partial b}{\partial t} + \mathbf{u} \cdot \nabla b = \kappa \nabla^2 b + \frac{\mathrm{d}}{\mathrm{d}z}(Q(z)), \tag{5.2c}$$

where $\mathbf{u} = (u, w)$ is the fluid velocity, p is the pressure, ρ_o is the mean density, ν is kinematic viscosity, and κ is thermal diffusivity. We assume that the fluid buoyancy, b, is a function only of temperature, T, so that $b = \alpha g T$, where α is the coefficient of thermal expansion and g is acceleration due to gravity. The

equation governing buoyancy has an added internal heating term to account for penetrative solar radiation. This flux is represented as $Q(z) = Q_o e^{z/l}$, where $Q_o = H_o(\alpha g)/(\rho_o C_p)$, H_o is the surface heat flux, C_p is the specific heat capacity of the fluid, l is the vertical decay scale, and z is the vertical space coordinate, negative downward with origin at sea level. The attenuation length, l, for solar radiation of short wavelength is approximately 20 m, whereas longer wavelengths get absorbed over a much shallower depth, approximately 0.5 m (Paulson and Simpson, 1977). Therefore, in our calculations we use $l = 20$ m. In general, the surface heat flux varies both diurnally and seasonally, but here we restrict our attention to a constant surface heat flux to study the statistical steady state.

We assume that the top and bottom boundaries are free-slip and impermeable. The buoyancy flux at the bottom boundary is that necessary to maintain the Brunt–Väisälä frequency of the thermocline.

$$\left.\begin{aligned} w = 0, \quad \frac{\partial u}{\partial z} = 0, \quad \kappa\frac{\partial b}{\partial z} = \kappa N^2 \qquad &\text{at} \quad z = -H \\ w = 0, \quad \frac{\partial u}{\partial z} = 0 \qquad &\text{at} \quad z = 0 \end{aligned}\right\} \tag{5.3}$$

with $H \gg l$. We further assume that a radiative cooling at the surface is specified so that the net flux in the system is zero, and the system reaches a statistical steady state. This simplification allows us to estimate a kernel that is stationary in time and only depends on the stationary statistics of the flow field. Furthermore, although we use this specific scenario in which a quasi-steady state approximation applies because of a net balance of fluxes, we emphasise again that subsequent approach to represent mixing in the surface layer as a functional of the mean gradients can be extended to a more general time-varying problem, where the eddy flux kernel is given as $\mathcal{K}(z, t|z', t')$ (cf. equation (5.1)).

Taking the horizontal average of equation (5.2c), where $\overline{*} = L^{-1}\int_0^L * \, \mathrm{d}x$ denotes horizontal average, we obtain the boundary condition for buoyancy at $z = 0$, i.e., the radiative cooling at the surface,

$$\frac{\partial \overline{b}}{\partial t} = -\frac{\partial}{\partial z}\left(\overline{w'b'} - Q_o e^{z/l} - \kappa\frac{\partial \overline{b}}{\partial z}\right), \tag{5.4}$$

where $b'(x, z, t)$ is the buoyancy perturbation ($b = \overline{b}(z, t) + b'(x, z, t)$). Assuming a quasi-steady evolution so that $\partial\overline{b}/\partial t = 0$, and integrating over the depth of

the domain from $z = -H$ to $z = 0$ gives the boundary condition for buoyancy at $z = 0$,

$$\kappa \frac{\partial \bar{b}}{\partial z}\bigg|_{z=0} = \kappa N^2 - Q_o(1 - e^{-H/l}). \tag{5.5}$$

The system is in dynamical equilibrium, and so we expect it to reach a statistical steady state. If $\partial b/\partial z < 0$ at the surface, we have colder fluid overlying hotter fluid. Therefore, $Q_o/\kappa N^2 > 1$ is a necessary condition for convection to occur, but it is not a sufficient condition since the fluid also needs to overcome viscous forces, as defined by the Rayleigh number. We non-dimensionalize the problem by defining the following dimensionless variables.[1]

$$\tilde{t} = \frac{t\kappa}{l^2}, \quad \tilde{\mathbf{u}} = \frac{\mathbf{u}l}{\kappa}, \quad \tilde{b} = \frac{bl^3}{\kappa^2}, \quad \tilde{p} = \frac{p\rho_o l^2}{\kappa^2} \tag{5.6}$$

The dimensionless equations are (dropping the tildes)

$$\nabla \cdot \mathbf{u} = 0, \tag{5.7a}$$

$$\frac{\partial \mathbf{u}}{\partial t} + (\mathbf{u} \cdot \nabla)\mathbf{u} = -\nabla p + \mathrm{Pr}\nabla^2 \mathbf{u} + b\hat{z}, \tag{5.7b}$$

$$\frac{\partial b}{\partial t} + \mathbf{u} \cdot \nabla b = \nabla^2 b + Fe^z, \tag{5.7c}$$

where the following non-dimensional parameters are defined,

$$F = \mathrm{Pr}\ \mathrm{Ra}_f = \frac{Q_o l^4}{\kappa^3}, \quad \mathrm{Pr} = \frac{\nu}{\kappa}, \quad \mathrm{Ra}_f = \frac{Q_o l^4}{\nu\kappa^2}, \quad \Phi = \frac{N^2 l^4}{\kappa^2}. \tag{5.8}$$

Here, Pr is the Prandtl number, Ra_f is the flux Rayleigh number, F is a measure of the penetrative shortwave heat flux, and Φ is a measure of the

[1] Note that our particular choice of non-dimensionalisation is arbitrary since we do not make any approximations on the basis of the non-dimensionalisation.

Table 5.1 Values of dimensionless parameters used in simulations, where h is the MLD.

L_x	L_z	Pr	F	Φ	(N_x, N_z)	$h = \ln \frac{F}{\Phi}$
4	16	10	8×10^6	8×10^5	(128,512)	2.302
4	16	10	1.6×10^7	8×10^5	(128,512)	2.996
4	16	10	2.4×10^7	8×10^5	(128,512)	3.401
4	16	10	3.2×10^7	8×10^5	(128,512)	3.689

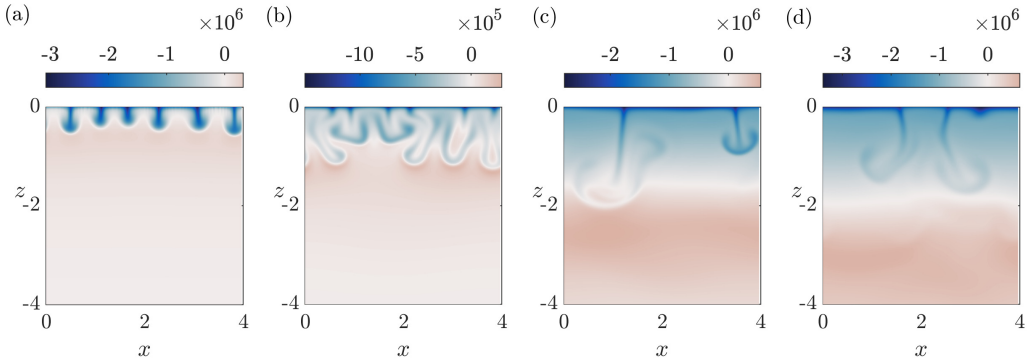

Figure 5.1 The panels show the evolution of the deviation of buoyancy field, $b(x, z, t) - \Phi z$, at four times, $t = 0.03, 0.04, 0.49, 1.10$ for $F/\Phi = 20$.

stratification the deep thermocline. The dimensionless boundary conditions are now given by,

$$\left.\begin{aligned} w = 0, \quad \frac{\partial u}{\partial z} = 0, \quad \frac{\partial b}{\partial z} = \Phi \qquad & \text{at} \quad z = -L_z \\ w = 0, \quad \frac{\partial u}{\partial z} = 0, \quad \frac{\partial b}{\partial z} = \Phi - F(1 - e^{-L_z}) \qquad & \text{at} \quad z = 0 \end{aligned}\right\} \tag{5.9}$$

where $L_z = H/l$ is the dimensionless depth of the domain. The domain extends from 0 to L_x in the horizontal direction. We assume zero base flow so that the fluid velocity is given by the perturbation velocity $\mathbf{u}'$ ($\mathbf{u} = \mathbf{0} + \mathbf{u}'$, where $\mathbf{u}' = (u', w')$).

5.2.1 Numerical simulations

We solve equations (5.7a–c) using the Dedalus pseudo-spectral code (Burns et al., 2019). We discretize the domain using N_x Fourier modes in the horizontal direction and N_z Chebyshev modes in the vertical direction, so that the smallest length scales in the vertical are $\mathcal{O}(10)$ mm and the resolution at the base of the

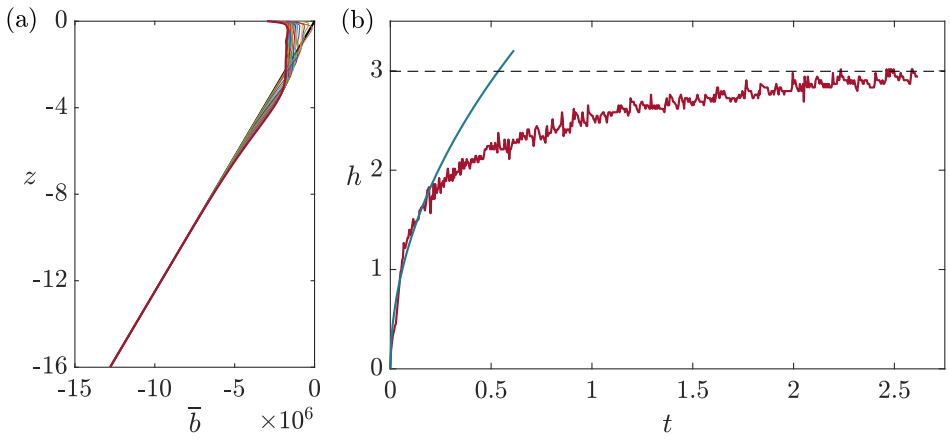

Figure 5.2 (a) Horizontally averaged buoyancy, $\overline{b}$, plotted at various times as represented by the different colours, starting with a linear profile (black line) at $t = 0$. (b) The variation of MLD, h, versus time, t. The horizontal line represents $h = \ln(F/\Phi)$ and the blue curve represents $h \sim \sqrt{t}$. Here, the ratio of the penetrating shortwave heat flux to the diffusive heat flux in the deep thermocline is $F/\Phi = 20$.

mixed layer is $\mathcal{O}(100)$ cm for our chosen parameter values. For time-stepping, we use a two-stage second-order Runge-Kutta method, where the linear terms are treated implicitly, and non-linear terms are treated explicitly. The time-step size is set by a Courant-Friedrichs-Lewy condition with prefactor 0.5. We choose a sufficiently large domain depth in order to mitigate the effects of internal gravity waves, generated by turbulent plumes hitting the base of the mixed layer, reflecting off of the bottom boundary. Table 5.1 shows the range of parameter values used in the simulations.

We initialise the problem by specifying a linear buoyancy field, $b = \Phi z$, and adding a small perturbation. Because of the surface cooling, the perturbation to buoyancy field produces horizontal buoyancy gradients which, in turn, begin to produce vorticity. The flows will further lift the light fluid and draw the heavier fluid down; the layer tries to overturn. Figure 5.1 shows the evolution of the deviation of buoyancy field, $b - \Phi z$, in the domain. In figure 5.1, the four panels show convective plumes descending from the surface, and generating dipolar vortices which increase the downward speed. Note the internal waves, generated as the plume hits the stratified base of the convective region. The plumes drive the turbulent mixing of the linear buoyancy field forming a fairly homogeneous region—a mixed layer—which deepens over time.

5.2.2 The depth of the mixed layer

Figure 5.2(a) shows the time-evolution of the horizontally averaged buoyancy field, $\bar{b}$, starting with an initially linear profile. The depth of this mixed region initially grows as $\sqrt{t}$ as expected of penetrative convection (Van Roekel et al., 2018), but eventually settles to a constant value (figure 5.2(b)).

We can estimate the mixed layer depth (MLD), h, using convective adjustment ideas; however, the naive approach of adjusting the diffusive profile that matches the boundary condition ends up with non-zero heat flux divergence. Instead, we can solve the initial value problem starting with the constant stratification and turning on the radiative heat flux in the interior and boundary conditions, with convective adjustment occurring whenever $\partial\bar{b}/\partial z < 0$. However, the end state can be found by setting $\partial\bar{b}/\partial t = 0$ in the non-dimensional form of equation (5.4) and integrating up from the bottom to find

$$\overline{w'b'} - Fe^{z} - \frac{\partial \bar{b}}{\partial z} = -\Phi, \tag{5.10}$$

neglecting the radiative flux at the bottom of the domain, i.e., $e^{-H/l} \approx 0$ for $H \gg l$. When $Fe^{-h} = \Phi$, the flux balance in the water below the mixed layer will be achieved for $\partial\bar{b}/\partial z = 0$ at $z = -h$. In the convecting layer, we must also have $\overline{w'b'} - \partial\bar{b}/\partial z = 0$ at that depth. This is consistent with the mixed layer buoyancy being constant and the eddy flux vanishing at the base of the mixed layer. Thus we settle to a constant flux state when

$$h = \ln\left(\frac{F}{\Phi}\right) \tag{5.11}$$

so that the mixed layer descends to the depth where the gradient of $\bar{b}$ in the diffusive solution changes sign.[2] Overshooting plumes may lead to some mixing below this depth resulting in a reversal in sign of the buoyancy flux; however, that is weak in the experiments since the mixed layer depth is comparable to the attenuation length for solar radiation. Choosing the base of the mixed layer to be where $\overline{w'b'} = 0$ still gives the value given by equation (5.11) since the gradient of $\bar{b}$ is nearly zero at $z = -h$ (see figure 5.2(a)). Near the surface, the eddy flux, $\overline{w'b'}$, vanishes so that the balance is between the diffusive flux and the solar heating. Correspondingly, the horizontally averaged buoyancy profile

[2]From equation (5.4), the deepening effectively halts and we reach a steady state when the buoyancy flux from the convective plumes can balance the heat fluxes.

shows a negative gradient close to the surface. In contrast, within the mixed layer, the vertical convective flux nearly balances the heating throughout the mixed layer.

Henceforth, we describe the mixed layer depth (MLD) using the non-dimensional parameter, F/Φ, which is the ratio of the penetrating heat flux to the diffusive heat flux in the deep thermocline (see table 5.1).

5.3 Mixing of a passive scalar

Equation (5.7c) is analogous to an advection–diffusion equation for a passive scalar given by

$$\frac{\partial c}{\partial t} + \mathbf{u} \cdot \nabla c = \nabla^2 c + \frac{\mathrm{d}}{\mathrm{d}z}(f(z)), \tag{5.12}$$

where $c(x, z, t)$ is the concentration of tracer, and $f(z)$ is a forcing function or source term for the tracer. Additionally, we define the boundary conditions for the tracer,

$$\frac{\partial c}{\partial z} = 0 \quad \text{at} \quad z = 0, -L_z. \tag{5.13}$$

Taking a horizontal average of equation (5.12) and using the continuity equation, we obtain

$$\frac{\partial \overline{c}}{\partial t} + \frac{\partial}{\partial z}\overline{w'c'} = \frac{\partial^2 \overline{c}}{\partial z^2} + \frac{\mathrm{d}}{\mathrm{d}z}(f(z)). \tag{5.14}$$

Splitting the concentration into a horizontally averaged part and a fluctuating part ($c = \overline{c}(z, t) + c'(x, z, t)$) and substituting this into equation (5.12) gives, after subtraction of equation (5.14),

$$\left(\frac{\partial}{\partial t} + \mathbf{u}.\nabla - \nabla^2\right) c' - \frac{\partial}{\partial z}\overline{w'c'} = -w'\frac{\partial \overline{c}}{\partial z}. \tag{5.15}$$

The integro-differential operator on the left-hand side of equation (5.15) is linear if we have a specified flow field, $\mathbf{u}$. So we can easily show that c' and the eddy flux, $\overline{w'c'}$, will be linear functionals of $\partial\overline{c}/\partial z$ (see appendix B). This

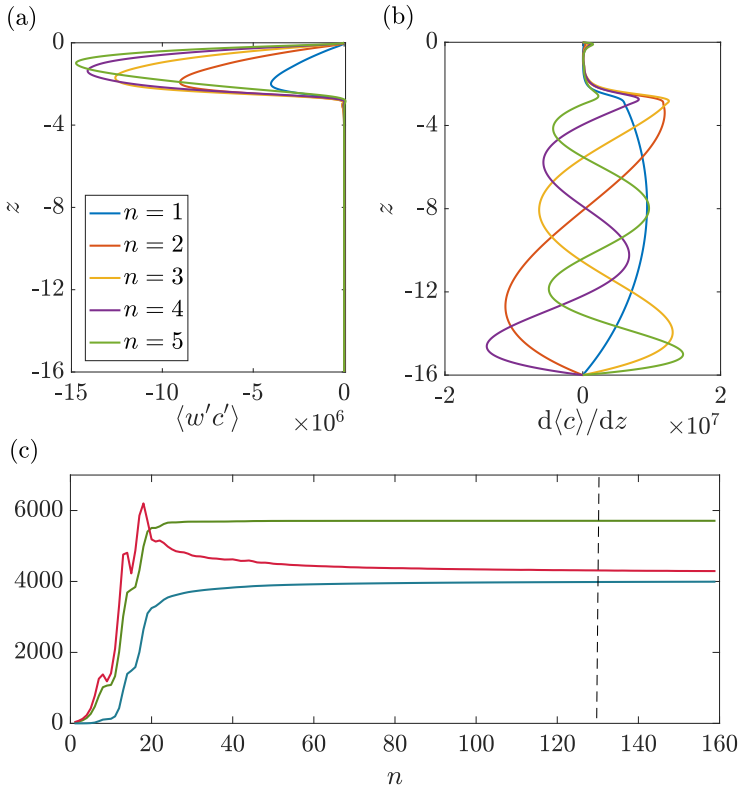

Figure 5.3 Panels (a) and (b) show the horizontally averaged eddy fluxes, $\langle w'c' \rangle$, and gradients, $\mathrm{d}\langle c \rangle / \mathrm{d}z$, for the tracer, corresponding to the forcing function $f_n(z)$ where $n = 1, 2, 3, 4, 5$. (c) Convergence of the kernel, $\mathcal{K}(z|z')$, with the number of tracers, n. The different curves correspond to different measures of convergence: the maximum eigenvalue (multiplied by 100 for scale, green curve), sum of the absolute values of $\mathcal{K}(z|z')$ (red curve), and the sum of the squares of $\mathcal{K}(z|z')$ (blue curve). The black dotted line represents $n = 128$. In these calculations, the ratio of the penetrating shortwave heat flux to the diffusive heat flux in the deep thermocline is $F/\Phi = 10$.

implies that the horizontally and temporally averaged fluxes are a functional of the horizontally and temporally averaged gradients.

$$\langle w'c' \rangle = -\int \mathcal{K}(z|z') \frac{\partial \langle c \rangle (z')}{\partial z'} \mathrm{d}z' \tag{5.16}$$

with $\langle * \rangle = \lim_{\tau \to \infty} \tau^{-1} \int_0^\tau * \, \mathrm{d}t$ (see appendix B).

5.3.1 Choice of the forcing function

In the discrete form used for the numerics, equation (5.16) can be written for a particular forcing function, f_k, as

$$\langle w'c'\rangle_{ik} = -\mathcal{K}(z_i|z_j)\frac{\partial\langle c\rangle_j}{\partial z'_k}\Delta z_j = -\mathcal{K}_{ij}\frac{\partial\langle c\rangle_j}{\partial z'_k}\Delta z_j, \tag{5.17}$$

with the appropriate summation convention; the goal is to find the matrix $\mathcal{K}_{ij}$. We solve equation (5.12) from zero initial conditions, holding $f = f_1(z)$ fixed, and compute to a statistical steady state giving one pair of $\langle w'c'\rangle_{i,1}$ and $\langle c_z\rangle_{i,1}$ vectors (note that, here, $\langle c_z\rangle \equiv \mathrm{d}\langle c\rangle/\mathrm{d}z$).

To obtain linearly independent data pairs for both $\langle w'c'\rangle$ and $\partial\langle c\rangle/\partial z$, we could define the forcing function, $f(z)$, as

$$f(z) \equiv f_k(z) = F \times \left(T_{k+1}\left(\frac{2z}{L_z}+1\right) - \left(\frac{z}{L_z}\right)\Big[T_{k+1}(1) - T_{k+1}(-1)\Big]\right), \tag{5.18}$$

where $T_k(z) = \cos(k\cos^{-1}(z))$ are Chebyshev polynomials of first kind. This definition of $f_k(z)$, which includes the subtraction of a linear term, ensures that the domain averaged concentration, found by integrating equation (5.14) in z, remains constant in time and the system reaches a statistical steady state.

If we define $\mathrm{d}f(z)/\mathrm{d}z$ in a way that its vertical integral is not zero, i.e., without subtracting the linear part from $f(z)$, then we would have $\partial\overline{c}/\partial t$ tending to a constant. This, however, would have no effect on the fluxes and gradients of tracer, and they would still converge to statistically steady values in time. Therefore in our simulations we have defined $f(z)$ as

$$f(z) \equiv f_n(z) = F \times \left[T_{n+1}\left(\frac{2z}{L_z}+1\right)\right] \tag{5.19}$$

in order to estimate the kernel $\mathcal{K}(z|z')$ given by equation (5.16).

We repeat the experiment n times, using n passive tracers to reach n linearly independent statistically steady states. Collecting the experiments into $m \times n$ matrices, with $m = 512$ being the number of modes used to discretize the domain in z and n being the number of tracers, gives $\mathcal{F} \equiv \langle w'c'\rangle_{ik}$ and $\mathcal{G} \equiv \Delta z_j\big(\partial\langle c\rangle_j/\partial z_k\big)$. The eddy diffusivity kernel $\mathcal{K}$ can be estimated using a least-squares fit of the discrete data as $\mathcal{K} = -\mathcal{F}(\mathcal{G}^T\mathcal{G})^{-1}\mathcal{G}^T$.

Figures 5.3(a)-(b) show the fluxes and gradients of the passive scalar for $n = 1, 2, 3, 4, 5$. Figure 5.3(c) shows the convergence of the kernel with n as we add more tracers to compute the fluxes and gradients. We choose $n = 128$ tracers since the results do not vary significantly as we add more tracers (figure 5.3(c)).

5.3.2 The eddy diffusivity kernel

Figure 5.4(a) shows the kernel for $n = 128$ tracers and for a given ratio of the penetrating shortwave heat flux to the diffusive heat flux in the deep thermocline ($F/\Phi = 10$). In this figure, the horizontal axis gives the centre of a delta function forcing for an arbitrary function, $f(z)$, represented as the sum of delta functions, and the vertical axis gives the response, with the diagonal elements (going from lower-left to upper-right) representing the local contributions. Figure 5.4(a) illustrates that the mixing is strongest within the mixed layer, and the large off-diagonal elements illustrate that both local and non-local effects of mixing are significant within the convective region. Figure 5.4(b) shows the very weak eddy flux associated with the internal gravity waves in the region below the mixed layer.

Figure 5.5 shows the kernel for four different values of the mixed layer depth obtained by varying the non-dimensional parameter F/Φ. The local effects of mixing can be seen from the diagonal elements of $\mathcal{K}(z|z')$; this is shown in figure 5.6(a) where the vertical axis has been non-dimensionalized by MLD, $h = \ln(F/\Phi)$. The figure illustrates that the eddy diffusivity decays rapidly in the region outside the mixed layer, for $|z/h| > 1$. The non-local effects of mixing can be interpreted by looking at a horizontal slice in figure 5.5; this is shown in figure 5.6(b) for a location in the middle of the mixed layer. The figure shows the contributions from forcing at different levels to the response in eddy flux at $z/h = -0.5$, i.e., in the middle of the convecting layer. The figure illustrates that although the local effects are strongest as indicated by the peak at $z/h \approx -0.5$ i.e., that the flux at that level has the biggest contributions from the gradient at that level, more importantly, it highlights that the flux at that level also has leading-order contributions from gradients above that level. The stronger contributions from gradients above the forcing location are due to the convective plumes descending from the surface which have large momentum.

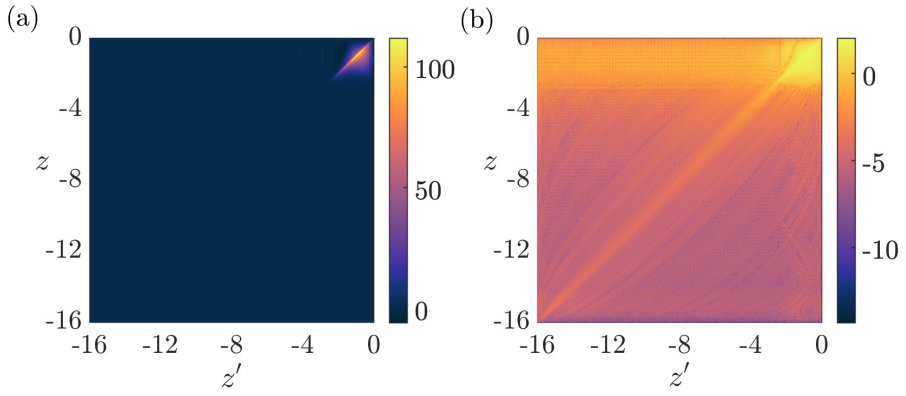

Figure 5.4 (a) $\mathcal{K}(z|z')$. (b) $\log_{10}|\mathcal{K}(z|z')|$. In these calculations, the ratio of the penetrating shortwave heat flux to the diffusive heat flux in the deep thermocline is $F/\Phi = 10$, and the kernel is computed using $n = 128$ tracers.

However, we observe weak contributions from the gradients below this point due to the upward plumes having petered out by the time they reach the top.

5.4 Eddy buoyancy flux

The analysis presented in §5.3 is strictly only applicable for a passive scalar since the fluxes, $\langle w'c'\rangle$, are linear in c', whereas $\langle w'b'\rangle$ is non-linear since w' is a function of the buoyancy b. However, we can compare the eddy flux, $\langle w'b'\rangle$, obtained from the experiments to an estimate using the kernel, $\mathcal{K}(z|z')$, and the diagnosed gradients, $\partial\langle b\rangle/\partial z$. A comparison between the two fluxes is shown in figure 5.7(a) for four values of MLD.

It is worth noting that the flow is generated by the buoyancy, b, and that the kernel, $\mathcal{K}$, is dependent on statistics of the flow field. While figure 5.7(a) illustrates that the estimate of the eddy flux using the kernel gives a consistent representation of the buoyancy fluxes, the same would not hold true if a buoyancy anomaly was created by a different active scalar affecting the flow field since this is not taken into account in estimating $\mathcal{K}$. Nevertheless, this calculation does indeed show that the kernel is in fact consistent with the fluxes of buoyancy. Additionally, it is also worth noting that although the fluxes do decay rapidly outside the convective region, for $|z/h| > 1$, the fluxes are non-linear and we do not expect a self-similar solution applicable to all examples of convective mixing. Indeed, we see that the kernel is not similar in z/h even for a passive scalar (figure 5.6).

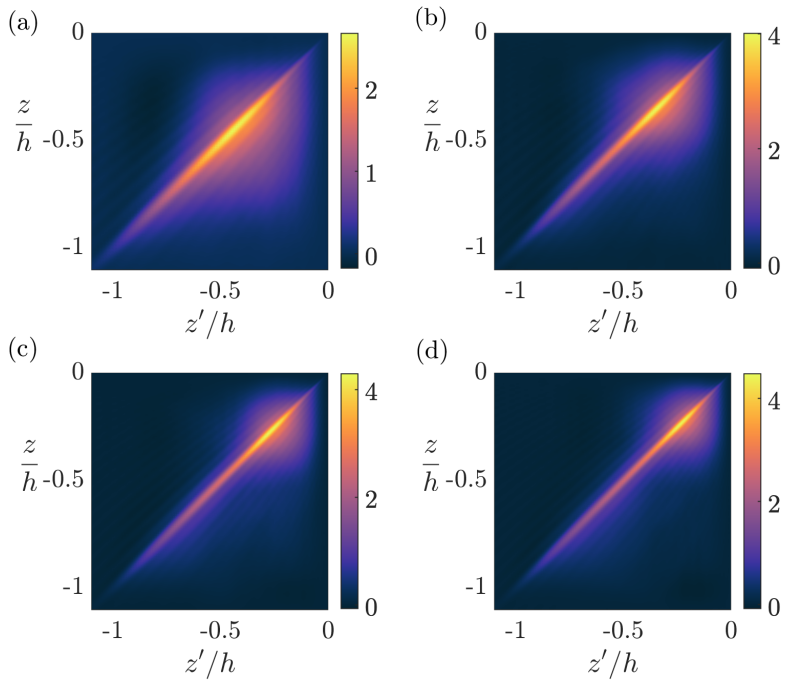

Figure 5.5 Panels (a)-(d) show the kernel, $\mathcal{K}(z/h|z'/h)$, for four different values of MLD, $h = \ln(F/\Phi)$, obtained by varying the ratio of the penetrating shortwave heat flux to the diffusive heat flux in the deep thermocline, where $F/\Phi = 10, 20, 30, 40$ respectively.

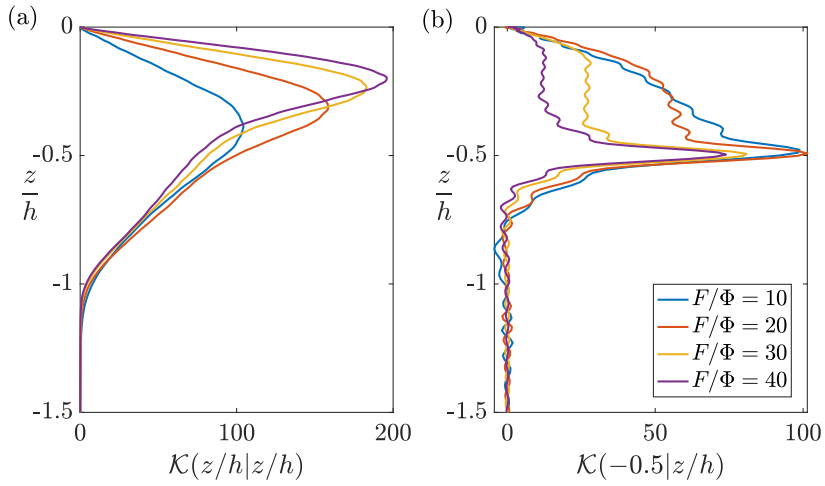

Figure 5.6 (a) The diagonal elements of the kernel, showing the local effect of the mixing, plotted against z/h, where h is the MLD. (b) A horizontal slice of $\mathcal{K}(z/h|z'/h)$ in the middle of the mixed layer at $z/h = -0.5$, illustrating the non-local effects of mixing for four different values of MLD. In each case, the MLD is defined as the ratio of the penetrating shortwave heat flux to the diffusive heat flux in the deep thermocline, $h = \ln(F/\Phi)$.

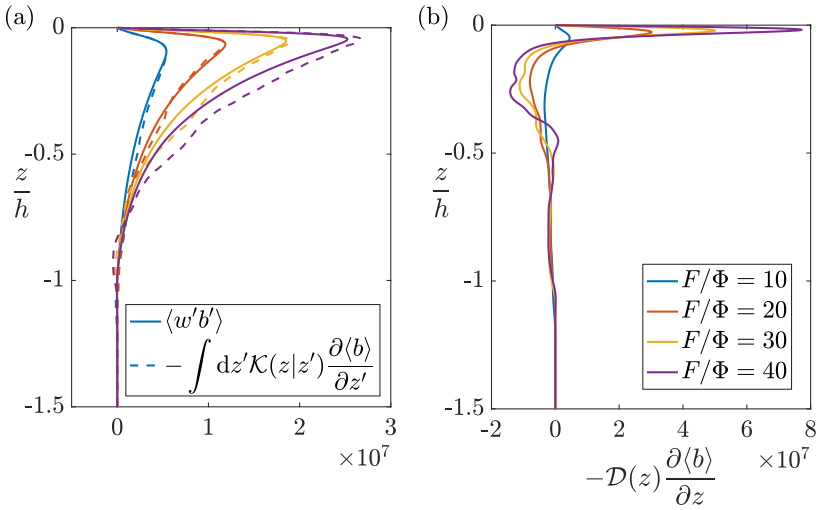

Figure 5.7 (a) Comparison of the eddy fluxes, $\langle w'b' \rangle$ (solid curve), with the estimate from the kernel, $-\int \mathrm{d}z' \mathcal{K}(z|z') \partial b/\partial z$ (dashed curve), for four different MLD. (b) An estimate of the flux using the appropriate local diffusivity, $\mathcal{D}(z)$, for four different values of MLD. In each case, the MLD is defined as the ratio of the penetrating shortwave heat flux to the diffusive heat flux in the deep thermocline, $h = \ln(F/\Phi)$.

We further investigate the importance of non-local effects by defining an effective local diffusivity, $\mathcal{D}(z)$, so that

$$\mathcal{K}(z|z') = \mathcal{D}(z)\delta(z - z') \implies \mathcal{D}(z) = \int \mathcal{K}(z|z')dz'. \tag{5.20}$$

The estimates of the flux using the appropriate local diffusivity is shown in figure 5.7(b), which illustrates the significance of the non-local terms in describing the transport both qualitatively and quantitatively.

5.5 Summary

The mixing of a passive tracer in the the surface mixed layer of the ocean is given by a non-local formulation of the eddy flux in terms of the mean gradient, $\langle w'c' \rangle = -\int \mathrm{d}z' \mathcal{K}(z|z') \partial \langle c \rangle / \partial z'$, where $\mathcal{K}(z|z')$ is the eddy diffusivity kernel. Although several non-local parameterisations have been defined in literature, the analysis presented in this chapter does not use any closure assumptions, and therefore the functional form of eddy diffusivity gives an unapproximated representation of the chosen physics. We demonstrate that the eddy flux can be

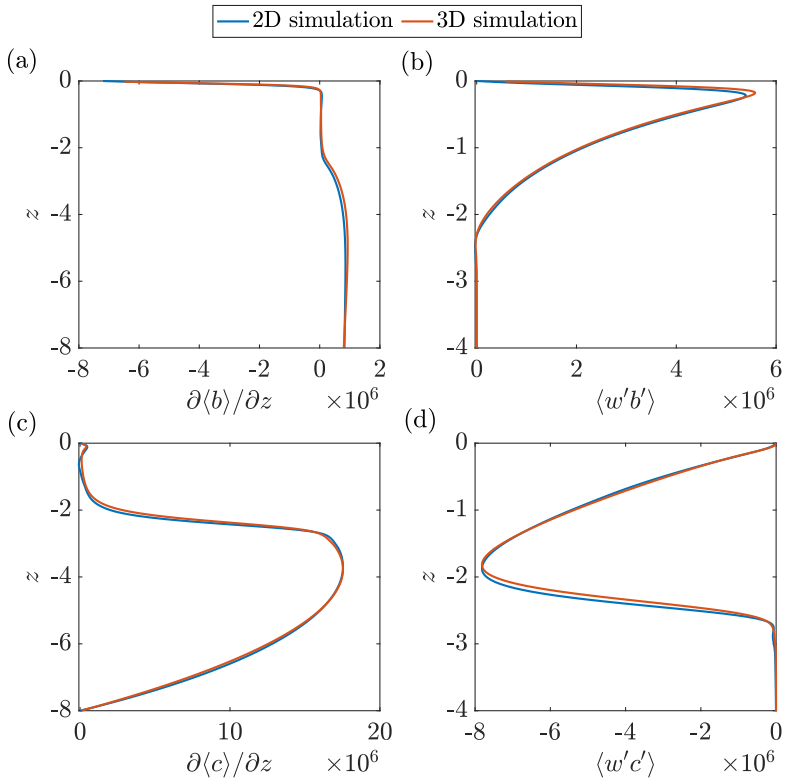

Figure 5.8 Comparison of the horizontally and temporally averaged fluxes and gradients of buoyancy and passive tracer in 2D and 3D simulations with the same boundary conditions. The 3D simulations are done using a finite volume code (Ramadhan et al., 2020) whereas the 2D simulations use a pseudo-spectral code (Burns et al., 2019). In both sets of simulations, the ratio of the penetrating shortwave heat flux to the diffusive heat flux in the deep thermocline is $F/\Phi = 10$, so that the MLD is $h = \ln(F/\Phi) \approx 2.3$. The profiles for the passive tracer are estimated by solving equation (5.12) where $f(z)$ is given by equation (5.19) for $n = 1$.

expressed as a functional of the gradient, and compute the full eddy diffusivity kernel by resolving the small scales.

We consider an idealised 2D convection-driven mixed layer dynamics and give an estimate for MLD as given by a balance between the surface fluxes and the buoyancy flux of the thermocline; this analysis is therefore directly applicable to situations where convection is the dominant process in causing mixed layer deepening. To further illustrate that this analysis is equally applicable to a 3D case, we have looked at an example of the balanced state in three dimensions and find that the structure of the gradients and fluxes of both buoyancy and passive tracer are very similar to the 2D DNS (see figure 5.8).

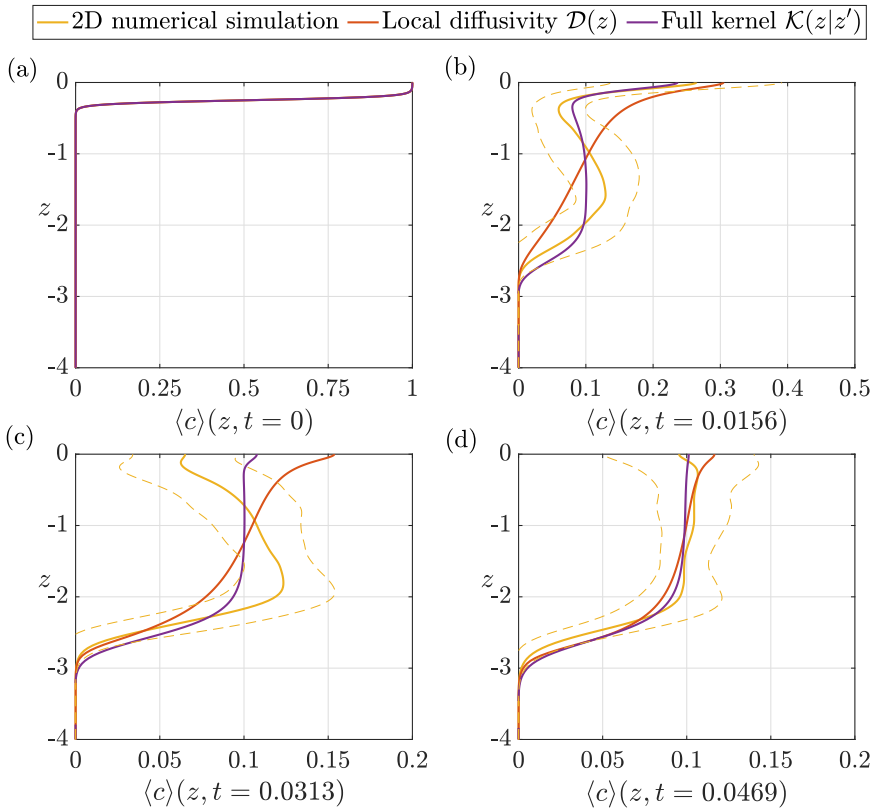

Figure 5.9 Panels (a)-(d) show the time-evolution of a passive tracer added to the flow near the surface, as given by the 2D DNS, and solution to equations (5.21a) and (5.21b). The yellow dotted curves represent one standard deviation from the mean ensemble profile (yellow curve) obtained by averaging 100 realisations in the 2D DNS. Panel (a) shows the initial profile at $t = 0$ which is given by equation (5.22) for $d = 0.25$. In these calculations, the ratio of the penetrating shortwave heat flux to the diffusive heat flux in the deep thermocline is $F/\Phi = 10$.

The mixed layer deepens as the surface fluxes are increased relative to the buoyancy fluxes at the thermocline, in accordance with the theoretical formulation of MLD. At early times, the mixed layer deepens as square root of time, but eventually settles to a near constant value given by the location where the fluxes due to solar heating balance the buoyancy flux of the thermocline.

The kernel describes both the local and non-local effects of mixing, illustrating that for this flow, the non-local effects are strongest closer to the surface because of the energy of the convective plumes detaching from the surface. The non-local effects are therefore important in transporting properties from one side of the boundary layer to the other as illustrated in figure 5.1. To

further understand the mixing of a passive tracer by the flow, the importance of non-local effects can be illustrated by adding a tracer near the surface and studying its distribution a short time later. To do this, we solve

$$\frac{\partial\langle c\rangle}{\partial t} = \frac{\partial}{\partial z}\left(\mathcal{D}(z)\frac{\partial\langle c\rangle}{\partial z}\right) + \frac{\partial^2\langle c\rangle}{\partial z^2}, \tag{5.21a}$$

$$\frac{\partial\langle c\rangle}{\partial t} = \frac{\partial}{\partial z}\left(\int \mathcal{K}(z|z')\frac{\partial\langle c\rangle}{\partial z'}\mathrm{d}z'\right) + \frac{\partial^2\langle c\rangle}{\partial z^2}, \tag{5.21b}$$

which describe the time-evolution of the ensemble-averaged concentration, $\langle c\rangle(z,t)$, as mixed by the diagnosed local diffusivity, $\mathcal{D}(z)$, given by equation (5.20) and the full kernel, $\mathcal{K}(z|z')$, respectively. Since the flow is in a statistically steady state, we would expect that the tracer distribution given by the solution to both equations (5.21a) and (5.21b) would be very similar at late times. We begin with

$$\langle c\rangle(z, t=0) = \frac{1}{2}\Big[\tanh(20(z+d)) + 1\Big]. \tag{5.22}$$

The equivalent profiles from the 2D DNS can be obtained by adding passive tracers to the statistically steady flow, i.e., solving equation (5.12) with $f(z) = 0$, and with the same initial condition for the tracer concentration, $c(x,z,t)$ (equation (5.22)). We add 100 tracers to the flow at different times to obtain the ensemble and horizontally averaged profiles, $\langle c\rangle(z,t)$. This is shown in figure 5.9. As the figure illustrates, the profiles given by the full kernel better describe the transient evolution of the tracer at early times. The profiles obtained using (equation (5.21b)) are within one standard deviation of the profiles obtained from the 2D DNS, whereas the equivalent profiles from the local diffusivity (equation (5.21a)) lie outside this range. Although both solutions (equations (5.21a) and (5.21b)) converge rapidly, the figure highlights that the kernel contains information pertaining to the non-locality of the flow that is missing from a local diffusivity. This non-local behaviour might be especially important for transient processes that occur on short timescales, where the non-local fluxes could lead to qualitative macroscopic differences in properties in the ocean mixed layer.

The kernel, $\mathcal{K}(z|z')$, depends on the statistics of the flow field and is computed here for advection of a passive scalar by a fully non-linear turbulent

flow field. Within the mixed layer, the kernel is non-local since plumes transport properties from one level to the other by advection. The non-local fluxes move the tracer around with an advective timescale, whereas a purely diffusive description could exhibit a different timescale dependence on mixed layer depth. This non-locality could be particularly important when the mixed layer is very deep since stronger convective plumes will tend to transport properties over larger distances by advection.

Chapter 6

Dynamics of turbulent starting plumes

The material contained in this chapter has been published in *Journal of Fluid Mechanics*, under the title 'On the dynamics of starting plumes' (Bhamidipati and Woods, 2017).

6.1 Introduction

The study of turbulent plumes in uniform and stratified ambient has been of interest for many decades (Morton et al., 1956; Woods, 2010). In this chapter, we study the transient nature of buoyant plumes, following the work of Morton et al. (1956) and Turner (1962). Morton et al. (1956) showed that the rate of entrainment of ambient fluid into the plume at a given height is proportional to the characteristic plume velocity at that height, and subsequently developed a series of self-similar solutions based on this assumption. Turner (1962) explored the transient nature of plumes with an experimental investigation of the initial stages of formation of a turbulent buoyant plume. They found that a plume head develops ahead of the steady plume, and a key observation of their work was that the plume head rises at a speed that is approximately 0.6 times the characteristic velocity of the following steady plume.

Some studies have proposed theoretical models for the dynamics of the plume head building on the vortex ring theory for a discrete buoyant thermal proposed by Turner (1957) (Middleton, 1975; Scase et al., 2009; Turner, 1962). However, there still remains some uncertainty about the internal dynamics of

the plume head (Scase et al., 2009). The purpose of this chapter is to reassess the dynamics of a starting plume with a series of new experiments, exploring the balance of mass, momentum and buoyancy between the following steady plume and the plume head. Besides giving more insight into the dynamics of starting plumes, these experiments may provide some new insights into the class of problems in which the source buoyancy flux of an established plume is rapidly increased from one value to another. In this case, it is likely that a plume head type structure, akin to the starting plume, may develop between the original and new plume (Scase et al., 2009, 2006).

In §6.2, we begin by describing our experimental setup, and in §6.3, we present the results from a series of new laboratory experiments of starting plumes, which complement previously published data. In §6.4, we present our observations from experiments in which a pulse of dye is injected into the starting plume to visualise the interaction between the plume head and the following steady plume. In §6.5, we use conservation laws to constrain the fraction of source buoyancy which accumulates in the head. We find that the associated buoyancy force plus the momentum flux supplied by the following plume exceed the rate of change of momentum of the starting plume. We interpret this imbalance as evidence of a drag force associated with the displacement of ambient fluid originally ahead of the starting plume. In §6.6, we explore the implications of our model for the dynamics of a starting plume rising in a stratified ambient. Finally, we present our conclusions and indicate directions for future work in §6.7.

6.2 Experimental setup

A series of six experiments were carried out in a tank of dimensions 0.8 m $\times$ 0.6 m $\times$ 0.6 m, initially filled with fresh water. Salt water plumes of source salinity, s_o, varying between $2.5 - 10$ wt.% were supplied through a nozzle of diameter 0.001 m placed at the top of the tank. A peristaltic pump was calibrated to supply plume fluid to the nozzle at a constant volume flow rate of 1.33 cc/s. The plumes have a source Reynolds number of $\mathcal{O}(10^3)$, and become fully turbulent within $1 - 2$ cm from the source. The plume fluid was dyed in order to distinguish it from the fluid in the tank, and the tank was back-lit by an electroluminescent light sheet (W&Co LED panel 0.8 m $\times$ 0.4 m). The experiments were carried out in an otherwise dark room, and each experiment

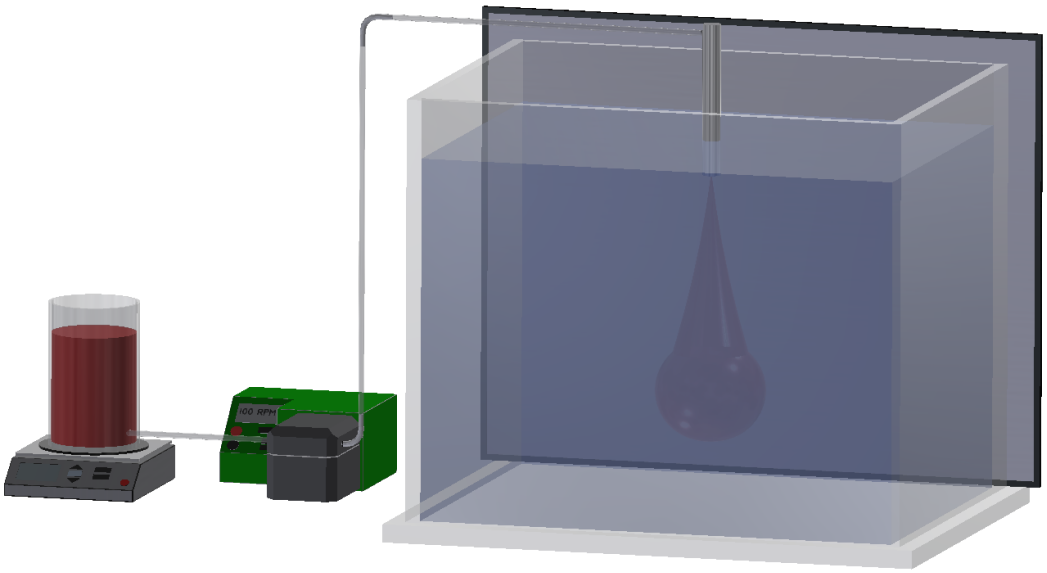

Figure 6.1 The typical experimental setup consists of a tank of dimensions 0.8 m × 0.6 m × 0.6 m, initially filled with fresh water, a peristaltic pump to pump in dyed salty water from a nozzle placed at the top of the tank, and an electroluminescent light sheet to visualise the experiments.

was recorded by video at 30 frames per second. Figure 6.1 shows a typical setup of our experiments.

6.3 Velocity of the plume head

First a series of experiments were carried out in order to measure velocity of the front of the plume and the average shape of the plume head. We define the edge of the plume head as the point where the intensity of the dye, integrated through the plume, drops to 3% of the maximum dye intensity at the source. For smaller values of dye intensity, the background noise becomes as significant as the signal. Using a larger threshold of 4% leads to a reduction in the radius of the head by less than 8%.

From dimensional analysis we expect that for a plume with a source buoyancy flux πB_o, the velocity of the leading edge of the plume, u_f, will scale as $B_o^{1/3} z_f^{-1/3}$, where z_f is the position of the leading edge of the plume head.

$$u_f = \xi_f {B_o}^{\frac{1}{3}} {z_f}^{-\frac{1}{3}} \tag{6.1}$$

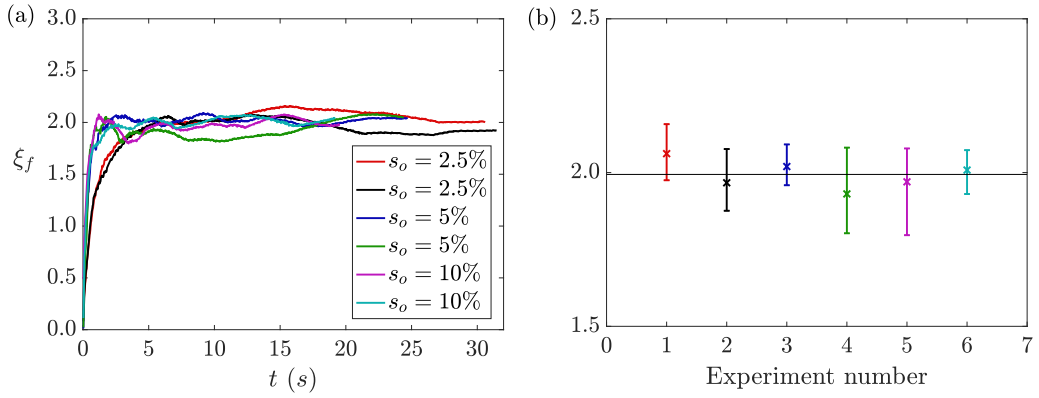

Figure 6.2 (a) Variation of the non-dimensional velocity, ξ_f, with time, t, in each of the six experiments. The legend shows the source salinity s_o associated with each experiment. The average value of ξ_f across each experiment and the corresponding error bars are represented in (b), retaining the same colour scheme as in (a). The horizontal black line in (b) indicates the mean value of ξ_f across the six experiments.

Here ξ_f is the non-dimensional velocity obtained by integrating equation (6.1), with $u_f = \mathrm{d}z_f/\mathrm{d}t$, and is given by

$$\xi_f = \frac{z_f^{\frac{4}{3}}}{\frac{4}{3}B_o^{\frac{1}{3}}(t + t_o)}. \tag{6.2}$$

The constant t_o relates to the time taken by the plume to develop a plume head after issuing from the source. Figure 6.2(a) illustrates the variation of ξ_f, using measured values of z_f at each time t, with different curves corresponding to each of the six experiments. We observe that the data collapses to a constant value after an initial adjustment above the source. We estimate the value of t_o for each experiment to optimise the asymptote of ξ_f to a constant value, and find that the time taken to adjust is in the range $0.5 - 2.5$ s, which is considerably shorter than the $20 - 30$ s typical of the experiments.

Figure 6.2(b) shows the average value of ξ_f for each experiment, with the colours corresponding to the legend in figure 6.2(a). The error bars in this figure represent the variation of ξ_f in each experiment after an initial adjustment time, t_o (see figure 6.2(a)). The mean value of ξ_f across experiments, indicated by the black line in figure 6.2(b), was found to be 1.99 ± 0.06.

The classical plume theory of Morton et al. (1956) describes the equations for the averaged top-hat velocity, $u_p(z)$, radius $b(z)$, and reduced gravity, $g'_p(z)$,

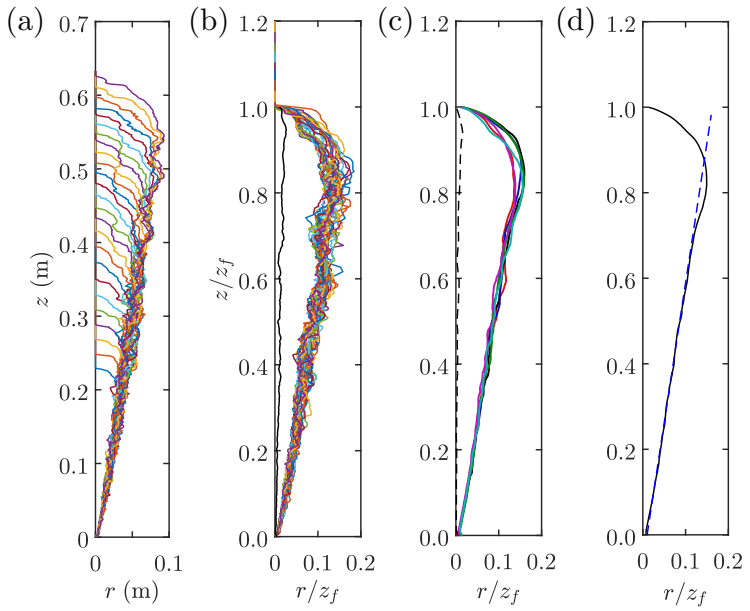

Figure 6.3 Variation of (a) the radius of the plume, r, as a function of height, z, and (b) the rescaled radius, r/z_f, as a function of rescaled height, z/z_f, of the starting plume. Data shows 25 frames, recorded with a time interval of 1 s between frames. In (b), the black curve represents the standard deviation of the rescaled data in (b), calculated for the experiment with $s_o = 2.5\%$ and $Q_o = 1.33$ cc/s. (c) Time average of the rescaled radius of the starting plume as a function of rescaled height for each of the six experiments, with the same colour scheme as in figure 6.2. The black dashed curve in (c) represents the standard deviation of the profiles in (c) relative to the mean profile from the six experiments, which is shown in (d). The blue dashed line in (d) represents the best-fit for the radius of the steady plume which follows the plume head.

as a function of height, z, for an established steady plume in an unstratified ambient.

$$\frac{\mathrm{d}(u_p b^2)}{\mathrm{d}z} = 2\alpha u_p b, \tag{6.3a}$$

$$\frac{\mathrm{d}({u_p}^2 b^2)}{\mathrm{d}z} = b^2 {g'_p}^2, \tag{6.3b}$$

$$\frac{\mathrm{d}(u_p b^2 g'_p)}{\mathrm{d}z} = 0, \tag{6.3c}$$

where α is the entrainment coefficient which has a value of 0.13 ± 0.01 (Morton et al., 1956). Solving the steady state plume equations given by equations (6.3a–c) gives the average top-hat velocity within the plume,

$$u_p = \frac{5}{6\alpha}\left(\frac{9\alpha B_o}{10}\right)^{\frac{1}{3}} z^{-\frac{1}{3}} = \xi_p {B_o}^{\frac{1}{3}} z^{-\frac{1}{3}}. \tag{6.4}$$

Based on our experimental data of the height of rise of the plume as a function of time, the ratio of the velocity of the front of the plume head (equation (6.1)) to the velocity of a steady plume at that height (equation (6.4)) (ξ_f/ξ_p) lies in the range 0.63 ± 0.04, which is consistent with the results of Turner (1962) (0.61 ± 0.05) and Scase et al. (2009) (0.65).

Figure 6.3(a) illustrates the radius of the plume as a function of height in the plume at a series of times. By scaling the height and radius of the plume at a given time t by the position of the leading front of the plume at that time, $z_f(t)$, we find that the starting plume can be mapped to a universal shape, suggesting that both the plume head and plume are self-similar. This is shown in figure 6.3(b). In this figure, the black curve represents the standard deviation of the plume radius for the 25 frames shown. The relatively large standard deviation is a result of turbulent fluctuations in the position of the edge of the plume with time.

The plume profiles obtained in each experiment were time-averaged, and the mean profiles for the six experiments are shown in figure 6.3(c). In this figure, the black dashed curve represents the standard deviation of these averaged experimental profiles. Figure 6.3(d) illustrates the average shape for the six experiments. The radius of the steady plume behind the plume head, shown in figure 6.3(d), increases linearly with height, as shown by the dashed line,

$r_f = \lambda(z + z_o)$, where $\lambda = 0.15$ and z_o is the virtual origin. The intercept on the line $r_f = 0$ occurs at $z \approx -4.5 \pm 1.5$ cm suggesting the virtual origin has value $z_o \approx 4.5$ cm. This value is small compared to the distance of order $60 - 70$ cm travelled by the plumes.

The linear increase in plume radius with height shown in figure 6.3(d) is observed to be valid only below the height $z = 0.71 z_f$, after which the difference between the best-fit straight line modelling the radius, r_f, and the average of the experimental data, r, is observed to increase more rapidly (figure 6.3(d)). We define this point to be the lower boundary of the plume head, z_b. By comparing the data with the model linear increase in radius with height, we find that in all experiments, the height of the lower boundary remains nearly constant, $z_b = (0.70 \pm 0.02) z_f$. Given the near constant ratio between z_b and z_f and the self-similar shape of the plume, we estimate the velocity of the lower boundary of the plume head,

$$u_b = \left(\frac{z_b}{z_f}\right) u_f = \xi_b {B_o}^{\frac{1}{3}} {z_b}^{-\frac{1}{3}}. \tag{6.5}$$

From our experimental data, this suggests that the ratio of the velocity of the lower boundary of the plume head to the velocity of a steady plume at that height (ξ_b/ξ_p) is 0.39 ± 0.04. This range is consistent with Turner's (1962) estimate of 0.38 and the maximum theoretical prediction of 0.42 given by Delichatsios (1979).

6.4 Interaction between the plume head and the following steady plume

In order to help understand the interaction between the plume and plume head and visualise the path followed by individual fluid elements in the plume, we inject pulses of dye into the starting plume. We inject a small amount of dye (less than 0.2 cc) through the nozzle using a syringe at a volume flux of 0.2 cc/s so that the volume flux of dye injected does not produce a significant change in the volume flux exiting the nozzle (source volume flux at the nozzle is $Q_o = 1.33$ cc/s). In experiment A, only one pulse of dye was injected at time $t \approx 2.5$ s to visualise the propagation of dye through the plume. Figure 6.4 illustrates the evolution of the pulse of dye in the plume. In this figure, the

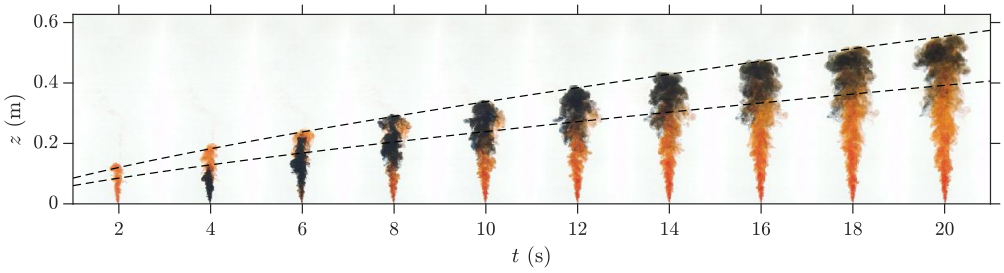

Figure 6.4 Experiment A. Propagation of a pulse of dye through the plume and accumulation of dye in the plume head. The dashed curves indicate the positions of the front (z_f) and back (z_b) of the plume head, where $z_b(t) = 0.71 z_f(t)$. In this experiment, the salinity of the fluid at the source is $s_o = 5\%$ and the source volume flux is $Q_o = 1.33$ cc/s. The time interval between frames is 2 s.

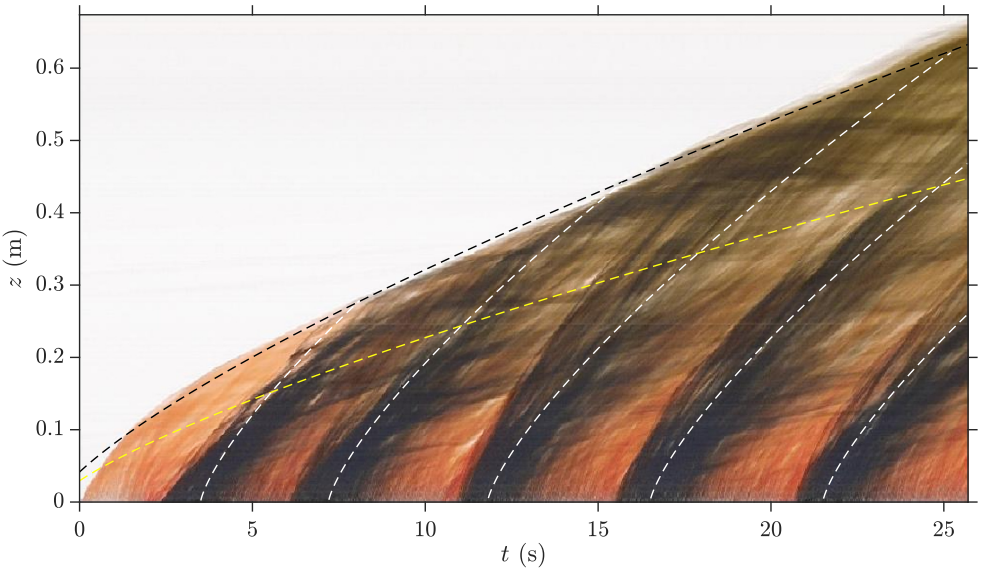

Figure 6.5 Experiment B. Time series of the vertical centre-line of the plume. The dashed curves show the $t^{\frac{3}{4}}$ characteristics for the position of the front (black) and back (yellow) of the head, and of the pulses of dye (white). In this experiment, the salinity of the fluid at the source is $s_o = 5\%$ and the source volume flux is $Q_o = 1.33$ cc/s.

black dashed curves represent the positions of the front and back of the plume head as defined by the relation $z_b(t) = 0.71 z_f(t)$. These curves are given by

$$z_f{}^{\frac{4}{3}} = \frac{4}{3}\xi_f B_o{}^{\frac{1}{3}}(t + t_o), \tag{6.6a}$$

$$z_b{}^{\frac{4}{3}} = \frac{4}{3}\xi_b B_o{}^{\frac{1}{3}}(t + t_o), \tag{6.6b}$$

consistent with equations (6.1) and (6.5).

The series of photographs in figure 6.4 show (i) the accumulation of the pulse of dye within the region defined by $z_b < z < z_f$, and (ii) the irregular turbulent structure of the plume head which is illustrated by the motion of the packets of dyed fluid as they approach the leading edge of the plume.

In experiment B, we add five pulses of dye to the source fluid at five successive times during the experiment in order to visualise the motion of the plume fluid as it rises towards the leading edge of the plume and then mixes into the plume head. In figure 6.5, we show a time-series of a vertical line of pixels passing through the plume source. This figure illustrates the successive waves of dyed fluid which migrate to the front of the flow, where they accumulate and mix in the plume head. This figure shows two sets of curves. First, the dashed black curve follows the leading edge of the plume head, and the dashed yellow curve follows the back of the plume head, as described by equations (6.6a–b). Second, a series of dashed curves $z_i(t)$ are shown, each of which follows the ascent of one of the successive streaks of dye. Based on dimensional analysis, these curves have the form

$$z_i{}^{4/3} = \frac{4}{3}\xi_s B_o{}^{1/3}(t - t_i), \tag{6.7}$$

where t_i is the time of release of the i-th pulse of dye. Tracking the pulses of dye that reach the front of the plume gives an approximate estimate for ξ_s, which has a value of approximately 3.82 ± 0.7. The range of values obtained for ξ_s are a result of the different speeds of each of the the individual pulse of dye, which is in part to the effects of dispersion (cf. Rocco and Woods (2015)). It is important to note that the estimate for ξ_s is larger than the estimates of ξ_f (1.99) and ξ_b (1.25) and shows that plume head is continually supplied fluid

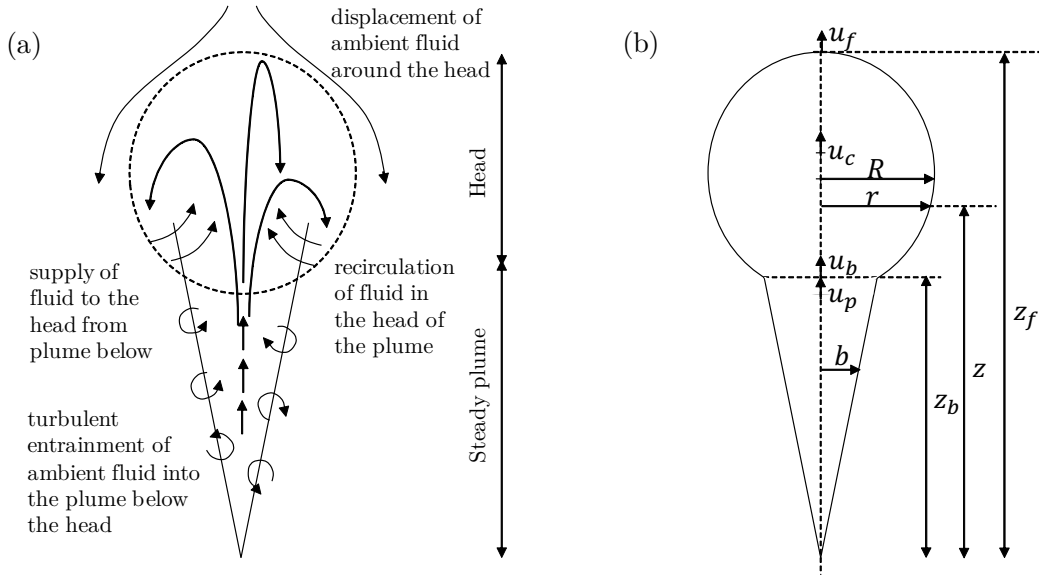

Figure 6.6 (a) An illustration of the motion of fluid within the starting plume and the motion of ambient fluid around the plume head. The motion of fluid within the plume head shown is in the frame of reference of the plume head. (b) A schematic illustrating various dimensions and velocities.

by the steady plume which develops behind the plume head, as is clear from the mean path followed by the dye in figures 6.4 and 6.5.

6.5 Modelling the plume head

We now build a model of the mass, momentum and buoyancy conservation in the plume head in order to estimate the mixing of ambient fluid directly into the head, and also to test the momentum balance of the head. The model presented here describes an ensemble average of the flow, averaged over several realisations of the flow, so that fluctuations associated with the detailed distribution of individual eddies in the flow are averaged. The plume behind the plume head is modelled as being steady, while the plume head slowly evolves in time and space. We define the plume head to correspond to the region $z_b < z < z_f$ as defined by figure 6.3(d). Figure 6.6(a) captures the observations from figures 6.4 and 6.5 in a schematic, and figure 6.6(b) illustrates the shape of the starting plume and the various parameters involved in the modelling of the plume head.

6.5.1 Conservation of volume

The volume of the plume head V_c is found by evaluating the integral

$$V_c = \int_{z_b}^{z_f} \pi r^2 \mathrm{d}z, \tag{6.8}$$

where $r = r(z)$ is the radius of the starting plume as obtained from our experiments. This is given by the shape profiles shown in figure 6.3. Similarly, we define the vertical momentum of the plume head as

$$M_c = \int_{z_b}^{z_f} \pi r^2 u \mathrm{d}z, \tag{6.9}$$

where u is the horizontally averaged vertical velocity at height z in the plume head. This is given by $u = u_f(z/z_f)^{-1/3}$, assuming that the shape of the plume head remains similar at all times. The velocity of the centre of mass of the plume head, $u_c = \mathrm{d}z_c/\mathrm{d}t$, is obtained from the equations for momentum and volume of the plume head, so that $u_c = M_c/V_c$. Using experimental data, we estimate the position of the centre of mass of the plume head, z_c, as a function of the position of the leading edge of the plume head, z_f, and find that $z_c = (0.83 \pm 0.01)z_f$.

Since the plume head is not perfectly spherical, we define a shape factor, Ω, for the plume head as

$$\Omega = \frac{V_c}{(z_c - z_b)R^2}, \tag{6.10}$$

where R is the maximum radius of the plume head (see figure 6.6(b)). The average value of Ω was found to be 5.41, which is a larger value than the shape factor of an equivalent ellipsoid ($= 4\pi/3 \approx 4.19$). As a result, the volume of the plume head as defined in equation (6.8), and using the 3% dye threshold, which is the limit of our experimental method, was found to be approximately 23% larger than the volume estimates of Turner (1962) and Scase et al. (2009), where the plume head was assumed to have a spherical shape.

Figures 6.4 and 6.5 illustrated that the plume head is supplied with fluid by the following steady plume. We can estimate the volume flux of fluid supplied by the steady plume to the plume head by solving the steady plume equations (6.3a–c) of Morton et al. (1956) for the radius and the velocity of the following steady plume. The flux entering the plume head, evaluated at $z = z_b$, is given by $Q_p = \pi b^2(u_p - u_b)|_{z=z_b}$, where the expression $(u_p - u_b)$ accounts for the fact

that the back of the plume head is advancing with velocity u_b. The equation for conservation of volume of the plume head is then given by

$$Q_c \equiv \frac{\mathrm{d}V_c}{\mathrm{d}t} = Q_p + \epsilon V_c^{\frac{2}{3}} u_c, \tag{6.11}$$

where the second term on the right-hand side gives the volume flux ambient fluid entrained into the plume head.

Solving equation (6.11) using the experimental estimates of V_c, Q_p, u_c and z_b, suggests that the ratio of the volume flux supplied by the following steady plume, Q_p, to the rate of change of volume of the plume head, $\mathrm{d}V_c/\mathrm{d}t$, is approximately 0.88 ± 0.06. This implies that the time-averaged volume flux entrained directly into the plume head is small compared to the flux supplied from the steady plume. The range of values of Q_p/Q_c is consistent with the error in our measurement of the volume of the plume head, V_c, and arises in part due to the turbulent fluctuations of the flow and in part due to the uncertainty in the precise value of the entrainment coefficient of the steady plume, α.

Based on our experimental data, we estimate that the entrainment coefficient for the plume head, ϵ, is approximately 0.14 ± 0.08. If the plume head were to entrain over its entire surface area, $S_c = \int_{z_b}^{z_f} 2\pi r \mathrm{d}z$, then the equivalent entrainment coefficient per unit surface area would be 0.04 ± 0.02. This value, which is smaller than the entrainment into a steady plume, is consistent with the entrainment coefficient for the plume head estimated by Scase et al. (2009) $(0.04 - 0.05)$. These estimates suggest that the increase in the volume of the plume head is mainly due to the supply of the fluid from the following steady plume, and that the volume flux of fluid entrained directly into the plume head is only a small fraction of the volume flux of the plume head.

6.5.2 Conservation of buoyancy

The conservation of buoyancy for the plume head is given in terms of the flux of buoyancy entering the head from the steady plume. Since the buoyancy flux in steady plume is defined as $\pi g_p' b^2 u_p$ in the top-hat model of Morton et al. (1956), and since the rear of the plume head advances with speed u_b, the flux

entering the plume head is given by $\pi b^2(u_p - u_b)g'_p = Q_p g'_p$. This leads to the equation for the conservation of buoyancy,

$$\frac{\mathrm{d}g'_c V_c}{\mathrm{d}t} = Q_p g'_p|_{z=z_b}. \tag{6.12}$$

Here g'_c is the mean reduced gravity of the plume head averaged throughout the plume head, and g'_p is the mean reduced gravity of the following steady plume at height z, averaged across a horizontal surface at height z. We obtain $g'_p(z)$ by solving the steady-state plume equations (Morton et al., 1956),

$$g'_p(z) = \frac{5B_o}{6\alpha}\left(\frac{9\alpha B_o}{10}\right)^{-\frac{1}{3}}(z + z_o)^{-\frac{5}{3}}, \tag{6.13}$$

where z_o is the virtual origin of the plume. The total buoyancy in the steady plume in the region $0 < z < z_b(t)$ is given by

$$\pi\int_0^{z_b} g'_p(z)b(z)^2\mathrm{d}z = \left(\frac{3\pi}{4}\right)\left(\frac{6\alpha}{5}\right)\left(\frac{9\alpha}{10}\right)^{-\frac{1}{3}} {B_o}^{\frac{2}{3}}\left[(z_b + z_o)^{\frac{4}{3}} - {z_o}^{\frac{4}{3}}\right]. \tag{6.14}$$

In the limit $z_o << z_b$, appropriate for our experiments with $z_o \approx 4.5$ cm and $z_b \approx 60 - 70$ cm, we may approximate the right-hand side of equation (6.14) by the expression

$$\left(\frac{3\pi}{4}\right)\left(\frac{6\alpha}{5}\right)\left(\frac{9\alpha}{10}\right)^{-\frac{1}{3}} {B_o}^{\frac{2}{3}} {z_b}^{\frac{4}{3}} = \left(\frac{\xi_b}{\xi_p}\right)\pi B_o t, \tag{6.15}$$

where $\pi B_o t$ is the total buoyancy supplied from the source up to a time t, and ξ_p and ξ_b are defined in equations (6.4) and (6.5) respectively. Here $(\xi_b/\xi_p) = 0.39 \pm 0.04$ (see §6.3). The remainder of the buoyancy accumulates in the plume head and is given by

$$\left(1 - \frac{\xi_b}{\xi_p}\right)\pi B_o t = (0.61 \pm 0.04)\pi B_o t. \tag{6.16}$$

6.5.3 Conservation of momentum

We propose that the equation for conservation of momentum of the plume head has the form

$$(1 + A)\frac{\mathrm{d}M_c}{\mathrm{d}t} = Q_p u_p|_{z=z_b} + g'_c V_c - C_d u_c^2(\pi R^2), \tag{6.17}$$

where A is the added-mass of the plume head, and the first two terms on the right-hand side denote the momentum flux supplied to the plume head by the fluid entering from the following steady plume and the buoyancy force on the head. We have also included a drag force, with drag coefficient C_d, which is similar in effect to form drag on a moving body. The added-mass, A, arises due to the acceleration of ambient fluid around the head, thus contributing an increased force on the plume head (Ohl et al., 2003).

We note that this model differs from some of the earlier literature in which the plume head has been modelled as a spherical vortex (Scase et al., 2009; Turner, 1962). Our observations of the structure and motion of fluid in the plume head (figures 6.4 and 6.5) suggest that the flow does not develop a coherent vortex ring type structure. Instead, we observe irregular motion as turbulent pulses of buoyant fluid supplied to the plume head reach the plume front and spread radially, with successive parcels spreading in different directions. This approach for modelling the plume head follows from the work of Scorer (1997) who proposed a similar momentum conservation equation for a discrete thermal, although they did not include the turbulent drag term since they did not measure the shape of the thermal independently of the momentum equation.

Using the estimated similarity coefficients from equations (6.11) and (6.12), together with the modified momentum equation for the plume head given by equation (6.17), we estimate that the drag coefficient, C_d, is approximately 4.2 ± 1.4. We find that the range of values of C_d correspond to the uncertainty in our estimate of ϵ. Hence we establish a relationship between the entrainment coefficient, ϵ, and drag coefficient, C_d, of the plume head by combining the coefficients from equations (6.11) and (6.17) so that

$$C_d = (6.0 \pm 0.3) - (11.8 \pm 1.2)\epsilon. \tag{6.18}$$

In doing these calculations, the added-mass of the plume head was assumed to be equal to the added-mass of a sphere, $A = 0.5$, consistent with Scorer (1997) and Ohl et al. (2003).

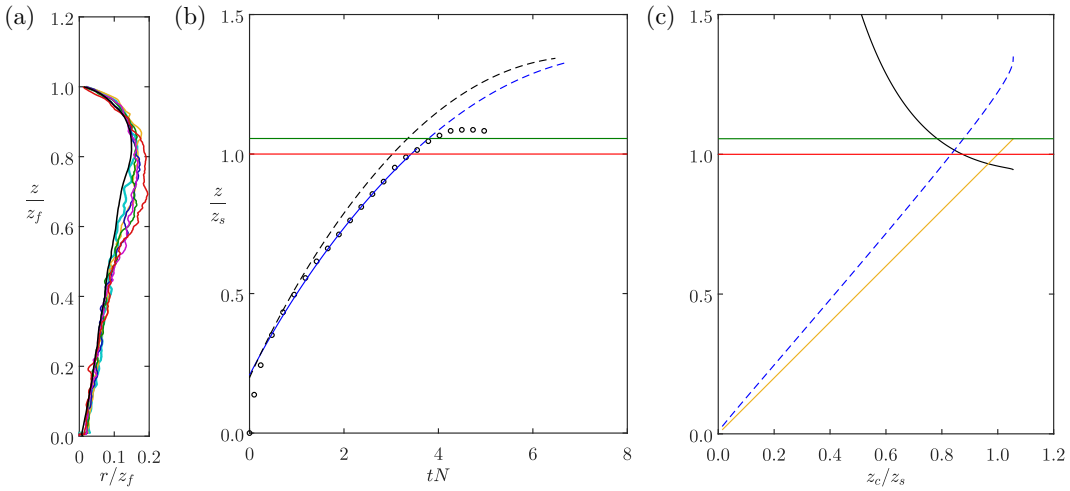

Figure 6.7 (a) Rescaled radius, r/z_f, as a function of the rescaled height, z/z_f, in a linearly stratified ambient. The figure shows the radius averaged across five experiments when the plume is at different fractions of the maximum top height, z_T ($z_f/z_T = 0.5 - 1.0$). The red profile shows the rescaled radius when the plume reaches its top height ($z_f = z_T$). The black profile shows the equivalent profile in an unstratified ambient (see figure 6.3(d)). In the five experiments, the ambient stratification is $N^2 = 0.35$ and the source volume flux is $Q = 1.01$ cc/s, and the source salinity in each of the five experiments is $s_o = 10\%, 12\%, 13\%, 14\%, 15\%$. (b) Plot of dimensionless height of rise, z/z_s, versus dimensionless time, tN, where z_s is the maximum height of the steady plume in a stratified ambient. The figure illustrates the height of rise as predicted by our model (blue dotted curve) and the model proposed by Turner (1962) using the equivalent top-hat coefficients estimated by Scase et al. (2009) (black dotted curve). The black circles indicate our experimental data. (c) z/z_s versus z_c/z_s, where z_c is the position of the centre of the plume head. The yellow line shows the rescaled position of the centre of the plume head, $z = z_c$, and the blue dotted line shows the position of the top of the plume head. The black curve is the instantaneous neutral height of the plume head (black curve), which is the height, z, at which the density of the plume head equals the density of the ambient. The horizontal lines in panels (b) and (c) show the maximum height of the continuing steady plume (red line) and the maximum height of rise of the centre of the plume head (green line) as predicted by our model.

6.6 The starting plume in a stratified ambient

In this section, we describe how a starting plume rises through a linearly stratified ambient, characterised by the Brunt–Väisälä frequency, N, where $N^2 = -\frac{g}{\rho_o}\frac{\mathrm{d}\rho_a}{\mathrm{d}z}$, in which ρ_a is the density of the ambient at height z and ρ_o is a reference density.

We have carried out a series of experiments in which we set up a linear stratification in the experimental tank with $N^2 = 0.35$ s^{-2}. We then explored the ascent of series of starting plumes with source volume flux $Q_o = 1.01$ cc/s and salinity $s_o = 10, 12, 13, 14, 15\%$. In figure 6.7(a), we illustrate the variation of the rescaled radius (r/z_f) as a function of the rescaled height (z/z_f) at the different times when the plume height z_f was a fraction 0.5 (cyan), 0.6 (yellow), 0.7 (blue), 0.8 (green), 0.9 (purple), and 1.0 (red) of the maximum height of rise of the starting plume z_T. In each case, we have averaged the profile over the five experiments. The figure shows that as the plume approaches the maximum height, the plume radius begins to increase as it slows down and intrudes laterally. For reference, the black profile represents the equivalent profile of the plume in an unstratified environment (figure 6.3(d)). In figure 6.7(b), we illustrate the average of the experimental data for the height of the top of the plume head as a function of dimensionless time, tN (black circles).

To include stratification in the model of a starting plume, we modify the buoyancy conservation equation (6.12) to the form (cf. Morton et al. (1956))

$$\frac{\mathrm{d}g'_cV_c}{\mathrm{d}t} = Q_pg'_p|_{z=z_b} - N^2V_cu_c. \tag{6.19}$$

We now solve equations (6.11), (6.17), and (6.19), for mass, momentum, and buoyancy conservation of the plume head, coupled with the solutions of the steady plume equations in a stratified environment (cf. Morton et al. (1956)) to calculate the supply of volume, momentum, and buoyancy into the plume head. To complete our model, we need to specify the shape of the plume head in order to relate the position of the base of the head, z_b, to the position of the centre of mass of the head, z_c, and to estimate the radius of the head, R, according to equation (6.10).

Below the maximum height of rise, before the shape of the plume is influenced by the stratification (figure 6.7(a)), we might expect that the relationships between z_b, z_c, z_f, and Ω for the unstratified case ($z_b/z_f = 0.71, z_c/z_f = 0.83, \Omega = 5.41$) provide a reasonable approximation. In these calculations, we

also need to specify the value of the drag coefficient, C_d, and the entrainment coefficient, ϵ, which are constrained by the relation $C_d = (6.0 \pm 0.3) - (11.8 \pm 1.2)\epsilon$ from our experiments in an unstratified ambient. We find that the error between our model and the experimental data is less than 5% for the range of values of C_d given by the relation (6.18).

The estimate of the height of rise from our model is shown in figure 6.7(b) (blue curve), where the mean value of $\epsilon (= 0.14)$ was used to estimate the value of the drag coefficient, C_d. Figure 6.7(b) also shows the estimates of the height of rise of the starting plume using the vortex ring model proposed by Turner (1962) and Scase et al. (2009) (black dashed curve). The parameters used in this model were taken from those given by Scase et al. (2009). We used the parameters from Scase et al. (2009), since in the original work of Turner (1962), the speed of the front of the plume head was assumed to equal a fraction 0.6 of the maximum centre-line speed of the steady plume rather than a fraction 0.6 of the top-hat speed as used by Scase et al. (2009), and which is consistent with our experimental results. Equation (6.19) was used to describe the conservation of buoyancy. The figure shows that the new model predicts the height of rise somewhat more accurately until the plume reaches the maximum height of the steady plume where the shape of the plume head and its dynamics change as a result of the stratification (figure 6.7(a)).

Figure 6.7(c) illustrates the variation of the height at which the plume head would be neutrally buoyant (black curve) as a function of the height of the centre of the plume head, as well as the height of the leading edge of the plume (blue dashed curve) and centre of the plume head (yellow curve). The figure indicates that the neutral buoyancy height of the plume head, which occurs where the yellow and black curves meet, is very similar to the maximum height of the steady plume (red horizontal line). The maximum overshoot of the centre of the plume head above this height (green horizontal line), as predicted by the model, is comparable to the experimental measurement of the maximum height of rise of the plume head as shown in figure 6.7(b). However, given the distortion of the shape of the plume head near the maximum height of rise (figure 6.7(a)), we do not expect the model prediction for the height of the leading edge of the plume head to follow accurately the motion of the leading front of the plume head beyond this height.

6.7 Summary

In this chapter we have illustrated some new experiments to describe the mixing and interaction between the plume head, the following steady plume, and the ambient. We found that the buoyancy force on the plume head combined with the momentum flux supplied to the plume head from the following steady plume exceed the rate of change of momentum of the plume head. We propose that a turbulent drag on the plume head develops which accounts for this difference. We have estimated that the drag coefficient is given by $C_d = 4.2 \pm 1.4$, with the range of values corresponding to the uncertainty in the estimate of the entrainment coefficient $\epsilon = 0.14 \pm 0.08$. The range of values of the entrainment coefficient suggest that the plume head entrains only a small fraction of its volume from the ambient, with the dominant influx of fluid supplied by the following steady plume. We also found that a fraction 0.61 ± 0.04 of the total buoyancy supplied by the source lies within the plume head, so that the plume head is more buoyant than the developing steady plume immediately behind at $z = z_b$.

In a stratified ambient the assumption that the plume head retains the same shape as in the unstratified case allows an initial estimate for the height of rise with time, which compares well with experimental data up to the point at which the plume head reaches the maximum height of rise of the ensuing steady plume. It would be of interest to explore the evolution of the plume head beyond the maximum height perhaps with an investigation into the dynamics of a negatively buoyant forced thermal in a uniform and stratified environment, to understand the dynamics and the deformation of the plume head near its maximum height.

When a steady flux of buoyancy, generating a steady turbulent plume, is suddenly increased to a substantially larger value, then a mixed zone of fluid may develop and grow in the transition region, somewhat akin to the starting plume. It would be of interest to develop the experimental modelling presented herein to estimate the drag and entrainment coefficients associated with such transition zones in order to build a model of their evolution.

Chapter 7

Conclusions and future work

In this thesis, we presented some simplified models of dispersion and mixing in geophysical flows. This chapter summarises our findings and indicates directions for future work.

In chapters 2 and 3, we analysed the dispersion of a passive tracer in a pressure-driven flow through a confined porous medium consisting of a random assemblage of lenses. We show that owing to the boundaries, a shear develops in the mean flow along the layer. This leads to a quantitatively different long-time behaviour of the tracer as it spreads out in the flow. Our analysis illustrates that at early times, the spreading of a cloud of tracer or a plume of pollutants in a porous rock is controlled by the effect of small-scale dispersion associated with the random positioning of the lenses across the channel. In this regime the along-flow length scale of the tracer grows as $\sqrt{x}$, where x is the horizontal position of the centre of mass of the tracer. At late times, the spreading is controlled by the mean shear, which arises as a result of the difference in travel times along different streamlines in the channel, and which leads to a spreading that grows linearly with distance. This is consistent with many field observations of the dispersion of tracer in porous rocks, which suggest that the standard deviation of the tracer increases approximately linearly with distance downstream (Gelhar et al., 1992).

In chapter 4, we explored the shear which arises as a result of (i) a tilted interface between two sections of isotropic rock, and (ii) a vertical interface between two sections of anisotropic rock. We explored the competition between these effects, showing how they may combine constructively to produce a larger shear, or may negate one another, reducing or reversing the sign of the shear,

depending on the angle of the interface, the degree of anisotropy and the change in effective downstream permeability across the interface. This analysis illustrates the key result that in such geological formations the flow can exhibit a strong shear and so using simplified 'effective permeability' values in the direction of the flow for simulation of the transport of tracer, or of a fluid-fluid interface, misses out the effects of shear, which is central for predicting the dispersion and stretching of the flow within this type of bounded porous layer.

To explore the effect of shear further, it would be of interest to explore the shear produced by a variety of more complex types of natural rock heterogeneity, and also to extend the analysis to consider three dimensional patterns of heterogeneity. For example, in finite channels, such as those formed by braided streams, lenses may be localised in both the vertical and lateral directions. The finite channel width and depth will again lead to both a mean shear and a large-scale dispersion due to the random positioning of the lenses.

As well as being important for modelling tracer dispersal, the shear driven spreading of a flow front may be very important in industrial situations in which pulses of chemicals are added to the flow to change the properties of the formation or the injected fluid. Often these chemicals are added some time after the start of operations, and they may be used with time-delay encapsulation technology, so that the chemicals can migrate a given distance into a formation before being activated. The development of a shear as well as the dispersive spreading will lead to distortion of the chemical front, and could have an important impact on its effectiveness. Exploring the effect of changes in flow properties associated with such additives would be an important extension of this work.

In chapter 5, we studied the 2D turbulent mixing of a passive scalar in the ocean mixed layer. As an example, we examined a steady-state convective mixed layer in which the boundary conditions are chosen so that the system reaches a dynamical equilibrium. In this idealised case, we parameterised the horizontally and temporally averaged fluxes as a functional of the horizontally and temporally averaged property gradients. Here, $\langle w'c' \rangle = -\int \mathrm{d}z' \mathcal{K}(z|z') \partial \langle c \rangle / \partial z'$, where $\mathcal{K}(z|z')$ is the eddy diffusivity kernel which describes the vertical transport by eddies at any vertical location z. The full kernel $\mathcal{K}(z|z')$ is computed by adding passive scalars to a buoyancy-driven flow field in a 2D DNS of the ocean surface layer. Although several non-local parameterisations have been defined in literature, the analysis presented in this chapter does not use any closure

assumptions, and the functional form of the eddy diffusivity kernel is based on an unapproximated representation of the chosen physics.

One further development to this study would be to study seasonal variations of the mixed layer depth by adding a time-varying surface insolation to see if the quasi-steady approach is adequate in describing time-varying fluxes. Although our model is missing important processes for the surface layer of the ocean (e.g. winds), we have established a framework for parameterising fluxes using a functional form of eddy diffusivity which is based on proper representation of the physics for different flow problems. While the particular example presented here is limited, it illustrates the basic principle of using a functional approach and points to a way to define those functionals for other problems in turbulence concerning the mixing of a passive scalar. We hope that this study further motivates new parameterisations in future works.

In chapter 6, we explored the dynamics of starting plumes by analysis of a series of new small-scale laboratory experiments which illustrated the mixing and dispersion of fluid in a transient turbulent plume. We find that the head of the plume ascends with a speed which is approximately 0.6 times the characteristic speed of the fluid in the following steady plume, in accordance with Turner (1962), and so the fluid released from the source eventually catches the head of the flow. On reaching the top of the plume it recirculates and mixes in the plume head. We estimated that approximately 0.61 ± 0.04 of the total buoyancy released from the source accumulates in the plume head, with the remainder in the following steady plume. Using measurements of the volume of the head, we estimated that a fraction 0.16 ± 0.08 of the volume of the head is entrained directly from the ambient, with the remainder of the fluid in the head being supplied by the following steady plume. These results imply that the buoyancy force exerted on the plume head plus the momentum flux supplied by the following plume exceeds the rate of change of momentum of the plume head even including the added-mass of the plume head. We proposed that the difference is associated with a drag force resulting from the displacement of ambient fluid around the plume head. Using our experimental data, we estimate that the drag coefficient C_d has a value 4.2 ± 1.4, with the range in values associated with the uncertainty in our estimate of entrainment of fluid directly into the plume head.

In a stratified ambient the shape of the plume head is no longer self-similar, but assuming that the plume head retains the same shape as in the unstratified

case allows an initial estimate for the height of rise with time. This compares well with experimental data up to the point at which the plume head reaches the maximum height of rise of the ensuing steady plume. It would be of interest to explore the evolution of the plume head beyond the maximum height, possibly with an investigation into the dynamics of a negatively buoyant forced thermal in a uniform and stratified environment, to understand the dynamics and the deformation of the plume head near its maximum height. When a steady flux of buoyancy, generating a steady turbulent plume, is suddenly increased to a substantially larger value, then a mixed zone of fluid may develop and grow in the transition region, somewhat akin to the starting plume. It would be of interest to develop the experimental modelling presented herein to estimate the drag and entrainment coefficients associated with such transition zones in order to build a model of their evolution.

References

Acreman, D. M. and Jeffery, C. D. (2007). The use of Argo for validation and tuning of mixed layer models. *Ocean Modelling*, 19(1–2):53–69.

Allen, J. R. L. (1963). The classification of cross-stratified units. With notes on their origin. *Sedimentology*, 2(2):93–114.

Bear, J. (1971). *Dynamics of Flow in Porous Media*. Elsevier.

Bear, J. and Cheng, A. H.-D. (2010). *Modeling groundwater flow and contaminant transport*, volume 23. Springer Science & Business Media.

Begg, S. H. and King, P. R. (1985). Modelling the effects of shales on reservoir performance: calculation of effective vertical permeability. In *SPE Reservoir Simulation Symposium*. Society of Petroleum Engineers.

Berkowitz, B., Scher, H., and Silliman, S. E. (2000). Anomalous transport in laboratory-scale, heterogeneous porous media. *Water Resources Research*, 36(1):149–158.

Bhamidipati, N., Souza, A. N., and Flierl, G. R. (2020). Turbulent mixing of a passive scalar in the ocean mixed layer. *Ocean Modelling*, 149:101615.

Bhamidipati, N. and Woods, A. W. (2017). On the dynamics of starting plumes. *Journal of Fluid Mechanics*, 833.

Bhamidipati, N. and Woods, A. W. (2020a). Boundary-induced shear and tracer transport in heterogeneous porous rock. *Journal of Fluid Mechanics*, under review.

Bhamidipati, N. and Woods, A. W. (2020b). Shear generation in composite cross-bedded porous rock. *Journal of Fluid Mechanics*, in press.

Bickle, M. J. (2009). Geological carbon storage. *Nature Geoscience*, 2(12):815.

Burns, K. J., Vasil, G. M., Oishi, J. S., Lecoanet, D., and Brown, B. P. (2019). Dedalus: A flexible framework for numerical simulations with spectral methods. *arXiv e-prints*, page arXiv:1905.10388.

Cala, M. A. and Greenkorn, R. A. (1986). Velocity effects on dispersion in porous media with a single heterogeneity. *Water Resources Research*, 22(6):919–926.

Corbett, P. and Jensen, J. L. (1992). Estimating the mean permeability: how many measurements do you need? *First Break*, 10(3):89–94.

Dagan, G. (1979). Models of groundwater flow in statistically homogeneous porous formations. *Water Resources Research*, 15(1):47–63.

Dagan, G. (1982). Stochastic modeling of groundwater flow by unconditional and conditional probabilities: 1. Conditional simulation and the direct problem. *Water Resources Research*, 18(4).

Dagan, G. (1984). Solute transport in heterogeneous porous formations. *Journal of Fluid Mechanics*, 145.

Dagan, G. and Fiori, A. (2003). Time-dependent transport in heterogeneous formations of bimodal structures: 1. The model. *Water Resources Research*, 39(5).

Dagan, G., Fiori, A., and Janković, I. (2003). Flow and transport in highly heterogeneous formations: 1. Conceptual framework and validity of first-order approximations. *Water Resources Research*, 39(9).

Darcy, H. P. G. (1856). *Les Fontaines publiques de la ville de Dijon. Exposition et application des principes à suivre et des formules à employer dans les questions de distribution d'eau, etc.* V. Dalamont.

Davis, J. M., Lohmann, R. C., Phillips, F. M., Wilson, J. L., and Love, D. W. (1993). Architecture of the Sierra Ladrones formation, central New Mexico: Depositional controls on the permeability correlation structure. *Geological Society of America Bulletin*, 105(8):998–1007.

Delichatsios, M. A. (1979). Time similarity analysis of unsteady buoyant plumes in neutral surroundings. *Journal of Fluid Mechanics*, 93(02):241–250.

Desbarats, A. (1989). Support effects and the spatial averaging of transport properties. *Mathematical Geology*, 21(3):383–389.

Deutsch, C. (1989). Calculating effective absolute permeability in sandstone/shale sequences. *SPE Formation Evaluation*, 4(03):343–348.

Dietrich, C. R. and Newsam, G. N. (1993). A fast and exact method for multidimensional Gaussian stochastic simulations. *Water Resources Research*, 29(8):2861–2869.

Durlofsky, L. J. (1991). Numerical calculation of equivalent grid block permeability tensors for heterogeneous porous media. *Water Resources Research*, 27(5):699–708.

Durski, S. M., Glenn, S. M., and Haidvogel, D. B. (2004). Vertical mixing schemes in the coastal ocean: Comparison of the level 2.5 Mellor-Yamada scheme with an enhanced version of the K profile parameterization. *Journal of Geophysical Research: Oceans*, 109(C1).

Eames, I. and Bush, J. W. M. (1999). Longitudinal dispersion by bodies fixed in a potential flow. *Proceedings of the Royal Society of London. Series A: Mathematical, Physical and Engineering Sciences*, 455(1990):3665–3686.

Fiori, A., Janković, I., and Dagan, G. (2003). Flow and transport in highly heterogeneous formations: 2. Semianalytical results for isotropic media. *Water Resources Research*, 39(9).

Freedman, D. and Diaconis, P. (1981). On the histogram as a density estimator: L2 theory. *Probability Theory and Related Fields*, 57(4):453–476.

Garaud, P. and Brummell, N. (2015). 2D or not 2D: the effect of dimensionality on the dynamics of fingering convection at low Prandtl number. *The Astrophysical Journal*, 815(1):42.

Gelhar, L. W., Gutjahr, A. L., and Naff, R. L. (1979). Stochastic analysis of macrodispersion in a stratified aquifer. *Water Resources Research*, 15(6):1387–1397.

Gelhar, L. W., Welty, C., and Rehfeldt, K. R. (1992). A critical review of data on field-scale dispersion in aquifers. *Water Resources Research*, 28(7):1955–1974.

Ghesmat, K., Hassanzadeh, H., and Abedi, J. (2011). The effect of anisotropic dispersion on the convective mixing in long-term CO_2 storage in saline aquifers. *AIChE Journal*, 57(3):561–570.

Goggin, D. J., Chandler, M. A., Kocurek, G. T., and Lake, L. W. (1988). Patterns of permeability in eolian deposits: Page sandstone (Jurassic), northeastern Arizona. *SPE Formation Evaluation*, 3(02):297–306.

Greenkorn, R. A. and Kessler, D. P. (1969). Dispersion in heterogeneous nonuniform anisotropic porous media. *Industrial & Engineering Chemistry*, 61(9):14–32.

Hesse, M. A. and Woods, A. W. (2010). Buoyant dispersal of CO_2 during geological storage. *Geophysical Research Letters*, 37(1).

Hewitt, I. J. (2020). Subglacial plumes. *Annual Review of Fluid Mechanics*, 52:145–169.

Hidalgo, J. J. and Carrera, J. (2009). Effect of dispersion on the onset of convection during CO_2 sequestration. *Journal of Fluid Mechanics*, 640:441–452.

Janković, I., Fiori, A., and Dagan, G. (2003). Flow and transport in highly heterogeneous formations: 3. Numerical simulations and comparison with theoretical results. *Water Resources Research*, 39(9).

Janković, I., Fiori, A., and Dagan, G. (2006). Modeling flow and transport in highly heterogeneous three-dimensional aquifers: Ergodicity, Gaussianity, and anomalous behavior—1. conceptual issues and numerical simulations. *Water Resources Research*, 42(6).

Kampman, N., Bickle, M. J., Maskell, A., Chapman, H. J., Evans, J. P., Purser, G., Zhou, Z., Schaller, M. F., Gattacceca, J. C., Bertier, P., Chen, F., Turchyn, A. V., Assayag, N., Rochelle, C., Ballentine, C. J., and Busch, A. (2014). Drilling and sampling a natural CO_2 reservoir: Implications for fluid flow and CO_2-fluid–rock reactions during CO_2 migration through the overburden. *Chemical Geology*, 369:51–82.

Kantha, L. H. and Clayson, C. A. (1994). An improved mixed layer model for geophysical applications. *Journal of Geophysical Research: Oceans*, 99(C12):25235–25266.

Kantha, L. H. and Clayson, C. A. (2000). *Small scale processes in geophysical fluid flows*, volume 67. Elsevier.

Kara, A. B., Rochford, P. A., and Hurlburt, H. E. (2003). Mixed layer depth variability over the global ocean. *Journal of Geophysical Research: Oceans*, 108(C3).

Klise, K. A., Tidwell, V. C., and McKenna, S. A. (2008). Comparison of laboratory-scale solute transport visualization experiments with numerical simulation using cross-bedded sandstone. *Advances in Water Resources*, 31(12):1731–1741.

Koch, D. L. and Brady, J. F. (1988). Anomalous diffusion in heterogeneous porous media. *The Physics of fluids*, 31(5):965–973.

Kraus, E. B. and Turner, J. S. (1967). A one-dimensional model of the seasonal thermocline II. The general theory and its consequences. *Tellus*, 19(1):98–106.

Kuhlbrodt, T., Rahmstorf, S., Zickfeld, K., Vikebø, F. B., Sundby, S., Hofmann, M., Link, P. M., Bondeau, A., Cramer, W., and Jaeger, C. (2009). An integrated assessment of changes in the thermohaline circulation. *Climatic Change*, 96(4):489–537.

Large, W. G., McWilliams, J. C., and Doney, S. C. (1994). Oceanic vertical mixing: A review and a model with a nonlocal boundary layer parameterization. *Reviews of Geophysics*, 32(4):363–403.

Law, J. (1944). A statistical approach to the interstitial heterogeneity of sand reservoirs. *Transactions of the AIME*, 155(01):202–222.

Levenspiel, O. and Smith, W. K. (1957). Notes on the diffusion-type model for the longitudinal mixing of fluids in flow. *Chemical Engineering Science*, 6(4-5):227–235.

Li, Q. and Fox-Kemper, B. (2017). Assessing the effects of Langmuir turbulence on the entrainment buoyancy flux in the ocean surface boundary layer. *Journal of Physical Oceanography*, 47(12):2863–2886.

Matheron, G. and De Marsily, G. (1980). Is transport in porous media always diffusive? A counterexample. *Water Resources Research*, 16(5):901–917.

Mathieson, A., Midgely, J., Wright, I., Saoula, N., and Ringrose, P. (2011). In Salah CO_2 storage jip: CO_2 sequestration monitoring and verification technologies applied at Krechba, Algeria. *Energy Procedia*, 4:3596–3603.

McWilliams, J. C., Huckle, E., and Shchepetkin, A. F. (2009). Buoyancy effects in a stratified Ekman layer. *Journal of Physical Oceanography*, 39(10):2581–2599.

McWilliams, J. C. and Sullivan, P. P. (2000). Vertical mixing by Langmuir circulations. *Spill Science & Technology Bulletin*, 6(3–4):225–237.

Mellor, G. L. and Yamada, T. (1982). Development of a turbulence closure model for geophysical fluid problems. *Reviews of Geophysics*, 20(4):851–875.

Meyer, D. W., Jenny, P., and Tchelepi, H. A. (2010). A joint velocity-concentration PDF method for tracer flow in heterogeneous porous media. *Water Resources Research*, 46(12).

Middleton, J. H. (1975). The asymptotic behaviour of a starting plume. *Journal of Fluid Mechanics*, 72(04):753–771.

Moeng, C. H., McWilliams, J. C., Rotunno, R., Sullivan, P. P., and Weil, J. (2004). Investigating 2D modeling of atmospheric convection in the PBL. *Journal of the Atmospheric Sciences*, 61(8):889–903.

Morton, B. R., Taylor, G., and Turner, J. S. (1956). Turbulent gravitational convection from maintained and instantaneous sources. *Proceedings of the Royal Society of London. Series A. Mathematical and Physical Sciences*, 234(1196):1–23.

Niiler, P. P. and Kraus, E. B. (1977). One-dimensional models of the upper ocean. *Modelling and Prediction of the Upper Layers of the Ocean*, pages 143–172.

Nordahl, K. and Ringrose, P. S. (2008). Identifying the representative elementary volume for permeability in heterolithic deposits using numerical rock models. *Mathematical Geosciences*, 40(7):753–771.

Ohl, C. D., Tijink, A., and Prosperetti, A. (2003). The added mass of an expanding bubble. *Journal of Fluid Mechanics*, 482:271–290.

Pacanowski, R. C. and Philander, S. G. H. (1981). Parameterization of vertical mixing in numerical models of tropical oceans. *Journal of Physical Oceanography*, 11(11):1443–1451.

Paulson, C. A. and Simpson, J. J. (1977). Irradiance measurements in the upper ocean. *Journal of Physical Oceanography*, 7(6):952–956.

Pickup, G. E., Ringrose, P. S., Corbett, P. W. M., Jensen, J. L., and Sorbie, K. S. (1995). Geology, geometry and effective flow. *Petroleum Geoscience*, 1(1):37–42.

Price, J. F., Weller, R. A., and Pinkel, R. (1986). Diurnal cycling: Observations and models of the upper ocean response to diurnal heating, cooling, and wind mixing. *Journal of Geophysical Research: Oceans*, 91(C7):8411–8427.

Qiao, F., Yuan, Y., Yang, Y., Zheng, Q., Xia, C., and Ma, J. (2004). Wave-induced mixing in the upper ocean: Distribution and application to a global ocean circulation model. *Geophysical Research Letters*, 31(11).

Ramadhan, A., Wagner, G. L., Hill, C., Campin, J.-M., Churavy, V., Besard, T., Souza, A., Edelman, A., Marshall, J., and Ferrari, R. (2020). Oceananigans.jl: Fast and friendly geophysical fluid dynamics on GPUs. *Journal of Open Source Software*, 5(45):1965.

Reichl, B. G. and Hallberg, R. (2018). A simplified energetics based planetary boundary layer (ePBL) approach for ocean climate simulations. *Ocean Modelling*, 132:112–129.

Reichl, B. G. and Li, Q. (2019). A parameterization with a constrained potential energy conversion rate of vertical mixing due to Langmuir turbulence. *Journal of Physical Oceanography*, 49(11):2935–2959.

Riebesell, U., Schulz, K. G., Bellerby, R., Botros, M., Fritsche, P., Meyerhöfer, M., Neill, C., Nondal, G., Oschlies, A., Wohlers, J., and Zöllner, E. (2007). Enhanced biological carbon consumption in a high CO_2 ocean. *Nature*, 450(7169):545–548.

Rocco, S. and Woods, A. W. (2015). Dispersion in two-dimensional turbulent buoyant plumes. *Journal of Fluid Mechanics*, 774.

Romps, D. M. and Kuang, Z. (2011). A transilient matrix for moist convection. *Journal of the Atmospheric Sciences*, 68(9):2009–2025.

Saffman, P. G. (1959). A theory of dispersion in a porous medium. *Journal of Fluid Mechanics*, 6(3):321–349.

Scase, M. M., Aspden, A. J., and Caulfield, C. P. (2009). The effect of sudden source buoyancy flux increases on turbulent plumes. *Journal of Fluid Mechanics*, 635:137–169.

Scase, M. M., Caulfield, C. P., Dalziel, S. B., and Hunt, J. C. R. (2006). Time-dependent plumes and jets with decreasing source strengths. *Journal of Fluid Mechanics*, 563:443–461.

Schmalzl, J., Breuer, M., and Hansen, U. (2004). On the validity of two-dimensional numerical approaches to time-dependent thermal convection. *EPL (Europhysics Letters)*, 67(3):390.

Scorer, R. S. (1997). *Dynamics of meteorology and climate*. John Wiley & Sons.

Scott, D. W. (1979). On optimal and data-based histograms. *Biometrika*, 66(3):605–610.

Smyth, W. D., Skyllingstad, E. D., Crawford, G. B., and Wijesekera, H. (2002). Nonlocal fluxes and Stokes drift effects in the K-profile parameterization. *Ocean Dynamics*, 52(3):104–115.

Srzic, V., Cvetkovic, V., Andricevic, R., and Gotovac, H. (2013). Impact of aquifer heterogeneity structure and local-scale dispersion on solute concentration uncertainty. *Water Resources Research*, 49(6):3712–3728.

Stull, R. B. (1984). Transilient turbulence theory. part I: The concept of eddy-mixing across finite distances. *Journal of the Atmospheric Sciences*, 41(23):3351–3367.

Stull, R. B. (1993). Review of non-local mixing in turbulent atmospheres: Transilient turbulence theory. *Boundary-Layer Meteorology*, 62(1–4):21–96.

Stull, R. B. and Kraus, E. B. (1987). The transilient model of the upper ocean. *Journal of Geophysical Research: Oceans*, 92(C10):10745–10755.

Sturges, H. A. (1926). The choice of a class interval. *Journal of the American Statistical Association*, 21(153):65–66.

Suciu, N. (2014). Diffusion in random velocity fields with applications to contaminant transport in groundwater. *Advances in Water Resources*, 69:114–133.

Takahashi, T., Sutherland, S. C., Wanninkhof, R., Sweeney, C., Feely, R. A., Chipman, D. W., Hales, B., Friederich, G., Chavez, F., Sabine, C., et al. (2009). Climatological mean and decadal change in surface ocean pCO_2, and net sea–air CO_2 flux over the global oceans. *Deep Sea Research Part II: Topical Studies in Oceanography*, 56(8–10):554–577.

Tan, Z., Kaul, C. M., Pressel, K. G., Cohen, Y., Schneider, T., and Teixeira, J. (2018). An extended eddy-diffusivity mass-flux scheme for unified representation of subgrid-scale turbulence and convection. *Journal of Advances in Modeling Earth Systems*, 10(3):770–800.

Taylor, J. R. and Ferrari, R. (2010). Buoyancy and wind-driven convection at mixed layer density fronts. *Journal of Physical Oceanography*, 40(6):1222–1242.

Tidwell, V. C. and Wilson, J. L. (2000). Heterogeneity, permeability patterns, and permeability upscaling: Physical characterization of a block of Massillon sandstone exhibiting nested scales of heterogeneity. Technical report, Sandia National Labs., Albuquerque, NM (US).

Tompson, A. F. B. and Gelhar, L. W. (1990). Numerical simulation of solute transport in three-dimensional, randomly heterogeneous porous media. *Water Resources Research*, 26(10).

Turner, J. S. (1957). Buoyant vortex rings. *Proceedings of the Royal Society of London. Series A. Mathematical and Physical Sciences*, 239(1216):61–75.

Turner, J. S. (1962). The 'starting plume' in neutral surroundings. *Journal of Fluid Mechanics*, 13(03):356–368.

Vallis, G. K. (2019). *Essentials of Atmospheric and Oceanic Dynamics*. Cambridge University Press.

Van Roekel, L., Adcroft, A. J., Danabasoglu, G., Griffies, S. M., Kauffman, B., Large, W., Levy, M., Reichl, B. G., Ringler, T., and Schmidt, M. (2018). The KPP boundary layer scheme for the ocean: Revisiting its formulation and benchmarking one-dimensional simulations relative to LES. *Journal of Advances in Modeling Earth Systems*, 10(11):2647–2685.

Woods, A. W. (2010). Turbulent plumes in nature. *Annual Review of Fluid Mechanics*, 42:391–412.

Woods, A. W. (2015). *Flow in porous rocks*. Cambridge University Press.

Zavala-Sanchez, V., Dentz, M., and Sanchez-Vila, X. (2009). Characterization of mixing and spreading in a bounded stratified medium. *Advances in Water Resources*, 32(5):635–648.

Appendix A

Numerical simulations of flows through porous rocks

We model flow through a domain spanning $(0, D)$ in the x direction and $(0, H)$ in the z direction with $D \gg H$, which is driven by a pressure gradient in the x direction.

The flow field, $\mathbf{u} = (u, w)$, is given by the continuity equation and Darcy's law for an isotropic medium. This gives an equation for the pressure field, $p(x, z)$.

$$\nabla \cdot \mathbf{u} = 0, \qquad \mathbf{u} \equiv \begin{pmatrix} u \\ w \end{pmatrix} = -\frac{1}{\mu} \begin{pmatrix} k_{xx} & k_{xz} \\ k_{zx} & k_{zz} \end{pmatrix} \begin{pmatrix} \partial p/\partial x \\ \partial p/\partial z \end{pmatrix}, \tag{A.1}$$

where μ is the dynamic viscosity of the fluid, and the matrix on the right hand side is the local permeability tensor, $\underline{\underline{k}}(x, z)$. The permeability tensor is symmetric ($k_{xz} = k_{zx}$) and positive definite ($k_{xx}k_{zz} \geq k_{xz}^2,\ k_{xx} > 0,\ k_{zz} > 0$). We impose pressure boundary conditions,

$$p = 1 \quad \text{at} \quad x = 0, \qquad p = 0 \quad \text{at} \quad x = D, \tag{A.2}$$

while the no-flux condition through the top and bottom boundaries may be expressed in terms of $\mathbf{n}$, the normal to the top ($z = H$) and bottom ($z = 0$) boundaries,

$$\mathbf{u} \cdot \mathbf{n} = 0 \implies w = 0 \implies p_z = 0 \quad \text{at} \quad z = 0, H. \tag{A.3}$$

To solve for pressure, we require that the permeability field, $\underline{\underline{k}}(x, z)$, is continuous and differentiable (cf. equation (A.1)). Table A.1 summarises the functions used to generate the permeability field in each set of simulations. Equation (A.1) is solved using a pseudo-spectral code in Dedalus (Burns et al., 2019). We use Fourier modes in the x direction and Chebyshev modes in the z direction. We use an artificial time-marching scheme to converge to a fixed point for the pressure. For time-stepping, we use a one-stage first-order Runge-Kutta method with a uniform time-step. We run with a resolution of (N_x, N_z) spectral modes to resolve the permeability field and ensure stability of the time-stepping method (see table A.1). Using the computed pressure field, we estimate the flow field using Darcy's equation (A.1). To estimate the travel times along individual streamlines over a region of length L, we integrate along each streamline at height z as

$$t_s = \int_0^L \frac{\mathrm{d}x}{u_s(x, z)}, \quad U = \frac{L}{t_s}, \tag{A.4}$$

where u_s is the horizontal speed along streamline s and U is the mean flow speed along individual streamlines which varies with the vertical location, z, of the streamline in the channel. Across all simulations, we keep the channel width constant ($H = 1$).

Furthermore, to illustrate the evolution of tracer concentration in the domain, a pulse of inert tracer is injected instantaneously with the flow at $t = 0$. The concentration of this tracer, $c(x, z, t)$, follows the conservation equation,

$$c_t + \mathbf{u} \cdot \nabla c = \kappa \nabla^2 c, \tag{A.5}$$

where κ the coefficient of molecular diffusion. The value of κ in our numerical simulations is chosen to be 10^{-4}. We choose a small enough value of κ so that the time scale for transverse pore-scale diffusion is negligible compared to the time scales of shear due to the presence of heterogeneity. For the parameter values in our calculations, this is consistent with the requirement that $\kappa \ll \mathcal{O}(1 - 10)$. We solve equation (A.5) using a third-order four-stage Runge-Kutta method with a uniform time-step.

Table A.1 For each figure/chapter, the table summarises the functions used to describe the permeability field, the channel dimensions, (D, H), the spectral resolution used to solve for the pressure field, (N_x, N_z), and the parameters that are kept constant in each set of simulations. In all sets of simulations, we check for convergence by varying numerical resolution.

	Permeability field	(D, H)	(N_x, N_z)	Constant
Figure 2.1	Fast Fourier transform method proposed by Dietrich and Newsam (1993)	(544,1)	(32768,544)	Correlation scales, $l_x = 1,\ l_z = 0.4$
Chapter 2	$\frac{k(x,z)}{k_1} = \left(\frac{k_2}{k_1}\right)^{\beta_r(x,z)}$ $\beta_r(x,z) = \exp\left(-\left(\frac{(x-x_c)^2}{(l/2)^2}\right)^{\gamma} - \left(\frac{(z-z_c)^2}{(h/2)^2}\right)^{\gamma}\right)$	(40,1)	(16384,4096)	$k_1 = 1,\ \gamma = 20,$ $x_c = 20$
Chapter 3	$\frac{k(x,z)}{k_1} = \left(\frac{k_2}{k_1}\right)^{\beta_e(x,z)}$ $\beta_e(x,z) = \exp\left(-\left(\frac{(x-x_c)^2}{(l/2)^2} + \frac{(z-z_c)^2}{(h/2)^2}\right)^{\gamma}\right)$	(20,1)	(8192,4096)	$k_1 = 1,\ \gamma = 20,$ $x_c = 10,\ l = 1$
Chapter 4	$\beta_c(x,z) = \exp\left(-\left(\frac{(x-D/2)-(z-z_c)\cot\theta_e}{(d/2)}\right)^{\gamma}\right)$ $K_{1,2}(x,z) = k_0 + (k_{1,2} - k_0)\beta_c(x,z)$ $\underline{\underline{k}}(x,z) = \begin{pmatrix} K_1\cos^2\theta_i + K_2\sin^2\theta_i & (K_1 - K_2)\cos\theta_i\sin\theta_i \\ (K_1 - K_2)\cos\theta_i\sin\theta_i & K_2\cos^2\theta_i + K_1\sin^2\theta_i \end{pmatrix}$	(20,1)	(2048,512)	$k_0 = 1,\ \gamma = 20,$ $x_c = 5,\ z_c = 0.5,$ $d = 10$

In chapters 2 and 3, the permeability field is isotropic so that $k_{xx} = k_{zz} \equiv k(x,z)$ and $k_{xz} = k_{zx} = 0$, so we solve $\nabla \cdot (k \nabla p) = 0$ (cf. equation (A.1)). The heterogeneous permeability field described in figure 2.1 is generated using a fast Fourier transform method proposed by Dietrich and Newsam (1993).

In the simulations described in chapter 2, we define the permeability using a rectangular Gaussian function, $\beta_r(x,z)$,

$$\frac{k(x,z)}{k_1} = \left(\frac{k_2}{k_1}\right)^{\beta_r(x,z)}, \quad \beta_r(x,z) = \exp\left(-\left(\frac{(x-x_c)^2}{(l/2)^2}\right)^{\gamma} - \left(\frac{(z-z_c)^2}{(h/2)^2}\right)^{\gamma}\right), \tag{A.6}$$

where we choose a value of γ to ensure that the permeability varies smoothly from k_2 to k_1 over a distance $\ll l, h$.

In the simulations described in chapter 3, we define the permeability using an elliptic Gaussian function, $\beta_e(x,z)$,

$$\frac{k(x,z)}{k_1} = \left(\frac{k_2}{k_1}\right)^{\beta_e(x,z)}, \quad \beta_e(x,z) = \exp\left(-\left(\frac{(x-x_c)^2}{(l/2)^2} + \frac{(z-z_c)^2}{(h/2)^2}\right)^{\gamma}\right), \tag{A.7}$$

where the region containing the lens is

$$\frac{(x-x_c)^2}{(l/2)^2} + \frac{(z-z_c)^2}{(h/2)^2} \leq 1. \tag{A.8}$$

Again we choose a value of γ to ensure that the permeability at an angle ϕ about the centre of the ellipse varies smoothly from k_2 to k_1 over a distance $\mathcal{O}\left(\frac{\sqrt{l^2\cos^2\phi + h^2\sin^2\phi}}{\gamma}\right) \ll l, h$.

In chapter 4, the anisotropic permeability transitions smoothly from $K_1 = k_0$ and $K_2 = k_0$ to $K_1 = k_1$ and $K_2 = k_2$, where the depositional layers within the cross-bedded layer are inclined at an angle θ_i to the lateral boundaries, and the interface between the two regions is titled at an angle θ_e to the lateral boundaries. In such a configuration, we define the permeability using a function $\beta_c(x,z)$,

$$\beta_c(x,z) = \exp\left(-\left(\frac{(x-D/2) - (z-z_c)\cot\theta_e}{(d/2)}\right)^{\gamma}\right), \tag{A.9}$$

so that

$$K_1(x,z) = k_0 + (k_1 - k_0)\beta_c(x,z), \tag{A.10a}$$
$$K_2(x,z) = k_0 + (k_2 - k_0)\beta_c(x,z). \tag{A.10b}$$

Again, we choose a value of γ to ensure that the permeability varies smoothly over a distance $\ll d, H$. The components of the permeability tensor in terms of K_1 and K_2 are (Bear, 1971)

$$\left.\begin{aligned} k_{xx} &= K_1 \cos^2\theta_i + K_2 \sin^2\theta_i, \\ k_{xz} &= (K_1 - K_2)\cos\theta_i \sin\theta_i, \\ k_{zz} &= K_2 \cos^2\theta_i + K_1 \sin^2\theta_i. \end{aligned}\right\} \tag{A.11}$$

Table A.1 summarises the permeability functions, the domain length, the numerical resolution, and the parameters kept constant in each set of simulations described in this thesis. In all sets of simulations, we check for convergence by varying numerical resolution; we find that doubling the numerical resolution changes the mean flow speed, U (equation (A.4)), by less than 0.05%.

Appendix B

Derivation of the eddy diffusivity kernel

Let ϕ' be the Green's function for the integro-differential operator on the left hand side of equation (5.15), so that

$$\left(\frac{\partial}{\partial t} + \mathbf{u}.\nabla - \nabla^2\right)\phi'(\mathbf{x}, t|\mathbf{x}', t') - \frac{\partial}{\partial z}\overline{w'\phi'} = \delta(\mathbf{x} - \mathbf{x}')\delta(t - t'). \tag{B.1}$$

Multiplying equation (B.1) by $-w'(\mathbf{x}', t')\partial\overline{c}(z', t')/\partial z'$ and integrating with respect to $\mathbf{x}'$ and t' shows by comparison with equation (5.15) that

$$c'(\mathbf{x}, t) = -\int \mathrm{d}\mathbf{x}'\ \mathrm{d}t'\ \phi'(\mathbf{x}, t|\mathbf{x}', t')w'(\mathbf{x}', t')\frac{\partial\overline{c}(z', t')}{\partial z'}. \tag{B.2}$$

Multiplying equation (B.2) by w' and taking a horizontal average gives the flux, $\overline{w'c'}$, which is a function of z and t,

$$\overline{w'c'} = -\int \mathrm{d}z'\ \mathrm{d}t'\left[\int \mathrm{d}x'\ \overline{w'(\mathbf{x}, t)\phi'(\mathbf{x}, t|\mathbf{x}', t')w'(\mathbf{x}', t')}\right]\frac{\partial\overline{c}(z', t')}{\partial z'}. \tag{B.3}$$

The term in square brackets is a kernel, $\tilde{\mathcal{K}}(z, t|z', t')$, for the temporally evolving, horizontally averaged flux. Since $f(z)$ does not depend on time and the flow is

in a statistically steady state, $\partial\overline{c}/\partial t$ is negligible. Therefore, the temporally and horizontally averaged flux becomes

$$\langle w'c' \rangle = -\int \mathrm{d}z' \left[\int \mathrm{d}x' \, \mathrm{d}t' \, \langle w'(\mathbf{x},t)\phi'(\mathbf{x},t|\mathbf{x}',t')w'(\mathbf{x},t)\rangle \right] \frac{\partial \langle c \rangle (z')}{\partial z'}, \tag{B.4}$$

with $\langle * \rangle = \lim_{\tau\to\infty} \tau^{-1} \int_0^\tau * \, \mathrm{d}t$. The kernel, $\mathcal{K}(z|z')$, which maps the gradients to the fluxes is the term in the square brackets in equation (B.4).

$$\langle w'c' \rangle = -\int \mathcal{K}(z|z') \frac{\partial \langle c \rangle (z')}{\partial z'} \, \mathrm{d}z' \tag{B.5}$$

Ensemble (rather than spatial-temporal) averaging would lead to the same form after invoking stationarity and horizontal homogeneity, appropriate to our periodic domain.